UNIVERSITÀ POLITECNICA DELLE MARCHE

FACOLTÀ DI INGEGNERIA

Corso di Laurea Magistrale in Ingegneria Meccanica

Misure di scambio termico in un impianto di turbina ad alta pressione

Heat transfer measurements in a high-pressure turbine rig

Relatore: Chiar.mo
Nicola PAONE

Correlatore: Chiar.mo
Paolo CASTELLINI

Tesi di Laurea di:
Giorgia CRISPIANI

Correlatore:
Sergio LAVAGNOLI

A.A 2020-2021

Mi prometto del passato,

di far tesoro del vissuto.

Mi prometto della strada,

dei principi tramandatimi,

del tempo per imparare.

Mi prometto di essere,

di esistere,

di farlo con educazione.

Mi prometto della scelta,

degli esempi concreti,

di essere selettiva,

di sapere per me.

Ringraziamenti

Prima di procedere con la trattazione, vorrei dedicare qualche riga a tutti coloro che, con dedizione e pazienza hanno contribuito alla realizzazione di questo elaborato.

Ringrazio il Prof. Paone Nicola e il Prof. Castellini Paolo per avermi incoraggiata ad intraprendere il tirocinio al Von Karman Institute, esperienza da cui prende vita questa tesi.

Ringrazio il Prof. Sergio Lavagnoli per avermi dato l'opportunità di far parte di un progetto così ambizioso.

Un ringraziamento particolare va al mio advisor Bogdan Cernat per avermi trasmesso le conoscenze necessarie alla stesura di questa tesi, ma soprattutto per avermi seguita pazientemente, motivata e supportata in ogni istante.

Un ringraziamento doveroso va ai miei due compagni di viaggio, Giacomo e Filippo, per la condivisione quotidiana di stress e risate. Senza di voi quest'esperienza non avrebbe avuto lo stesso sapore.

Non posso non menzionare le mie amiche di sempre, che anche in questo percorso mi hanno confermato come la condivisione delle nostre vite è e sarà sempre vitale.

Dedico infine questo traguardo alla mia famiglia; per gli insegnamenti, la pazienza, la forza, la costanza, la presenza. A voi devo tutto.

Abstract

The main objectives concerning the design of turbomachines deal with an overall improvement in efficiency and the continuous search for larger performance development. Thus, a substantial effort has been made to understand the aerothermal loss mechanisms and their origins in the highly unsteady environment of turbomachines. The experimental investigation on the performance of modern gas turbines is of fundamental importance for the quantification of the efficiency and the life span of the components. Significant research efforts are presently devoted to the understanding of the unsteady flow structures generated in the high-pressure turbine (HPT) stage in order to quantify their contribution among the efficiency loss sources and to design innovative solutions for their containment.

In the frame of a large project investigating the aerodynamics and heat transfer of high-pressure turbines, this work is an experimental investigation of the steady and unsteady heat transfer on the stator blade of a transonic turbine stage. The main goals of the project will be to setup, acquire and process measurements of heat transfer carried out by means of double-layered thin film gauges that guarantee a better signal to noise ratio and a better resolution of the unsteady phenomena with respect to the single layer one. These transducers are suitable for the detection of the unsteady component since they have a bandwidth high enough to detect what expected.

The measurements were performed in the compression tube turbine test rig CT3 at the Von Karman Institute around the stator blade at 50% and 90% span covering 26 locations for each section.

Abstract

Questa tesi presenta uno studio sul trasferimento di calore sullo statore di una turbina ad alta pressione che ha avuto luogo attraverso test eseguiti in un impianto del von Karman Institute, in condizioni rappresentative dei motori aeronautici. Nella prima parte del report viene fornita la descrizione della struttura della facility e dei sensori utilizzati nella campagna test. Le misurazioni eseguite attraverso film sottili ad alta risposta dinamica, hanno fornito il flusso di calore risolto e mediato nel tempo. Le termocoppie sono state invece impiegate per l'analisi delle condizioni di flusso in ingresso e in uscita dallo stadio di turbina. A questa parte segue la sezione dedicata alla descrizione dei processi di calibrazione che hanno permesso di ottenere le relazioni che legano il segnale acquisito alla temperatura. L'analisi prevede che la calibrazione debba essere eseguita in un bagno d'olio per ottenere un risultato migliore del 25%. La calibrazione interna del digitalizzatore porta ad un'incertezza di ±0,2°C rispetto ai ±0.15°C ottenuti con la calibrazione a bagno d'olio. Successivamente, è stata effettuata l'analisi del trasferimento di calore stazionario e instabile. Il nuovo metodo di calcolo sviluppato da Oldfield ha permesso di ottenere il flusso di calore partendo dall'andamento della tensione. L'andamento del coefficiente di scambio termico ottenuto dalla precedente analisi a midspan, in linea con i risultati attesi, ha mostrato un aumento non solo nel LE ma anche nella parte posteriore del lato di aspirazione (88% dell'ascissa curvilinea) dovuto all'effetto destabilizzante del rotore e alla riduzione dell'accelerazione del flusso che ha determinato il passaggio da laminare a turbolento con aumento del trasferimento di calore. È stata valutata la ripetibilità da test a test. La distribuzione della pressione delle pale dello statore è stata calcolata e confrontata con i risultati CFD mostrando un buon accordo. Lo studio delle condizioni aerodinamiche ha permesso di interpretare l'andamento del coefficiente di scambio termico verificandone l'influenza su quest'ultimo. Le misure effettuate al 90% della campata hanno invece mostrato un picco molto più avanzato verso il LE (35% dell'ascissa curvilinea) probabilmente per effetto dei flussi secondari in prossimità dell'involucro che hanno indotto una transizione prematura. La distribuzione del numero di Nusselt, in funzione del numero Re e della turbolenza, trovando una buona corrispondenza con le correlazioni di Lowery e Vachon utilizzate per prevedere il numero di Nusselt sul punto di stagnazione.

L'analisi instabile è stata effettuata utilizzando la funzione pWelch su Matlab evidenziando l'influenza del rotore soprattutto nella parte posteriore del lato aspirazione dove il contenuto in frequenza è maggiore e sono chiaramente distinguibili la frequenza di passaggio della pala (4,7 kHz) e le armoniche associate, anche prima dell'inizio della prova. In accordo con l'analisi instabile, l'andamento del RMS ha, inoltre, mostrato fluttuazioni più pronunciate nella parte posteriore del lato di aspirazione. L'analisi del periodo antecedente l'inizio della prova ha permesso di individuare picchi di frequenza spuri non riconducibili ad un comportamento reale e fisico del fluido, confermando inoltre che le discrepanze da prova a prova nell'andamento RMS erano dovute alla presenza di rumore. La transizione da laminare a turbolenta è stata analizzata attraverso l'intermittency factor e lo skewness. Poiché il lato aspirazione è responsabile di gran parte delle perdite complessive, nelle future indagini e campagne sperimentali dovrebbe essere utilizzato un numero maggiore di sensori per essere maggiormente indagati al fine di poter conoscere opportunamente l'andamento dell'intermittency factor e dello skewness che nella presente valutazione, per la mancanza di sufficienti punti di misurazione nell'area della discussione, non ha fornito risultati coerenti con le aspettative.

Contents

Abstract IV

List of Figures X

List of Tables XV

List of Symbols XVII

Introduction 1

1.1 Turbomachinery overview 1

1.2 Modern aero-engine research and HPT stage flow field 3

1.3 Aims of the project and thesis outline 6

Experimental Methods 7

2.1 Rotating Turbine Test Rig CT-3 7

2.2 Experimental setup 11

2.3 Theoretical background 15

2.3.1 Thermocouples 15

2.3.2 Data processing methodologies for thin film measurements 15

2.3.2.1 Numerical method 18

2.3.2.2 Filter method 24

Static calibration 27

3.1 Thermocouples static calibration 27

3.1.1 Uncertainty analysis thermocouples calibration 35

3.2 Thin film casing insert calibration 38

3.2.1 Annealing 38

3.2.2 Resistance - temperature calibration 47

3.2.3 Uncertainty analysis thin films calibration 54

3.3 Thin film instrumented vane calibration 55
Experimental campaign 56
4.1 Instrumented stator vanes 56
4.1.1 Heat transfer data conditioning 57
4.1.2 Heat transfer data processing 59
4.1.3 Steady data processing 62
4.1.4 Unsteady data processing 79
4.1.4.1 Intermittency factor 88
4.1.4.2 Skewness 92
Conclusions 94
Bibliography 97
Appendix A 101
Appendix B 105
Appendix C 110
Appendix D 113

List of Figures

Figure 1.1: Components and main flows of the turbofan engine 2
Figure 1.2: Gas turbine thermodynamic cycle..... 3
Figure 1.3: Pressure and Temperature evolution of a Rolls-Royce Trent 800 4
Figure 1.4: Secondary flows representation 5
Figure 2.5: Turbine rig and test section..... 7
Figure 2.6: Evolution of the main turbine parameters during the test. 9
Figure 2.7: HPT stage meridional view and rainbow rotor setup..... 10
Figure 2.8: Plane 01-03 aerothermal probes: reference probe (a), total temperature rake (b) 11
Figure 2.9: Radial profiles of total temperature measured at the stage inlet (Plane 01) 12
Figure 2.10: Meridional view turbine stage..... 12
Figure 2.11: Meridional view of CT-3 facility 13
Figure 2.12: Heat transfer casing insert..... 13
Figure 2.13: High speed turbine test rig (CT3): meridional view 14
Figure 2.14: Instrumented stator vane 14
Figure 2.15: Comparison of sensor's structures 18
Figure 2.16: Two-layer heat transfer gauge..... 18
Figure 2.17: Scheme of 1D semi-infinite approach..... 19
Figure 2.18: Example of data interpolation and linear regression..... 23
Figure 2.19: Impulse response function and heat flux derived from Tw signal..... 26
Figure 3.20: Set up for the calibration procedure: 1=test chamber, 2=thermocouples, 3=digitizer, 4=acquisition system..... 27
Figure 3.21: Thermocouples and test chamber temperature trend between 40°C and 45°C 28
Figure 3.22: Calibration law average value..... 29
Figure 3.23: Comparison between digitizer's internal calibration and reference one..... 30
Figure 3.24: Temperature variation in the two lying planes of the thermocouples..... 31
Figure 3.25: Comparison between calibration law performed with the casing (continuous line) and the one without the casing (dashed line) 32

Figure 3.26: Comparison between standard deviation trend related to the calibration performed with the casing (continuous line) and the setting without the casing (dashed line) 32
Figure 3.27: Set up for the calibration procedure: 1=Isotech bath, 2=thermocouples, 3=digitizer, 4=reference probe (PT100), 5=acquisition system 33
Figure 3.28: Calibration law 34
Figure 3.29: Setup for the annealing procedure 38
Figure 3.30: Drawing of thin film circuit 39
Figure 3.31: Temperature trend over time relative to the thin films taken as reference 39
Figure 3.32: Resistance trend over time relative to the thin films taken as reference 39
Figure 3.33: Resistance comparison before and after the annealing procedure 40
Figure 3.34: Comparison before and after the first annealing in terms of temperature 40
Figure 3.35: Setup scheme for the annealing procedure with thin films switched on 41
Figure 3.36: Simplified schematic of the electronics of the thin film conditioning unit 42
Figure 3.37: Picture of control unit's front and real panels 42
Figure 3.38: Temperature trend over time relative to the thin films taken as reference 43
Figure 3.39: Voltage trend over time relative to the thin film taken as reference 43
Figure 3.40: Voltage stability analysis over time 44
Figure 3.41: Resistance Comparison before and after the last annealing procedure 45
Figure 3.42: Comparison before and after the last annealing in terms of temperature 45
Figure3.43: Thin film insert positioning inside the test chamber. 47
Figure 3.44: Setup for test chamber calibration 48
Figure 3.45: Calibration law 49
Figure 3.46: Residual plot for reference thin film 49
Figure 3.47: Calibration law 50
Figure 3.48: Comparison linear regression coefficients 51
Figure 3.49: Comparison linear regression coefficients of the second calibration 52
Figure 3.50: Comparison resistance before and after calibration process 53
Figure 3.51: Calibration setup 55
Figure 4.52: Qualitative trend of the temperature amplitude decreasing with heat flux frequency. 57
Figure 4.53: Shaped gain 58
Figure 4.54: High- and low-frequency data conditioning and acquisition 59

Figure 4.55: maximum h variation 60
Figure 4.56: Voltage to temperature signal processing steps 61
Figure 4.57: Processing steps 62
Figure 4.58: Raw voltage trend over pressure side and suction side 63
Figure 4.59: Gas temperature trend plane 01 for tests at 50% and 90% of the vane span .. 64
Figure 4.60: Typical wall temperature and gas temperature evolution 65
Figure 4.61: Test to test wall temperature drift with respect to the gas temperature 65
Figure 4.62: Heat transfer window to window variability respectively at 50% and 90% of the vane span 67
Figure 4.63: Heat transfer test to test repeatability respectively at 50% and 90% of the vane span 68
Figure 4.64: HTC trend and aerodynamic conditions comparison 50% and 90% of the vane span 69
Figure 4.65: Comparison h trend at 50% and 90% of the vane span 71
Figure 4.66: Time-average Nusselt number distribution: test to test repeatability at midspan and at 90%; b) comparison between the two investigated heights 73
Figure 4.67: Nusselt number distribution around the cylinder 75
Figure 4.68: Nu number at the stagnation point as a function of Reynolds and the turbulence intensity 76
Figure 4.69: Mach distribution around the instrumented vane 78
Figure 4.70: Comparison FFT and Welch's method 80
Figure 4.71: PSD sensor 6 on pressure side 81
Figure 4.72: PSD sensor 25 on suction side 81
Figure 4.73: Comparison PSD sensor 25 at 50 and 90% of the vane span 82
Figure 4.74: Power spectral density before the start of tests for sensor 6 (PS) and 26 (SS) 82
Figure 4.75: PSD for all the sensors at midspan 83
Figure 4.76: PSD for all the sensors at 90% of the vane span 84
Figure 4.77: Root-mean-square's h over testing time at midspan 85
Figure 4.78: Root-mean-square's h over 50 ms at midspan 85
Figure 4.79: Comparison h trend over pre-rising period for sensors 2 and 9 86
Figure 4.80: Root-mean-square trend at 90% of the vane span 87
Figure 4.81: Root-mean-square comparison between the sensors at 50% and those at 90% of the vane span 87

Figure 4.82: PSDI method 88
Figure 4.83: Power spectral density on suction side at midspan 89
Figure 4.84: Intermittency factor through Power Spectral Density Integral at midspan 90
Figure 4.85: Power spectral density on suction side at 90% of the vane span 90
Figure 4.86: Intermittency factor through Power Spectral Density Integral at 90% of the vane span 91
Figure 4.87: Theoretical skew distribution 92
Figure 4.88: Skew trend over suction side at midspan 93
Figure 4.89: Skew trend over suction side at 90% of the vane span 93
Figure A1: Comparison in terms of temperature of the two calibrations, the reference one and the digitizer one 102
Figure B1: Geometry of the tested profile and thin film location at midspan (on the left) and at 90% of the vane span (on the right) 105
Figure B2: Stator blade thin film: 50% and 90% 106
Figure B3: thin film positions along the chord and along the curvilinear abscissa: 50% and 90% 107
Figure D1: Power spectral density 113

List of Tables

Table 2.1: Experimental test conditions 10
Table 3.2: Linear regression coefficients, slope, intercept and R2..... 29
Table 3.3: Comparison linear regression coefficients between the ref and the digitizer calibration 30
Table 3.4: Comparison between linear regression coefficients applying the spatial calibration or not..... 31
Table 3.5: Comparison between calibration coefficients performed with the casing (continuous line) and the one without the casing (dashed line) 32
Table 3.6: Average calibration coefficients for oil bath calibration..... 34
Table: 3.7: Summary scheme of the terms considered in the uncertainty budget..... 37
Table 3.8: Heat Transfer Control Board Settings..... 42
Table: 3.9: summary table of the changes in resistance and temperature undergone by the sensors following the annealing procedure 46
Table 3.10: Linear regression coefficients 49
Table 3.11: Average variation calibration parameters. 50
Table 3.12: Average variation calibration parameters. 52
Table 3.13: Check possible drift in thin films resistances after each calibration. 53
Table 3.14: Summary scheme of the terms taken into account in the uncertainty analysis. 54
Table A1: Thermocouples' calibration set-up and coefficients..... 102
Table A2: Calibration coefficients thin film casing insert 103
Table A3: Calibration coefficients thin film on instrumented vane 104
Table B3: Summary of the test conditions at 50% and 90% of the vane span..... 109
Table C1: thin-film setup and connections at 50% and 90% of the vane's span 112

List of Symbols

Acronyms

1D one-dimensional

BPF Blade Passing Frequency

DAS Data Acquisition System

DFT Discrete Fourier Transform

IRM Impulse Response Method

PDS Power Spectral Density

RMS root mean square

RPF Rotor Passing Frequency

RSS Root Sum Square

VKI von Karman Institute for Fluid Dynamics

PS Pressure Side

SS Suction Side

LE Leading Edge

TE Trailing Edge

CT-3 Compression tube

Roman symbols

D diameter [mm]

C vane chord [m]

f frequency [Hz]

fs sampling frequency [Hz]

h heat transfer coefficient [W/(m^{2}K)]

I current intensity [A]

k thermal conductivity [W/ (m K)]

L thin film length [mm]

M Mach number -

Nu Nusselt number –

p Laplace variable -

P power [W]

$\dot{q}$ heat flux [W/m^2]

R resistance Ω

Re Reynolds number -

R $_c$ radius of curvature m

s curvilinear abscissa [m]

t time [s]

T temperature [K]

Tu turbulence intensity [%]

T_0 total gas temperature [K]

Tr recovery temperature [K]

V voltage [V]

Greek symbols

α thermal diffusivity [m^2/s]

ρ density [kg/m^3]

μ dynamic viscosity [$W/(m^2K^4)$]

σ standard deviation

Subscript

0 total conditions

01 inlet of the stator

02 outlet of the stator, inlet of the rotor

03 outlet of the rotor

gas value in the flow

wall value at the surface

Chapter 1

Introduction

1.1 Turbomachinery overview

Turbomachinery, in mechanical engineering, describes machines that transfer energy between a rotor and a fluid, including both turbines and compressors. While a turbine transfers energy from a fluid to a rotor, a compressor transfers energy from a rotor to a fluid. The operating principle of turbomachinery is, hence, based on the transfer of energy between the rotating elements and the continuous flow that passes through it. This energy exchange is due to changes in momentum and is converted into shaft power and/or thrust.

Axial flow turbomachinery whose purpose is to generate thrust are widely used in aircraft engine applications. Their operating principle provides for the entry of air at ambient pressure into a dynamic inlet and then compressed by a certain number of axial stages in order to reach a pressure value that allows combustion in the next chamber. The exhaust gases are then expanded by the axial stages of the turbine and then further accelerated in a nozzle to generate thrust. In ideal conditions the thrust is given by the following relation:

$$T = \dot{m}(V_j - U)$$

where $\dot{m}$ is the mass flow that enters in the engine from the inlet, Vj is the exhaust gases speed and U is the speed of the air coming from the dynamic inlet. In order to have a high thrust, the mass flow should be the highest possible (together with V_j) and this is possible by using axial flow machines instead of radial flow machines. Modern aeroengines, such as the turbofan engines capable of delivering high thrust without the high fuel consumption as compared to a turbojet engine, have evolved from their introduction in the 1950s to their current role as the primary power source for today's commercial aviation fleet.

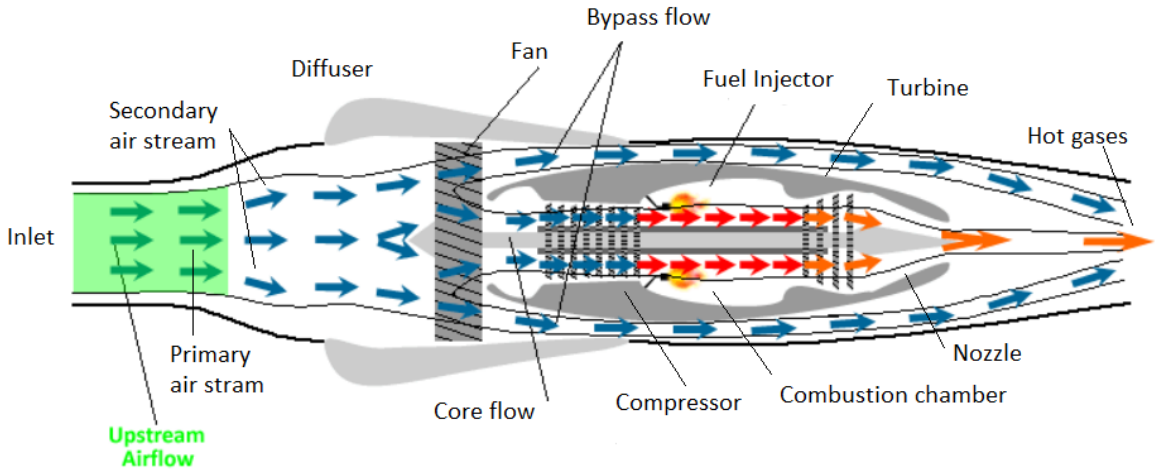

Figure 1.1: Components and main flows of the turbofan engine

A typical modern turbofan, shown in schematic cross-section in Fig. 1.1, produces thrust by ingesting ambient air, compressing the air, undergoing combustion, and expanding the hot gas through thrust-producing exhaust nozzles.

In detail, air at atmospheric conditions is first ingested by the fan located in the front part of the machine. The mass flow coming from the inlet, after the fan compression is divided in two ways: one part going to a bypass duct, giving the necessary thrust, the other going to the core engine (where the compressor, burner and turbine are located). The primary air stream is driven in the compressor where, as shown in the diagrams in Figure 1.2, in the ideal case, the compression produces an isentropic increase of pressure and temperature (phase 1-2). This transformation is not isentropic in the real case mainly because of the continuous losses.

The compressed air is then injected in the combustion chamber where fuel is also injected, thus generating combustion which leads to an increase of entropy and temperature (up to 1200 K) at constant pressure (phase 2-3). The hot gas is then released into the turbine stages, which have the task of extracting energy needed to drive the fan, the compressor stages and the auxiliary systems. The turbine causes an isentropic decrease in pressure (in the real case the behaviour of friction losses is beneficial, thus improving the expansion), as can be seen in phase 3-4. In aero-engine applications, the turbine's exhaust gases are furtherly expanded in a nozzle (with the interposition of an afterburner in supersonic aircraft) in order to gain the thrust coming from their kinetic energy.

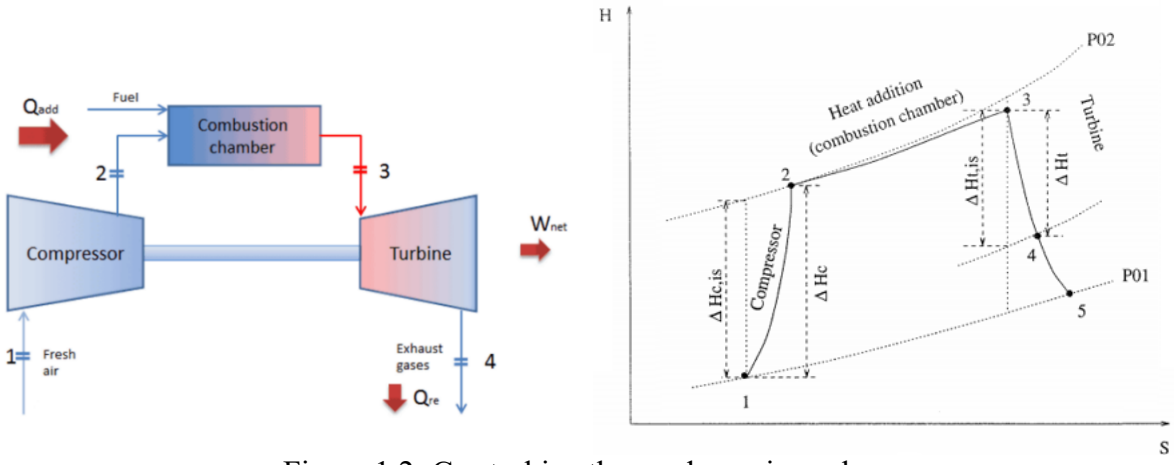

Figure 1.2: Gas turbine thermodynamic cycle

1.2 Modern aero-engine research and HPT stage flow field

The main challenges in modern gas turbine design concern reducing emissions, acoustic pollution, fuel consumption and weight while increasing performance, reliability, and maintainability.

Gas turbines are thermodynamically described by the Brayton cycle, also known as Joule cycle (represented in Figure 1.2). From the analysis of the ideal cycle (dotted line in the figure) is well known that the efficiency depends on the pressure ratio. On the other hand, for real operating conditions, where losses associated with irreversible transformations occur, the efficiency increases with the turbine inlet temperature increase together with the specific thrust output. For this reason, in order to achieve high cycle efficiency, modern engine designers strive to maximize the turbine inlet temperature while safeguarding the integrity of the turbine components through thermal coatings and energy-efficient cooling schemes.

Being placed at the exit of the combustion chamber, the high-pressure turbine (HPT) hosts severe aerodynamic and time-varying heat exchange phenomena (as shown in Figure 1.3), which have a substantial impact on the efficiency and duration of the machine. Indeed, the life-limiting of the component of a modern gas turbine engine is the high-pressure (HP) turbine stage due to the arduous environment. For the same reason, real gas turbine engine operation prevents fundamental research.

For these reasons, energy-expensive cooling strategies are required to keep a limited temperature of the metal (far from the melting point) to avoid creep, and moderated temperature gradients to avoid thermal fatigue, safeguarding the integrity of the HPT components.

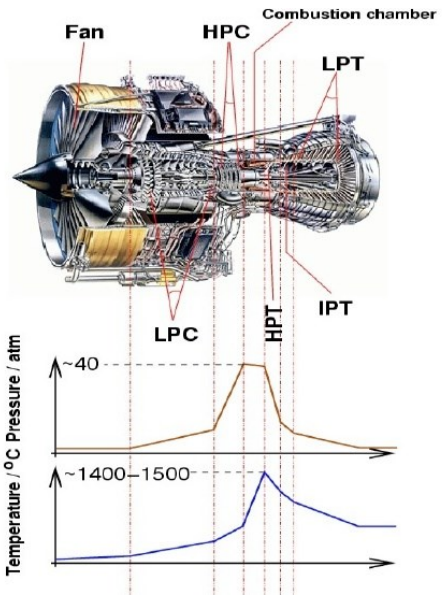

Figure 1.3: Pressure and Temperature evolution of a Rolls-Royce Trent 800

The blade tip design, rotor tip leakage flows, hub design, the inevitable clearance between stationary and rotating parts in turbine stages are crucial aspects for the development of modern aeroengines as they generate high unsteady leakage flows that strongly reduce the engine efficiency and can cause thermally induced blade failures. For these reasons, all these aspects play an important role in the limitation of the turbine's life and performance.

For example, tip clearance losses caused by the small gap between the external case (end wall) and the rotor blade tip, involve a small amount of flow leaks from the pressure side to the suction side through this gap. This leakage flow travels through the blade channel without doing any useful work and hence temperatures remain very high across the blade, leading to high thermal losses and burning of blade tips if no appropriate tip cooling is applied. Since the loading is generally high in modern turbines, the pressure differences between the suction side and pressure side are elevated, thus increasing the importance of these losses. Moreover, the leakage flow interacts with the suction side free stream and forms a tip vortex, also influencing the passage vortex.

Hence, flows in this region are highly complex (high-speed flow, separation, vortex generation), very confined (the tip clearance is usually a small fraction of the blade span) and highly unsteady (f > 10kHz). Therefore, the turbine casing will then be instrumented (see calibration and data reduction in the following chapters) with the aim of achieving a correct thermal characterization of the flow that allows a better understanding of the phenomena described above.

Similar to turbochargers the flow in low-aspect-ratio turbines is dominated by secondary flows in addition to the presence of the blade wake (see Figure 1.4). Strong secondary flows can be expected to cause very hot segments of the mainstream gas to flow into the tip gap region. The high velocity of this leakage flow, rotation-driven work processes and periodic disruption of the end wall boundary layer promote an increase in heat transfer rates from the flow towards both rotor blade tips and casing with highly detrimental effects on the integrity of the components. Due to the elevated heat transfer coefficient in the tip gap, an important quantity of heat is transferred from the tip-leakage fluid to the casing wall.

In this context, the efficiency is influenced by secondary flows interaction, periodic wake impingement on the downstream blade, strong potential field effects, periodic interaction between the vane potential field and rotor exit flow field. Thus, in designing a modern high-pressure turbine, the aerodynamicist must consider each of these sources of blade interaction to decrease and uniformly distribute the heat flux. The consequence of not considering them is the inaccurate prediction of stage performance.

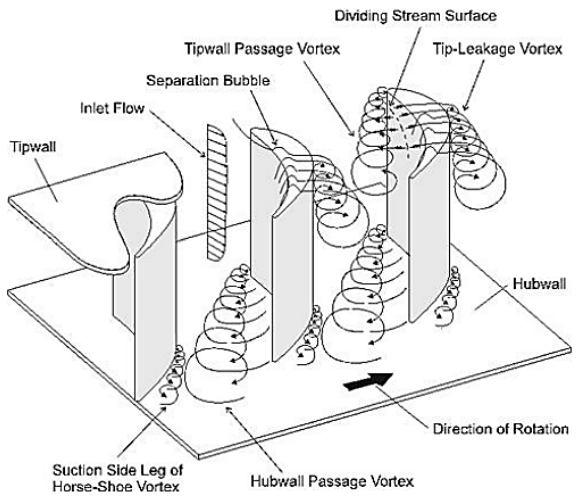

Figure 1.4: Secondary flows representation

1.3 Aims of the project and thesis outline

The widespread use of the gas turbine as a means of aircraft propulsion engine or for electrical power production has provided considerable momentum for improving its efficiency. However, without a greater understanding of the steady and unsteady flow field, in particular, of the flow mechanisms that cause losses, it is difficult to further improve efficiency or quantify the improvement already reached through the new strategy and the use of the optimized configurations. With these aims, in the frame of this thesis, it has been performed both temperature measurements and an experimental investigation of the heat transfer of high-pressure stator vane tested in a short-duration turbine rig. In particular, the aims of the project regard:

- the calibration of the thermocouples probes for the characterization of the flow field at the inlet and outlet of the turbine stage;

- the calibration of the heat transfer insert for characterization of the unsteady heat transfer field at the rotor casing;

- the calibration, the measurements, and the data processing of steady and unsteady heat transfer over instrumented vanes mounted in the test section.

With the aim of contextualizing the work developed within the following thesis, a description of the facility, its test configuration and its operation is provided in the second chapter. Furthermore, the latter presents the theoretical background of the measurement techniques including the fundamental equations available in the literature and most widely used in the turbomachinery field will be given.

The calibration procedure and the measurement uncertainty analysis of the sensors used in the experimental campaign (thin-film heat transfer gauges and thermocouples) are then presented in Chapter 3.

Chapter 4 reports the data reduction of the heat transfer data acquired on a stator vane airfoil in the compression tube and by a fully detailed discussion of the experimental campaign results.

Chapter 5 summarizes the principal achievements and conclusions of this thesis and some suggestions for further improvement of the measurement technique are also given.

Chapter 2

Experimental Methods

2.1 Rotating Turbine Test Rig CT-3

The turbine tests were conducted in the rotating turbine test rig CT-3 of the von Karman Institute (VKI), even nowadays one of the biggest in the world. The work on short-duration heat transfer facilities for turbomachinery applications was pioneered at the Von Karman Institute in 1975 with the installation of the first high-speed linear cascade tunnel (CT-2), for heat transfer measurements, that adopted the principle of the Isentropic Light Piston Compression Tube developed at Oxford University by Schultz et Al. In this facility, the air is compressed in a tube by a free piston and thereby heated up, and subsequently released into the test section through a fast-acting slide valve. To reproduce the actual three-dimensional flow in turbine passages, in 1990, a big annular cascade test rig, capable of full simulation of Mach number, Reynolds number, turbulence intensity and gas/wall/coolant temperature ratios as seen in advanced aircraft engines [3], was built.

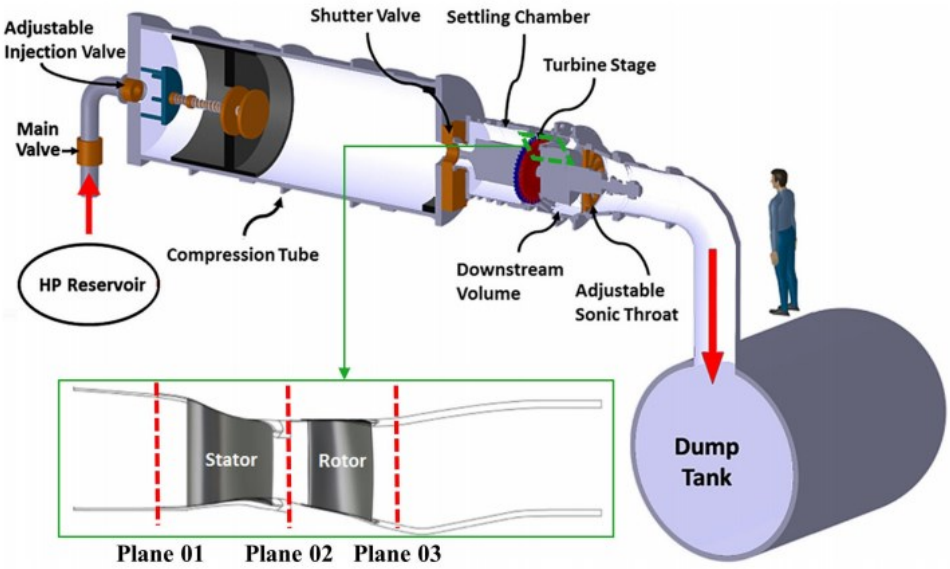

Figure 2.5: Turbine rig and test section

The annular cascade tunnel CT-3 of the von Karman Institute (fully detailed in [1] and represented in Figure 2.5) is a short duration blowdown tunnel that is able to reproduce the actual three-dimensional flow in turbine passages. It consists of three main elements: the compression tube (upstream reservoir), the test section where rotating cascade are assembled and a dump tank (downstream reservoir). A fast-opening shutter valve separates the compression tube from the test section, which is connected to the dump tank via an adjustable sonic throat. The latter is located downstream of the test section and acts to regulate the volumetric flow rate through the facility in order to match the desired pressure and temperature conditions. Indeed, the tunnel is operating at matched conditions when pressure and temperature are maintained constant during the run by tuning the volumetric flow rate into the tube behind the piston equal to that leaving the test section, which is dictated by the area of the variable sonic throat downstream of the stage. An in-house designed control system was implemented to monitor the status of the facility as well as of the main and coolant flows circuit. The system allows the user to select the operating conditions and the different threshold levels to open selected valves following a secured sequence. A second control system monitors the facility operation, by displaying in real-time the pressure and temperature of the oil circuit, rotor vibrations and rotational speed.

Typical test cycle operations (Figure 2.6) start with the shutter valve closed, isolating the test section from the upstream cylindrical reservoir. In the upstream tank, the piston is at the rear of the cylinder and the pressure is regulated to an initial level $P_{initial}$ while the temperature remains atmospheric. By contrast, the downstream reservoir and test section are evacuated to the lowest possible pressure level. Starting at ambient conditions the vacuum pumps allow to achieve 25 mbar (absolute pressure). The high-pressure air from the high-pressure reservoir (at ~ 300 bar) is expanded at the back of the piston into a low-pressure environment.

When the pressure at the back of the piston is one differential above the upstream pressure ($P_{initial}$) the piston starts to slide, and a quasi-isentropic compression is performed between the piston and the shutter, Eq.1.1.

$$T_{f,tube} = T_{i,tube} \left(\frac{P_{f,tube}}{P_{i,tube}}\right)^{\frac{\gamma-1}{\gamma}} \tag{1.1}$$

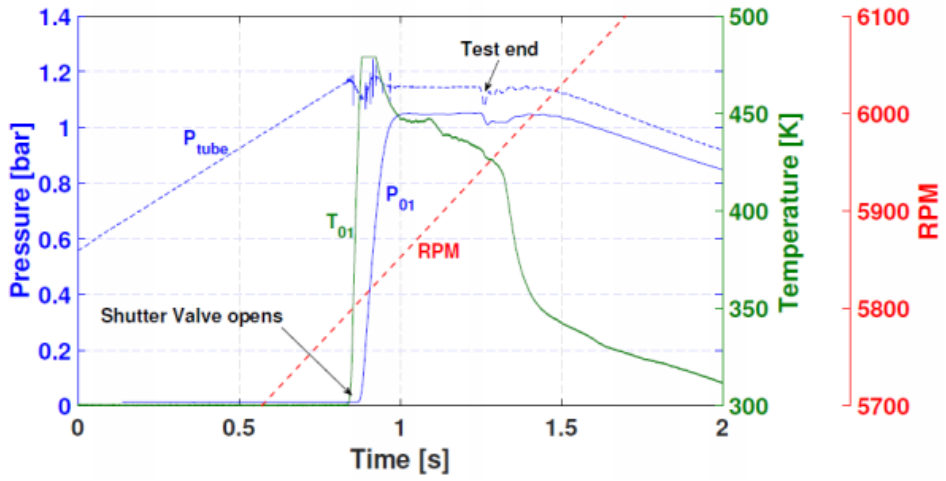

Figure 2.6: Evolution of the main turbine parameters during the test.

Once the specified tube pressure and temperature levels are reached, the shutter valve opens discharging the pressurized and heated air into the test section. The rotor is typically spun up to 90-95 % of the nominal speed (6000 rpm) before the blow-down by means of an auxiliary turbine (disengaged when the right conditions are reached) and accelerates up to about 110-115% of its nominal speed during the test. While the rotor turns the three bearings are lubricated continuously, and vibrations are monitored with two accelerometers, placed next to the front and to the rear bearings.

The turbine inlet total temperature (T01) and pressure (P01) steeply rise to their nominal test values. The typical blowdown covers a time window of 200 ms. During this period, the variation of the rotational speed, the relative inlet flow angle to the rotor and the pressure values allow considering the results as obtained in steady-state conditions. In the present experimental campaign, one operating point has been investigated, whose engine-representative operating conditions are given in Table 2.1.

The test end is identified by a sudden dip in inlet pressure (P01) caused by the closure of the high-pressure line valve. At the test end, the rotor starts decelerating because of ventilation losses, and a small aerobrake on top of the inertia wheel is activated to rapidly decelerate the rotor disk to the rest. The facility is able to simulate the actual operating conditions of transonic and supersonic turbine stages, hence it is designed for the aerodynamic characterization of an HPT (vane + rotor) and can be regulated by adjusting independently Mach (M) and Reynolds (Re) numbers.

Parameters	*Mean*	*Repeatability*	*Units*
$P_{01,\ ms}$	1037.9	±0.7%	mbar
$T_{01,\ ms}$	434.5	±1.3	K
$P_{01}/P_{s3,\ Hub}$	2.195	±0.6%	-
$P_{01}/P_{s3,\ Tip}$	2.214	±0.5%	-
T_{01}/T_{03}	1.239	±1.4%	-
$Tu_{01,\ ms}$	9.03	±3.0%	%
N	5925	±0.3%	rpm
BPF	4700	±14.2	Hz
$Re_{2,\ NGV*}$	6.93×10^5	-	-
$M_{3,\ rel}$	0.78	-	-
$Re_{3,\ r*}$	3.23×10^5	-	-
T_{gas}/T_{wall}	1.5	-	-

Table 2.1: Experimental test conditions

The rotating turbine rig is operated in rainbow-rotor configuration, Figure 2.7. This testing method allows simultaneous measurements on different configurations of blade tip geometries and hub shapes. The turbine stage counts 34 three-dimensional vanes, mounted in a convergent inlet duct, and 48 rotor airfoils.

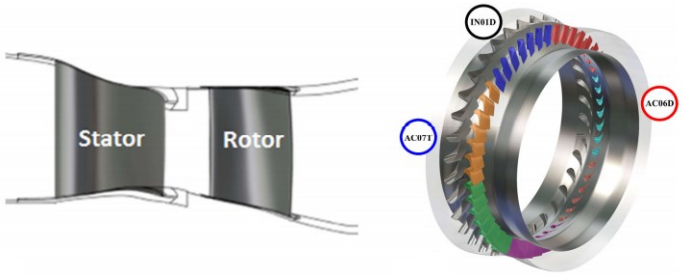

Figure 2.7: HPT stage meridional view and rainbow rotor setup

The 48 rotor airfoils incorporate different baseline profiles. They are distributed in seven distinct circumferential sectors each characterized by a different design combination. Each sector hosts six or seven blades with a specific tip and hub geometry. The rainbow rotor approach was adopted to minimize the measurement error due to test-to-test variations in the rig operating conditions. This turbine setup drastically reduces the number of experiments and offers a cost and time effective solution for testing multiple rotor geometries.

On the other hand, high-frequency aerothermal instrumentation and dedicated data reduction techniques are required to distinguish the different sector signatures, therefore the one-stage HPT test section is heavily instrumented to obtain temperature and heat-transfer measurements.

2.2 Experimental setup

The experimental campaigns in the annular turbine test section of the Von Karman Institute are going to be driven to the calculation of the temperature and the heat flux occurring in the test section. In order to do that two main type of gauges, thermocouples and thin films, have been used whose calibration process will be fully described in the following Chapter.

The inlet and outlet flow conditions within the test section are characterized through the use of reference probes (Figure 2.8 (a)) placed at a fixed radial position (mid span) of the plane 01and 03 (Figure 2.10). Their peripherical position remains the same for all tests during the campaign in order to provide the reference temperature and monitor the turbine operation throughout the test. This type of configuration permits to identify variations from one test to another, evaluating the test-to-test repeatability in the mean of temperature and pressure value.

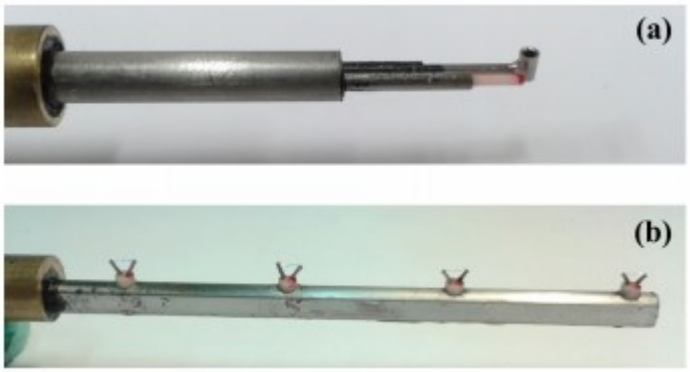

Figure 2.8: Plane 01-03 aerothermal probes: reference probe (a), total temperature rake (b)

In addition, 4-head thermocouple rakes, Figure 2.8 (b) are employed for the measurement of the time averaged total temperature radial profile. Their position along the planes changes each test to characterize the boundary conditions used for the numerical studies. Figure 2.9 presents a qualitative trend of the temperature profile, plotted in the form of experimental points complemented by fitting curve, and normalized by their midspan values.

The temperature trend confirms the predictions according to which the temperature is considerably affected by the presence of the endwalls where the heat transmission is considerably higher, with a measured temperature drop up to 15% $T_{01,\,ms}$ in the near tip region.

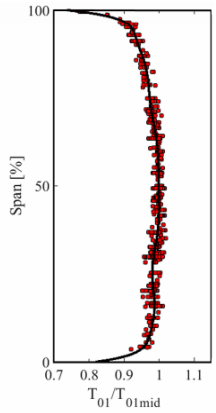

Figure 2.9: Radial profiles of total temperature measured at the stage inlet (Plane 01)

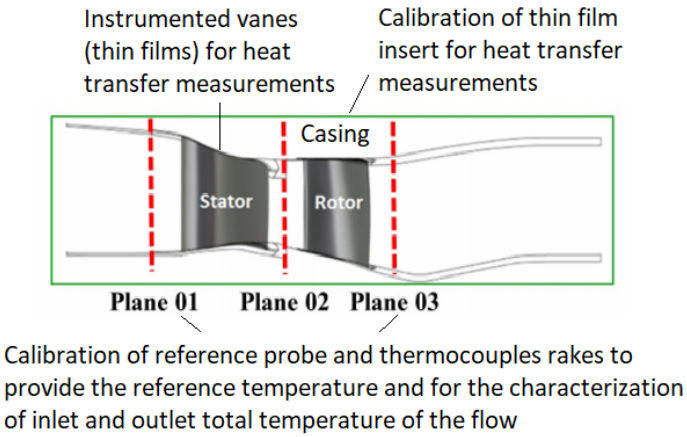

1Figure 2.10: Meridional view turbine stage

Another measurement is done at the end of the compression tube before the shutter valve. As described in Chapter 1 the piston moves forward till desired T and P values are reached and just in that moment the shutter valve open and the blow down starts. To follow the trend of the temperature, a T tube probe (calibrated in the following Chapter) is employed.

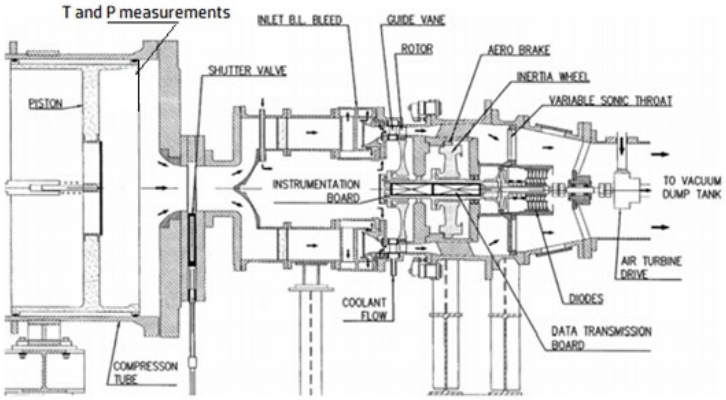

Figure 2.11: Meridional view of CT-3 facility

The amount of the inevitable space between the rotor tip and the casing is determined considering centrifugal forces acting on the blade, creep, thermal expansions of the parts, tolerances, etc. Due to the pressure difference between the suction and pressure sides of a rotor, flow is leaking through this cavity from the pressure to the suction side generating a vortex which will interact with the passage flow. As can be understood, this leakage increases with the increase of the gap and reduces the efficiency of turbine modules. Hence, the crucial aspect of working on the tip region of a rotor is to understand the heat transfer phenomenon over this location since rotor tips are susceptible to thermal damage and oxidation due to high thermal loading [16]. As a consequence, the casing heat flux is investigated by a double layer thin film gauge glued to an insert previously designed, presented in Figure 2.12 and whose calibration will be detailed in Chapter 3 of this paper. The insert thickness has to be large enough to accomplish the semi-infinite condition. The high-frequency temperature gauge is composed of a 200 nm-thick Aluminium element with a resistance of ~50 ohm deposited on a thermally insulating Kapton Polyimide layer. The array is composed by 38 sensors located in different positions of the axial chord of the rotor.

Figure 2.12: Heat transfer casing insert

During the blowdown, a small percentage of the hot gas flowing through the test section towards the cavities which exist upstream and downstream of the rotor disk, shown in Figure 2.13. Hence, inside the chamber, reference probes are placed circumferentially and spaced 120 ° from each other in order to check the axial symmetry of the flow conditions during the test duration. The reference probes allow to verify if the purge flow is able to counteract the high temperature flow that enters the cavity and which would affect the operation of the shaft, the bearings, causing thermal stress on the rotor disc.

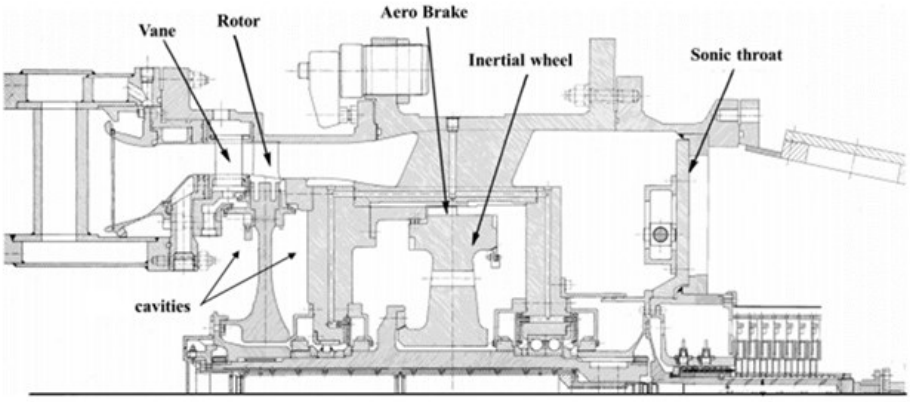

Figure 2.13: High speed turbine test rig (CT3): meridional view

To analyse the heat transfer phenomena occurring and the rotor-stator interaction instrumented vane will be employed with a thin film array who allow to perform the measurements at 50% and 90% of the vane span. At each height, 26 thin film gages mounted on ceramic inserts are distributed along the blade profile. The calibration coefficients and the data processing related to these measurements are reported in the following Chapters.

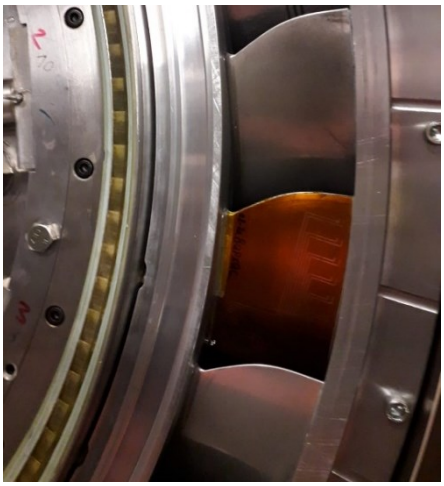

Figure 2.14: Instrumented stator vane

2.3 Theoretical background

2.3.1 Thermocouples

Thermocouples are sensors used to measure temperature, based on Seebeck effect. They consist of two wire legs made from different metals. The wires legs are welded together at one end, creating a junction. This junction is where the temperature is measured. When the two junctions are at different temperature, a voltage is created. The voltage can then be interpreted using the calibration law to calculate the temperature of the hot junction, known the temperature of the cold junction. Among many instruments for temperature measurements, thermocouples (TCs) are routinely and widely used as they provide accurate, relatively cheap, they have a linear calibration curve over a certain useful range, and they are small enough to give a local measurement of the temperature in the flow.

However, their disadvantage stands in a poor frequency response that is approximately up to about 200 Hz, which limits their ability in measuring fast temperature fluctuations that are typical of gas turbines. In this project the thermocouples used are the type K. Type K Thermocouples (Nickel-Chromium / Nickel-Aluminium) are the most common type of thermocouples. They are inexpensive, accurate, reliable, and have a wide temperature range. Their measurement range is from -200 ° C to 1260 ° C and their sensitivity is approximately 41 μV / °C.

The limited dynamic response that characterizes the thermocouples means that the latter are not able to follow the transient phenomena mainly due to the passage of the rotor blades. To overcome this limit in the following project it has been used, in addition, a dual thin film probes whose frequency response reaches 100 kHz.

2.3.2 Data processing methodologies for thin film measurements

This section describes the analytical steps undertaken to measure heat flux in a turbine tested in a blowdown wind tunnel when using a two-layered thin film gauge array. The development of thin film heat transfer gauges started around 1950s for measurements in short duration facilities and a small introduction of the gauges are given by Sieverding et.al.

[4]. These types of gauges are used by many institutions such as VKI, Oxford University, ONERA, MIT, USAF Research Laboratory, PSU, etc. Thin-film gauges were initially used in hypersonic wind tunnels and were subsequently used in turbomachinery research from the 1970s. The sensor consists of a nickel or platinum thermoresistor deposited onto a flexible polyamide substrate that can be easily bounded on a substrate using double sided adhesive.

The assembly constitutes a two layered system. These types of sensors are a highly conductive film whose resistance changes are related to its temperature fluctuations (resistance thermometer). In the range of the temperatures considered here, the relationship between the thin film resistance and its temperature can be expressed as a linear approximation, which is demonstrated in Eq. 2.3.

$$T = a_{\Delta T}\, R + \; b_{\Delta T} \tag{2.3}$$

The sensor placed on a substrate is connected to an Anderson loop that operates under constant current mode and that allows to amplify the small variation in terms of resistance (few Ω) with respect to the thin-film resistance absolute value (50-60 Ω). Its output is proportional to the wall temperature changes in time.

When it is coupled with an appropriate analytical model, and if the wall thermal properties are known, the wall temperature history can lead to the calculation of the wall heat flux history. Due to its small thickness (around 0.2 μm) and length, these sensors are characterized by a negligible thermal inertia and high thermal conductivity that allow that in every instant the sensor temperature corresponds instantaneously to the substrate surface temperature, T_w. One of the greatest advantages of these sensors lies precisely in their frequency response that is typically in the order of 100kHz. Thus, thanks to their fast response, thin film gauges appear suitable for measurements in highly unsteady environments, such as those found in turbomachinery and short duration facility. Indeed, thin-film sensor operated in a transient mode in principle enables very accurate surface temperature measurements to be obtained partly because the gauge is non-intrusive and partly because the high frequency of its response and, thus, it is widely used in short duration facilities. A more exhaustive description of the fundamental theory and its assumptions can be found in [5].

The major drawback for its popular use is the complexity of data reduction procedure which involves the solution of the heat conduction in solids. Among different techniques available, numerical discretization is gaining in importance for several applications basically because of their flexibility in treating boundary conditions and the low computational cost compared to other methods.

The thermodynamic theory suggests the relationship that binds the heat flux that is created between a solid wall and a gas with the difference in temperature and the convective heat transfer coefficient (HTC). Assuming an isentropic arrest of the flow at the probe's wall the convective heat flux at the probe's surface can be written as in Equation 2.4.

$$\dot{q}_w = h(T_T - T_w) \tag{2.4}$$

Where h is the HTC, T_W represents the solid surface temperature while T_T stands for the total temperature of the gas.

This equation is the Newton's cooling law. The statement of Newton's law used in the heat transfer literature puts into mathematics the idea that the rate of heat loss of a body is proportional to the difference in temperatures between the body and its surroundings.

Thin films allow to obtain the gas temperature and the heat transfer coefficient indirectly. In fact, the sensor output does not correspond to these quantities which, however, can be deduced following the knowledge of the wall temperature on the ceramic substrate.

Single layer and double layer thin-film gauges constitute the technical solutions usually employed to implement thin-film sensors into transient tunnels. Initially, in the single layer thin film gauge, the thin film sensor is deposited on a substrate such as quartz or ceramic (Macor). Quartz and Macor are selected because of their thermal properties variation with temperature is less than other insulators (e.g., Pyrex). In addition, the thermal properties of quartz are well documented and Macor can be machined with metal-working tools.

While the single layer probes make use of the sensing element directly applied on a ceramic insulating substrate, in double layer gauges the sensing material is usually deposited onto a flexible polyamide sheet rather than directly onto the substrate. The different structures are highlighted in Figure 2.15.

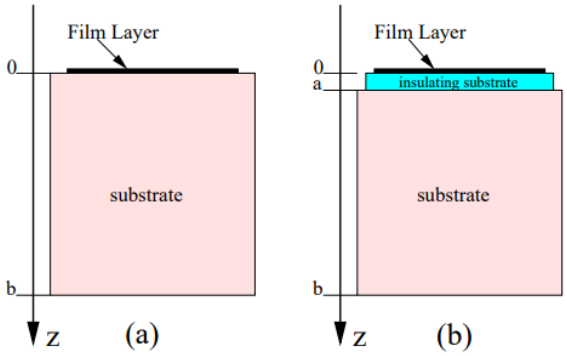

Figure 2.15: Comparison of sensor's structures

The development of the two-layered thin-film gauge allowed faster measurements on rotating components with a more flexible implementation. A cross section through a two-layer thin-film gauge is shown in Figure 2.16.

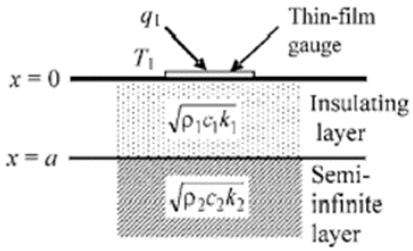

Figure 2.16: Two-layer heat transfer gauge

2.3.2.1 Numerical method

In this case, the heat flux is derived from the unsteady wall temperature measurements using a Crank-Nicholson scheme. To obtain the analytical solution of the problem two main hypothesis have been assumed:

1. The first one concerns the mono-dimensional model. The hypothesis is that of one-dimensional heat transfer, assuming therefore the non-existence of lateral heat losses.

2. The second one refers to the semi-infinite model. The semi-infinite principle implies that during the transient operation of the thin film gauge, the temperature on the back side of the gauge substrate remains equal to its initial value prior to the experiment. Thus, the thickness of the substrate should be large enough, so that the conductive heat transfer does not penetrates till its back side. This means that the total depth of the substrates is such that at a given depth > l_{TP}, the temperature can be considered as constant during the short testing time.

$$\dot{q} = 0 \; for \; x > \; l_{TP}, where \; l_{TP} \; represents \; the \; thermal \; penetration \; lenght$$

L_{TP} can be calculated with Equation (2.5):

$$L_{\infty} = 3.74\sqrt{\alpha t} \tag{2.5}$$

The classical data reduction technique used for double-layered thin-film gauges (Figure 2.17) comprises the resolution of the 1D unsteady heat conduction equations in a multi-layered substrate (2.6):

$$\frac{1}{\alpha_1(x)}\frac{\partial T_1(x,t)}{\partial t} = \frac{\partial^2 T_1(x,t)}{\partial x^2}$$

$$\frac{1}{\alpha_2(x)}\frac{\partial T_2(x,t)}{\partial t} = \frac{\partial^2 T_2(x,t)}{\partial x^2} \tag{2.6}$$

where the temperature is T at a distance x from the surface, at time t and α is the diffusivity of the material defined in terms of the thermal conductivity (k), the density (ρ) and the specific heat (c): α = k /ρ c. The suffixes 1 and 2 refer to the slab and backing material, respectively, in fact each layer is characterized by different values of density (ρ), specific heat (c) and thermal conductivity (k).

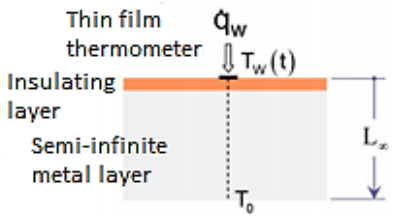

Figure 2.17: Scheme of 1D semi-infinite approach

To solve this equation, a set of initial and boundary conditions are needed. The wall temperature evolution measured with the thin film gauge is imposed $T_w(0, t)$.

Assuming that the last substrate is semi-infinite (for the second hypothesis), a second boundary condition is obtained: $T(x \to \infty, t) = T_0$. This assumption is valid as long as the test duration is sufficiently short.

In the case of multilayer substrates, an additional boundary condition ought to be imposed at the interface each substrate, namely, the heat flux continuity:

$$-k_1 \frac{\partial T_1(t)}{\partial x}\Big|_{x=L^-} = -k_2 \frac{\partial T_2(t)}{\partial x}\Big|_{x=L^+}$$

$$T_1(x = L^-, t) = T_1(x = L^+, t) \tag{2.7}$$

Where L represents the depth of the interface.

A Crank–Nicholson numerical discretization is employed to solve the 1D unsteady heat conduction equation. It provides the temperature field in the substrate at every time step and, subsequently, the wall heat flux at the gauge location thanks to the Fourier law:

$$\dot{q}_w(t) = -k_1 \frac{\partial T_1}{\partial x}\Big|_{x=0} \tag{2.8}$$

Taking the Laplace transforms, denoted by – we obtain:

$$\frac{p}{\alpha_1}\overline{T_1} = \frac{\partial^2 \overline{T_1}}{\partial x^2} \tag{2.9}$$

$$\frac{p}{\alpha_2}\overline{T_2} = \frac{\partial^2 \overline{T_2}}{\partial x^2} \tag{2.10}$$

Where $p = e^{\sigma + j\omega}$. Which give the general solutions:

$$\overline{T_1} = A\, e^{x(\frac{p}{\alpha_1})^{1/2}} + Be^{-x(\frac{p}{\alpha_1})^{1/2}} \tag{2.11}$$

$$\overline{T_2} = C\, e^{x(\frac{p}{\alpha_2})^{1/2}} + De^{-x(\frac{p}{\alpha_2})^{1/2}} \tag{2.12}$$

Using the boundary conditions to eliminate the constants from Equations we obtain:

$$\bar{T}_1 = \frac{\overline{\dot{q_w}}\sqrt{\alpha_1}[(1+a)e^{-(x-l)\sqrt{\frac{p}{\alpha_1}}}+(1-a)e^{(x-l)\sqrt{\frac{p}{\alpha_1}}}]}{k_1\sqrt{p}[(1+a)e^{l\sqrt{\frac{p}{\alpha_1}}}-(1-a)e^{(-l)\sqrt{\frac{p}{\alpha_1}}}} \tag{2.13}$$

$$\bar{T}_2 = \frac{2\overline{\dot{q_w}}\sqrt{\alpha_1}\, e^{(l-x)\sqrt{\frac{p}{\alpha_2}}}}{k_1\sqrt{p}[(1+a)e^{l\sqrt{\frac{p}{\alpha_1}}}-(1-a)e^{(-l)\sqrt{\frac{p}{\alpha_1}}}} \tag{2.14}$$

Where $$a = \sqrt{\frac{\rho_2 c_2 k_2}{\rho_1 c_1 k_1}}$$

The transformed time derivatives of temperature are given by the equation:

$$\frac{\partial \bar{T}}{\partial t} = p\bar{T} \tag{2.15}$$

Considering the boundary and the initial conditions listed so far and assuming that the surface measuring film has negligible effect on the heat conduction process, the surface temperature of the substrate may be found by putting l=0 in Equation (2.14) and the temperature then becomes:

$$\bar{T}_x = \frac{1}{\sqrt{\rho c k}}\frac{\overline{\dot{q_w}}}{\sqrt{p}}\, e^{(-x)\sqrt{\frac{p}{\alpha}}} \tag{2.16}$$

And inverting the transform:

$$T_w = \frac{1}{\sqrt{\pi}\sqrt{\rho c k}}\int_0^t \frac{\dot{q_w}(\tau)d\tau}{t-\tau} \tag{2.17}$$

Equation (2.17) represents the temperature evolution in time at the surface (x=0) caused by the step in heat flux. Being the heat transfer rate constant, Equation (2.17) above reduces to:

$$T_w(t) = \frac{2\dot{q_w}}{\sqrt{\pi}}\sqrt{\frac{t}{\rho c k}} \tag{2.18}$$

And it is seen that under such conditions the surface temperature is parabolic in form.

Details of the approaches and solutions for different cases such as step in wall heat flux and step in fluid temperature can also be found in Schultz and Jones [5].

The complete analytical solutions for temperature T (x, t) and heat flux q (x, t) are, hence, the following:

$$T(x,t) = \frac{\dot{q_w}}{\sqrt{\rho c k}} \left[\frac{2\sqrt{t}}{\sqrt{\pi}} \exp\left(\frac{-x^2}{4\alpha t}\right) - \frac{x}{\sqrt{\alpha}} \, erfc\sqrt{\frac{x^2}{4\alpha t}} \right] \tag{2.19}$$

$$\dot{q}\,(x,t) = -k\frac{\partial \mathrm{T}}{\partial x} = \dot{q_w}\, erfc\sqrt{\frac{x^2}{4\alpha t}} \tag{2.20}$$

These solutions could be applied to the problems that refers to the heat transfer processing on the rotor casing.

While for the study of the heat transfer of the vane the reference temperature is the inlet one, for the study of the heat transfer to the casing it could be necessary to calculate the adiabatic wall temperature because it is not possible to take the inlet temperature as a reference because of the leakage flow that occurs between the casing and the blade which involves the increase of local T due to the fact that no work is extracted from the fluid which, however, passing from the pressure side to the suction side accelerates in that section and therefore undergoes a pressure reduction and a not negligible increase in temperature.

Therefore, the measurement of the heat flux alone is not sufficient to elucidate the physical origin of the heat transfer variations, which in turn are the boundary conditions to design the cooling schemes. Hence, the accurate measurement of the adiabatic wall temperature and the adiabatic local convective coefficient becomes essential to ensure a correct thermal assessment of any turbine hardware. The adiabatic wall temperature is necessary due to the inability to measure the gas temperature in the clearance between the casing and the rotor blade and the highly unsteady nature of the heat transfer at this location.

As explained in Thorpe and Ainsworth [6], the unsteady effects can contribute to 15% of the total heat flux at the tip region.

Due to this reason, it is required to measure not only the average temperatures but also the temperature fluctuations in this region.

Normally, it is possible to use cold wire resistance thermometer for such a measurement; however, it is not possible to place such a device between the tip and the casing for dimensional issues. Therefore, instead of the gas temperature at that location, the use of the adiabatic wall temperatures is essential. In this way the HTC is only function of the geometry and flow field and no more related to the thermal conditions of the heat transfer surface.

As proposed in [7], Newton's cooling law (Eq. 2.4) can be rewritten as reported in Equation 2.21:

$$\dot{Q}_w = h_{aw}(T_{aw} - T_w) \tag{2.21}$$

The adiabatic wall temperature (T_{aw}) can be defined as the temperature that forces the heat flux at the wall to be equal to zero, or, in other words, as the temperature of the body in a flow under adiabatic condition. Therefore, the adiabatic wall temperature (T_{aw}) is determined as the wall temperature that yields zero heat flux.

In order to obtain these values with a test campaign, the plot of time mean heat flux versus wall temperatures has to be evaluated as described in Pinilla et.al. [9]. The surface is heated by resistances from inner side to get different T_w of the body. By changing the surface temperature using the heaters, it is possible to obtain different points for each test performed and build the linear regression interpolating the data extracted from the experiments.

The slope of this interpolating line represents the heat transfer coefficient while the point of intersection with the horizontal axis reveals the adiabatic wall temperature as shown in Figure 2.18. The value of the heat flux at the wall will depend only on the so-called thermal product. For this reason, the accuracy on the heat flux is directly linked to the accuracy on the two thermal products of the two substrates. Additionally, the thickness of the first layer L is the third parameter that determines the accuracy of the heat flux calculations. Lavagnoli et.al. [8] carried out a detailed uncertainty analysis for such sensors and approach.

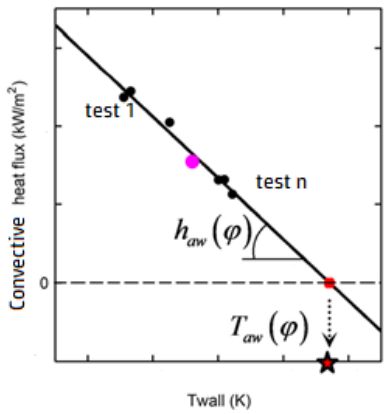

Figure 2.18: Example of data interpolation and linear regression

2.3.2.2 Filter method

The hypotheses so far considered valid, however, cannot be considered in the case of the heat transfer studied on the stator blades. The vanes, in fact, unlike the insert used in the casing, at the leading edge, are characterized by a curvature that is too wide to be able to consider the hypothesis of one-dimensionality to be true. Moreover, the vane thickness becomes smaller as the measurements move towards the trailing edge and thus, the assumptions taken for a semi-infinite body approach where we have negligible conduction in the substrate, might not be as applicable as before. For this reason, the numerical solution that will be used in this case, illustrated later, differs from that treated in the previous paragraphs.

In this case a new, computationally efficient method [10] will be used to analyse and process transient thin-film heat transfer gauge signals. The new method uses known pairs of exact solutions, such as the T response due to a step in q, to derive a sampled approximation of the impulse response of the gauge system. This impulse response is then used as a finite impulse response digital filter to process the sampled T signal to derive the required sampled q signal. This is computationally efficient because the impulse response need only be derived once for each gauge for a given sample rate, but can be reused repeatedly, using optimized MATLAB filter routines and is highly accurate.

The impulse response method can be used for most types of heat flux gauge. In fact, the method is universal for any linear measurement systems which can be described by linear differential equations where theoretical solution pairs exist between input and output.

This method allows to overcome the limits related to the use of numerical solutions that use a Crank-Nicholson scheme which, even being powerful, presents a high computational cost and may have difficulties in encompassing short and long time-scale phenomena in the same calculation. Indeed, for the most heat transfer gauge systems the new impulse response method is more efficient, simpler, and more accurate than the methods described above.

In detail, the impulse response method uses discrete deconvolution to derive filter impulse responses of the same length as the data being processed from analytically derived response functions [11]. The response of any linear time invariant system such as a thin-film gauge can be calculated from the impulse response h(t) of that system by the convolution integral:

$$q(t) = h(t) * T(t) = \int_{-\infty}^{\infty} h(\tau)T(t-\tau)d\tau$$

To avoid the singularities at the origin the convolution integral is replaced by the discrete convolution sum that can be carried out by the Matlab *fftfilt* function. In this way the discrete convolution becomes:

$$q[n] = h[\mathrm{n}] * T[\mathrm{n}] = \sum_{k=0}^{N-1} h[\mathrm{k}]T(n-k) \qquad for\ k = 0, 1, 2, \dots, N-1$$

The impulse response function sequence h[n] (that represents a sampled approximation to the continuous impulse function h(t)) can be obtained knowing a pair of non-singular analytical solutions $q_1(t)$ and $T_1(t)$ for the underlying heat transfer equations in the gauge substrate. In particular, for double layer heat transfer probes, an analytical solution exists in case of step in heat flux. Doorly and Oldfield provide the solution [12]:

$$T_w(t) = T_i + \frac{2\dot{q}_w}{\sqrt{\rho ck}}\left\{\sqrt{\frac{t\prime}{\pi}} + 2\sum_{n=1}^{\infty} A^n \left[\frac{\sqrt{t\prime}}{\sqrt{\pi}} \exp\left(\frac{-n^2 l^2}{\alpha_1 t\prime}\right) - \frac{nl}{\sqrt{\alpha_1}}\, erfc\frac{nl}{\sqrt{\alpha_1 t\prime}}\right]\right\} \qquad (2.22)$$

$$A = \frac{1-\sigma}{1+\sigma} \qquad \sigma = \frac{\sqrt{\rho_2 c_2 k_2}}{\sqrt{\rho_1 c_1 k_1}} \qquad t' = t - t_0$$

These solutions can be sampled and are then related to the required impulse response by the convolution:

$$q_1[n] = h[\mathrm{n}] * T_1[\mathrm{n}]$$

h[n] can then be found by deconvolution, using the MATLAB function *filter*, using the discrete impulse function δ[n]=1, 0, 0, …. Whose z transform is $\Delta(z)$

As described by Denbigh [12] the use of the z transform allows to replace the convolution operator with the multiplication operator:

$$Q_1(z) = H(z)T_1(\mathrm{z})$$

Convoluting the impulse response with an impulse function will, by definition, simply reproduce the impulse response, so that in the z transform domain: $H(z) = \frac{Q_1(z)}{T_1(\mathrm{z})}\Delta(z)$

Thus, the required impulse response can be obtained by digitally filtering the impulse function δ[n] by the infinite impulse response (IIR) filter whose coefficients are given by Q1(z)/T1(z) using the MATLAB function h = filter (q1, T1, impulse)

This h[n] was evaluated once considering the appropriate set of heat transfer gauge parameters (sampling rate, sampling time, layers' thermal properties…), and then subsequently used to process sampled data by using the fast function *fftfilt* in the Matlab signal processing toolbox.

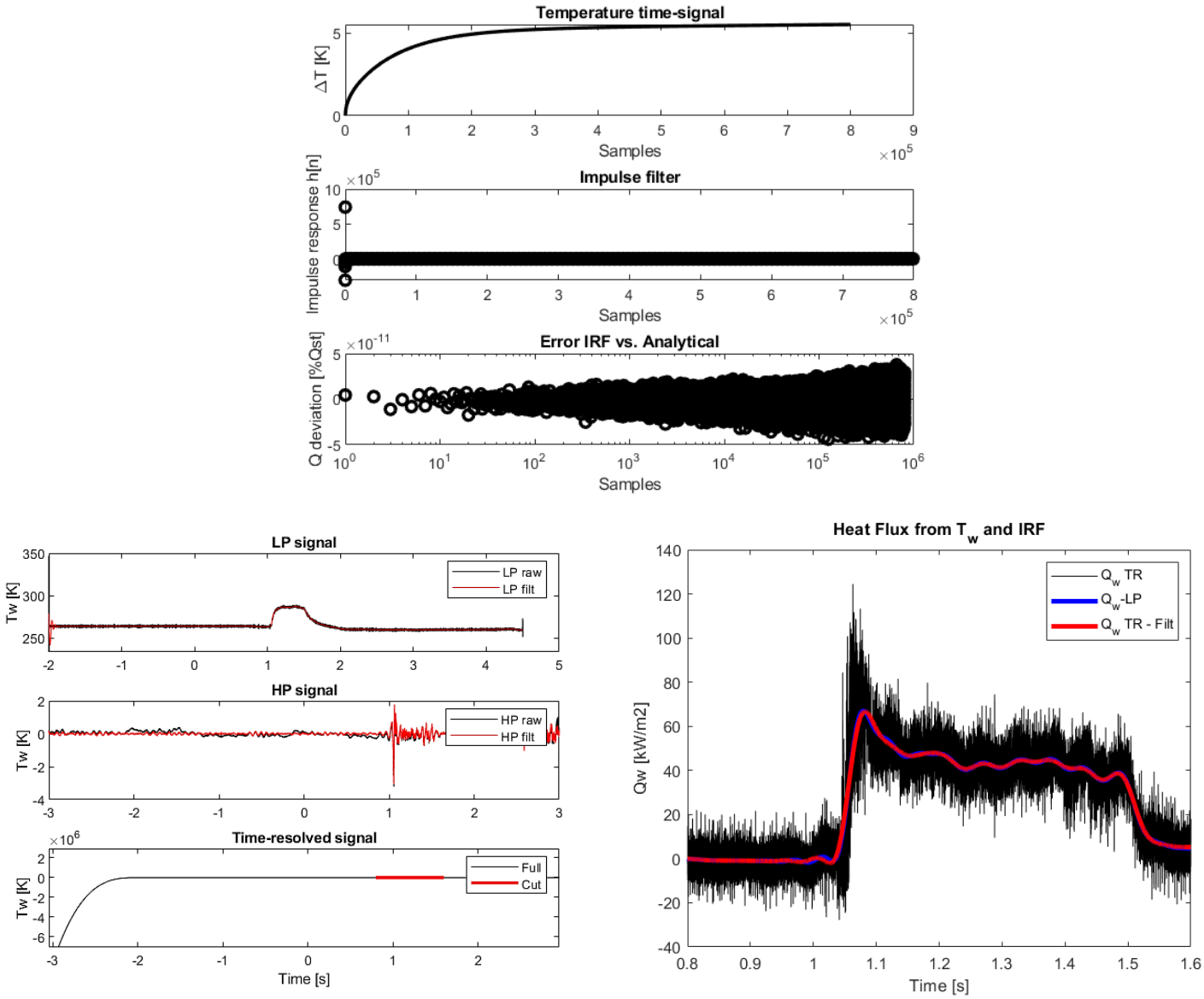

Figure 2.19: Impulse response function and heat flux derived from Tw signal

Chapter 3

Static calibration

3.1 Thermocouples static calibration

The calibration of these gauges is necessary in order to get a correlation between the temperature and the voltage values. In this way applying the calibration law to the signals, it will be possible to convert volts to the correspondent measurement unit (K or °C).

The thermocouples that were used to measure the temperature between the turbine internal casing and the facility external casing were calibrated in a test chamber while the reference and the rakes probes were calibrating in an oil bath to obtain the most accurate results. The complete results containing the calibration coefficients of all sensors used are summarized in Table A1 in Appendix A.

Concerning the first calibration, to perform it, the thermocouples were positioned in a climatic test chamber SYSTEM WEISS TYPE WKL 34/40 (that uses PT100 as reference resistance thermometer) and they were connected at two digitizers (Ametek EX1401) that allow to acquire and digitalize the signal as shown in the Figure 3.20.

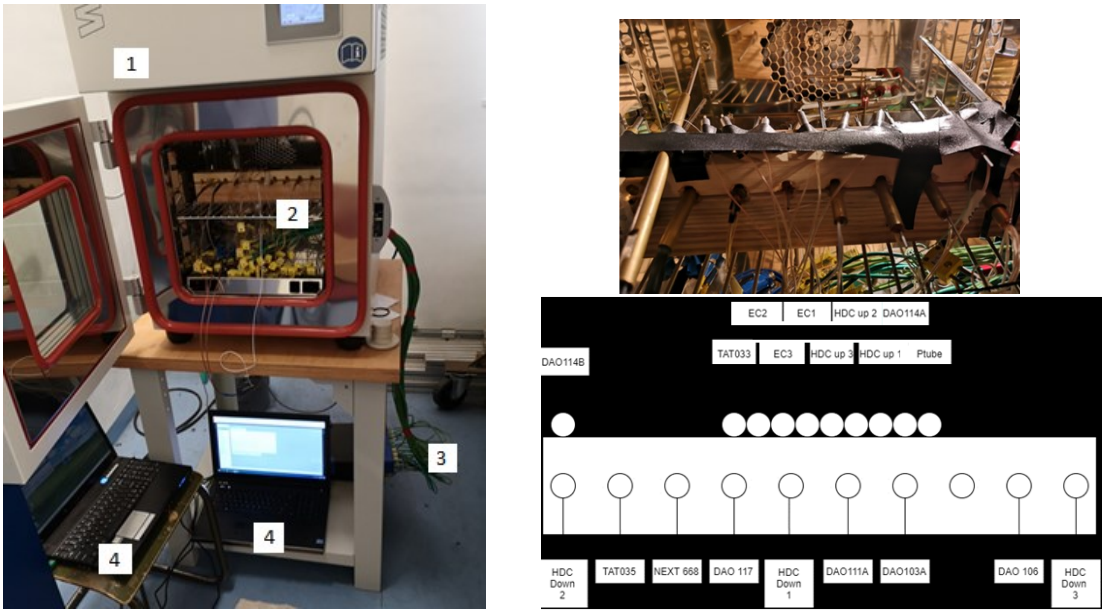

Figure 3.20: Set up for the calibration procedure: 1=test chamber, 2=thermocouples, 3=digitizer, 4=acquisition system

The calibration covers a range from 25°C to 70°C in steps of 5°C. The temperature does not reach 75°C due to the presence in the thermocouples of a glue that has a limitation in temperature. In order to achieve specified performance, all instruments should achieve thermal stability before proceeding to calibration. For this reason, it is required to power-up all instruments for the warmup duration time, as recommended in their manuals. Thermal equilibrium must be reached inside the chamber for each set temperature in order to give the proper time to the probes to stabilize. The analysis based on the measured transient behaviour of the temperature, shows that it is necessary to wait at least 40 minutes to obtain a stable voltage and temperature as represented in Figure 3.21. The acquisition starts when the maximum temperature oscillations are smaller or equal to 0,04°C/ 20 minutes around the target temperature.

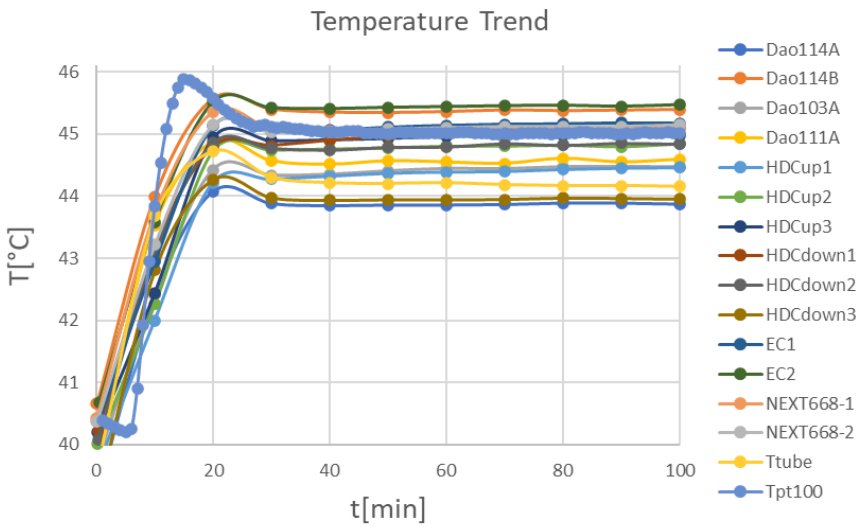

Figure 3.21: Thermocouples and test chamber temperature trend between 40°C and 45°C

When the probes reached the thermal equilibrium the voltage signals were acquired from the digitizer at frequency of 100 Hz for 10 seconds (high frequency for a small time to have a statistical significance), in this way 1000 voltage values were obtained which were averaged over time so as not to consider the oscillations of the signals due to the noise. The signals are acquired using a 24-bit acquisition board that provides a resolution of 13.5 nV of the measured sensor signals.

The voltage was then compared with the corresponding temperature given by the reference temperature of the PT100 positioned inside the oven. This allows a T− V curve to be built. The slope and the intercept of each linear correlation between temperature and voltage can be found and the coefficient of determination can be computed to find the goodness of the fit. The coefficient of determination (R^2) gives an idea of how many data points fall within the results of the line formed by the regression equation. An R^2 of 1 means that the dependent variable can be predicted without error from the independent variable.

The calibration law is expressed as in Equation 3.23, average values are summarized in Table 3.2 and graphically reported in Figure 3.22. The correlation coefficient value, R^2, indicates that the 1st order polynomial curve fit is thus suitable for measurements.

$$T_{PT} = m \cdot V_{TC} + q \tag{3.23}$$

Operating condition	$\bar{m}$ [°C/V]	$\bar{q}$ [°C]	$\overline{R^2}$
Calibration performed _ test chamber	25287,42	22,58	0,99977

Table 3.2: Linear regression coefficients, slope, intercept and R2

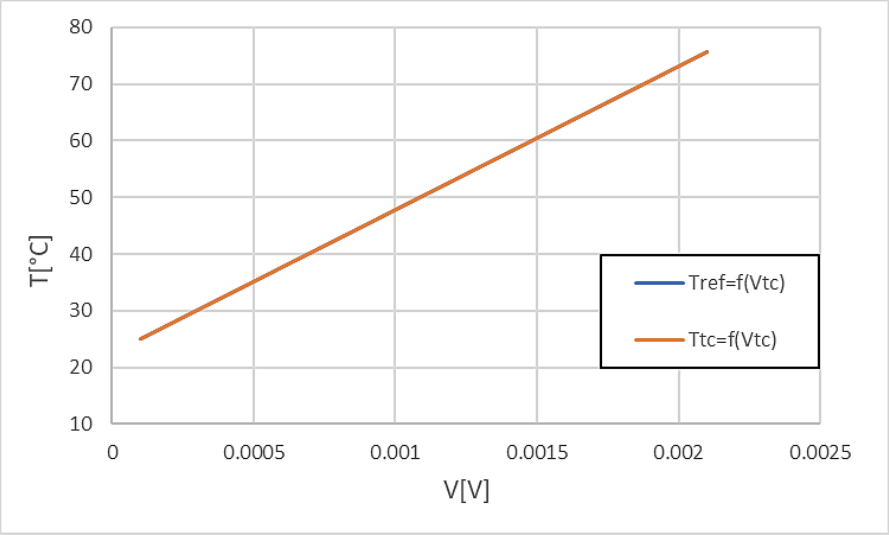

Figure 3.22: Calibration law average value

The digitizers can return both temperature and voltage as output. Hence, acquiring the voltage and the temperature sequentially, it is possible to evaluate the goodness of the digitizers' internal calibration, compering the voltage with the temperature acquired with the digitizer and not with that of PT100.

Both calibrations were compared for each thermocouple as shown in Figure 3.23. The comparison in terms of temperature for each prob is shown in Figure A1 presents in Appendix A.

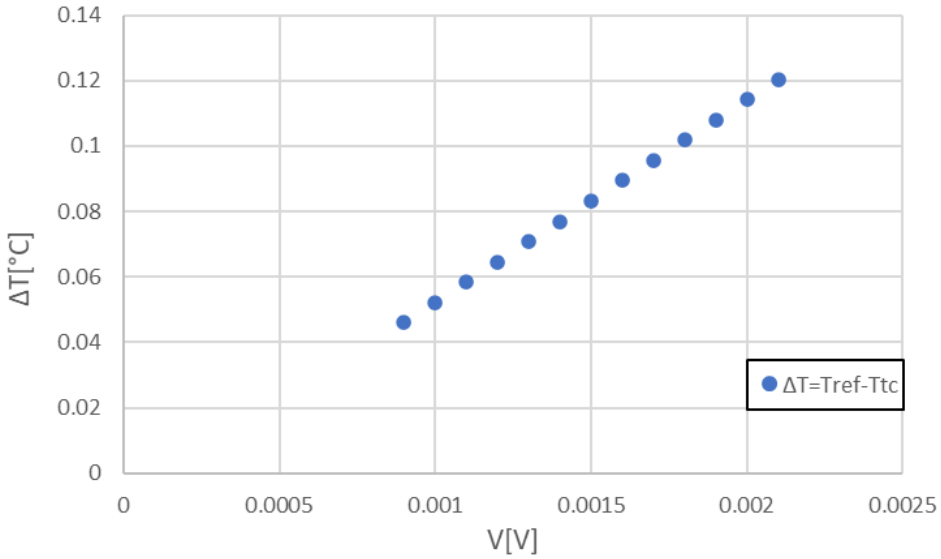

Figure 3.23: Comparison between digitizer's internal calibration and reference one

The average variation of the parameters by comparing the two calibrations is shown in the Table 3.3. It is recommended to perform the calibration in order to obtain more accurate results than those provided by the Ametek 1401 digitizers.

Operating condition	$\bar{m}$ $[°C/V]$	$\bar{q}$ $[°C]$	$\overline{R^2}$
Calibration performed _ ref	25287,42	22.58	0,99977
Digitizer calibration _ tc	25225,33	22.59	0,99973
Δ [%]	-0,25	0,04	-0,004

Table 3.3: Comparison linear regression coefficients between the ref and the digitizer calibration

To consider and evaluate the real temperature distribution inside the test chamber, it was necessary to analyze its spatial calibration. The development of an algorithm in MATLAB allowed to describe the temperature variations (assuming a linear trend) in each position of the climatic chamber compared to the PT100 temperature placed in front of the fan inside the test chamber as shown in Figure 3.24, where the black circles represent the positions of the probes.

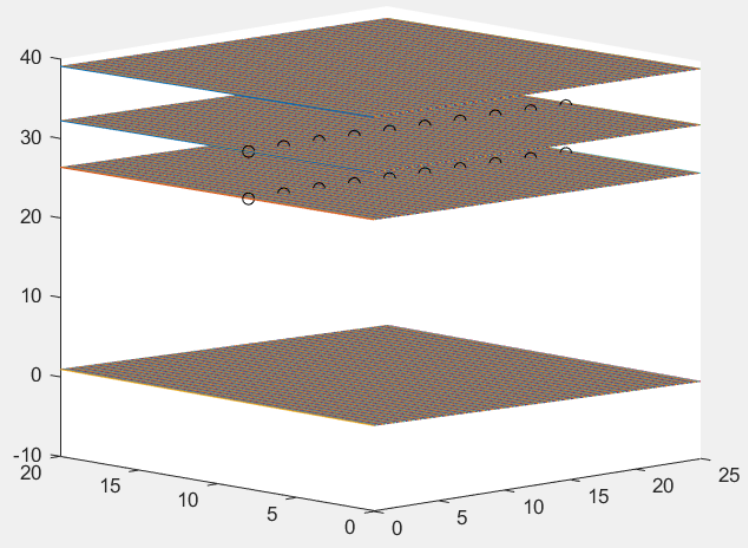

Figure 3.24: Temperature variation in the two lying planes of the thermocouples

Imposing the proper ΔT for each thermocouple, Table 3.4 reports the changing in each parameter applying this correction.

Operating condition	$\overline{m\_ref}$ [°C/V]	$\overline{q\_ref}$ [°C]	$\overline{R^2\_ref}$
Test chamber _ no ΔT correction	25287,42	22,58	0,99977
Test chamber _ ΔT correction	25287,42	22,37	0,99977
Δ [%]	-	-0,94	-

Table 3.4: Comparison between linear regression coefficients applying the spatial calibration or not

The results in Table 3.4 highlight that the only parameter that is subjected to a change is the intercept while the changing in the slope and the coefficient of determination can be considered neglectable.

To improve the accuracy of the reference temperature to which each probe is subjected, the setting conditions have been changed. While the first calibration was carried out placing all the thermocouples in the support directly exposed to the air flow from the fan, the second calibration was performed placing the probes inside a casing. This was done to ensure a better temperature homogeneity and to prevent that the air coming from the test chamber's fan from altering the measurement. Furthermore, in the second calibration, instead of taking as reference the PT100 temperature, an additional PT100 was positioned in the centre of the box, in close proximity to the probe, in order to compare as much as possible, the voltage with the temperature to which the thermocouples are subjected.

The results shown in the Figure 3.25, Figure 3.26 and Table 3.5 draw the attention to how the presence of the casing and the new reference probe allow to decrease the standard deviation by 80% and the uncertainty by 51% as will be illustrated in detail in the paragraph 3.1.1.

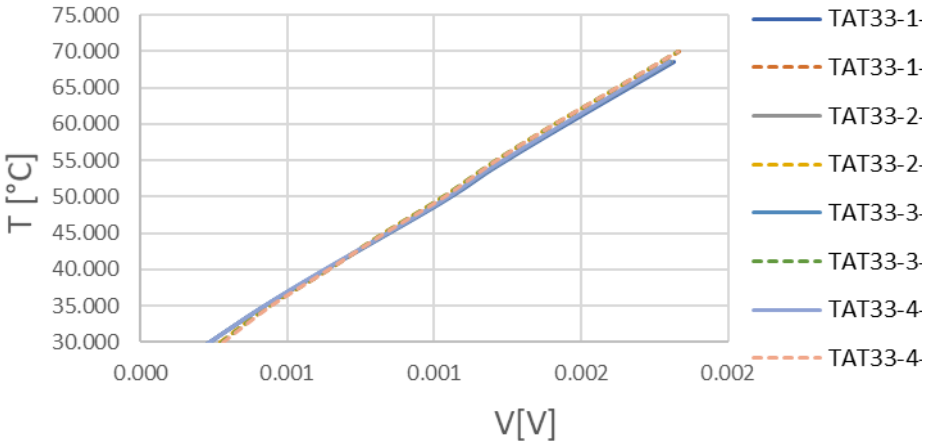

Figure 3.25: Comparison between calibration law performed with the casing (continuous line) and the one without the casing (dashed line)

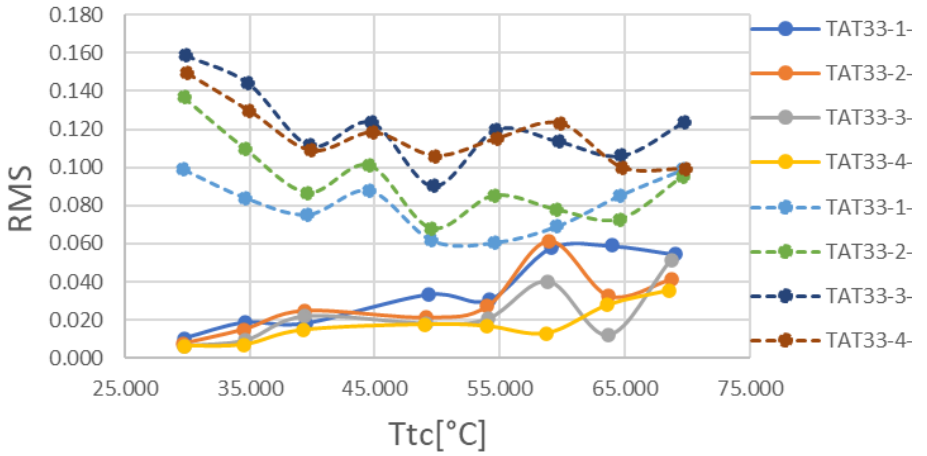

Figure 3.26: Comparison between standard deviation trend related to the calibration performed with the casing (continuous line) and the setting without the casing (dashed line)

Operating condition	$\overline{m\_ref}$ [°C/V]	$\overline{q\_ref}$ [°C]	$\overline{R^2\_ref}$	$\overline{RMS}$
test chamber _no casing	25320,34	23,43	0,99966	0,067
test chamber _casing	24845,79	24,21	0,99979	0,0134
Δ [%]	-1,87	3,32	0,013	-80,06

Table 3.5: Comparison between calibration coefficients performed with the casing (continuous line) and the one without the casing (dashed line)

For the reference and the rake probes the calibration was performed in the Isotech calibration bath respectively in a dry mode and in a liquid mode to obtain more accurate results. The experimental setup, composed by an Isotech calibration bath, a PT100, Ametek ex1401 digitizer and thermocouples is shown for both case in Figure 3.27. The Isotech calibration bath is a small electrical oven, in which a cylindrical container is inserted and heated up. This container, made of aluminium, is specifically shaped to be in contact with the oven walls, and allows the insertion of 6 probes and a PT100 at the same time. The calibration was performed between 25°C and 70°C with step of 5°C. Given the temperature limit set by the glue and insulating insert. A total of 10 measurement points were taken from ambient to 70°C and a linear regression was performed with the voltage acquired through the Ametek digitizer. A calibration law for the temperature in the form of equation 3.23 was found and the results, are reported in Table 3.6.

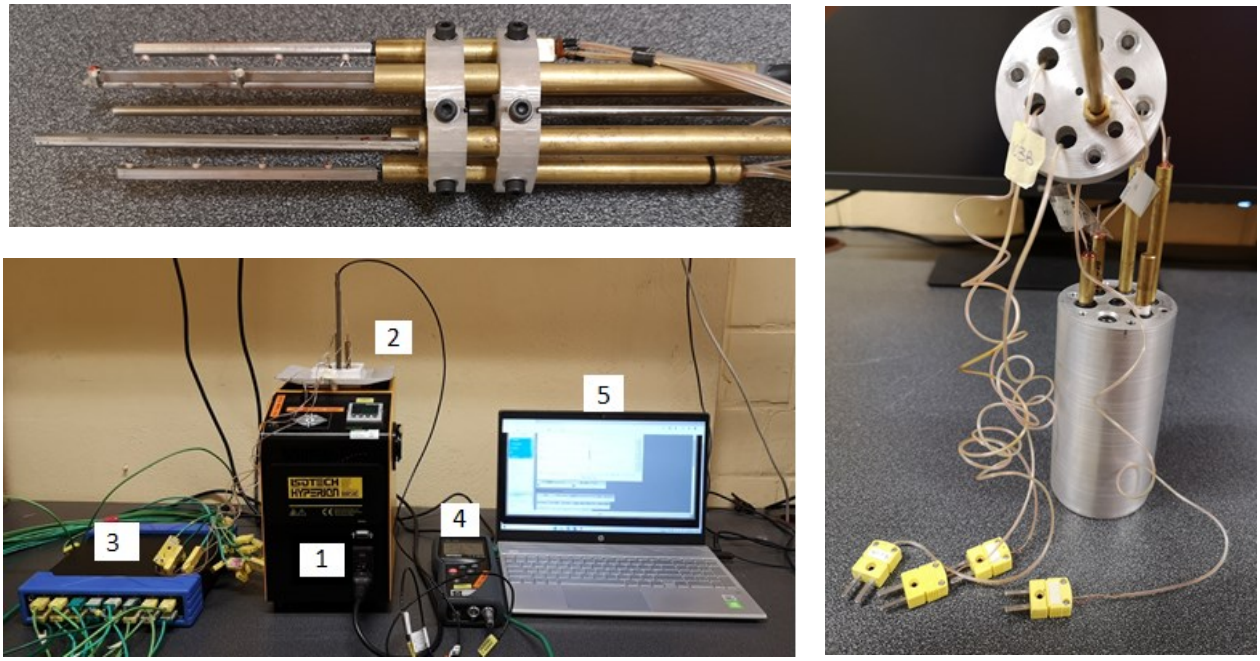

Figure 3.27: Set up for the calibration procedure: 1=Isotech bath, 2=thermocouples, 3=digitizer, 4=reference probe (PT100), 5=acquisition system

Operating condition	$\overline{m\_ref}$ [°C/V]	$\overline{q\_ref}$ [°C]	$\overline{R^2\_ref}$
Oil bath _ dry and liquid mode	24242,31	25,10	0,99996

Table 3.6: Average calibration coefficients for oil bath calibration

The increasing of the R^2 value demonstrates the importance of calibrating within the oil bath in order to obtain more accurate parameters.

Residual analysis has been used to assess the appropriateness of a linear regression model by defining residuals and examining the residual plot graphs. Residual refers to the difference between observed value vs predicted ones. The residual plot (Figure 3.28), in which residuals are on the vertical axis and the independent variable is on the horizontal axis shows that even if the values are not completely randomly dispersed around the horizontal axis, being in the range of the tenth of a degree it is possible to consider the appropriate regression model for data analysis.

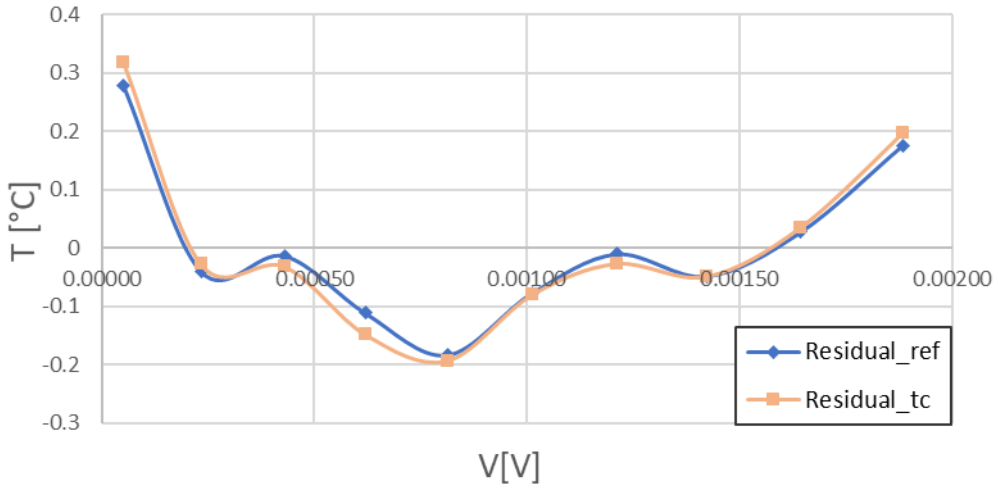

Figure 3.28: Calibration law

3.1.1 Uncertainty analysis thermocouples calibration

For the assessment of a good level of confidence on the measurements and on the corresponding data reduction, the calculation of the uncertainty plays an important role as represents an estimation of their accuracy. The uncertainty is defined as the most probable value that the error can be within a certain interval of confidence.

It is possible to distinguish two sources of error: systematic and random. As described in [13], measurement uncertainty analysis is a function of the measurement system therefore it is necessary to completely define the measurement system before proceeding with an uncertainty analysis. After that definition error sources may be treated as either random (precision) or systematic (bias).

Random error sources always cause scatter in the test results, which means that will add to the result a component that will change in a random fashion when repeating the measurement. Systematic error sources are all the sources that do not cause scatter in the results; they are constant along the duration of the experiment. Systematic errors are estimated either as the tolerances specified by the manufacturers or the result of the uncertainty calculation of the calibration of the instrument. In the case there is various sources of systematic error b_i, these can be combined as:

$$b_R = [\sum {b_i}^2]^{1/2}$$

Random errors are calculated as the standard deviation of the average of the measurements:

$$s_R = \frac{SEE}{\sqrt{N}}$$

Where SEE stands for Standard Error of the Estimate and it represents the standard deviation of the distribution and N represents the number of points considered.

Systematic and random sources are combined in order to calculate the absolute uncertainty:

$$U = \sqrt{b_i^2 + s_i^2}$$

The following uncertainty analysis lists each uncertainty in expanded form using a coverage factor k=2. The k value corresponds to a 2-sigma or 95% confidence interval.

1. Measurement noise→Measurement noise is the uncertainty caused by the noise or instability of the measurement readings. Each measurement point is based on the average or mean of 30 or more readings or samples. The uncertainty of the noise or instability of the 30 readings is calculated by dividing the standard deviation of the 30 samples by the square-root of n (n = 30). This calculation is often referred to as Standard Error of the Mean.
2. Check standard statistic→ The check standard statistic is an indication of the stability of the calibration process. The check standard measurement results have been plotted in a control chart and analysed to make sure no unexpected errors occur. The value entered into the uncertainty analysis is the standard deviation of the check standard measurements over time.
3. Readout accuracy calculation→ The following calculations demonstrate how to convert typical thermocouple specifications into values that can be entered into the uncertainty analysis. Since most thermocouples' readout are specified in terms of voltage accuracy, the following equation converts voltage uncertainty to temperature: $U = \frac{1}{2}(0.02\% * \bar{V} + 5{,}5\mu V) * \overline{m}$ (given in Ametek datasheet)
4. Reference junction accuracy→ The reference junction compensation is designed to compensates the changes in the ambient temperature. If the ambient temperature rises or falls, the compensation will automatically adjust for the change in reference junction potential, such that the output will still register the process (measurement junction) temperature.
5. Reference probe calibration uncertainty→ This uncertainty is transferred directly from the calibration certificate of the reference probe.
6. Axial and radial uniformity→ Furnace uniformity results to be more important than furnace stability in obtaining good quality calibrations.

To combine the uncertainties in order to calculate total uncertainty, it is important to know if each uncertainty is independent or correlated. An independent uncertainty is one that has nothing in common with the other uncertainties.

All independent uncertainties can be combined or added together using Root Sum Squares (RSS). A correlated uncertainty means that it has some type of correlation or relationship with one or more other uncertainties. Correlated uncertainties can often be added together with simple addition and then the sum is added by RSS with the other uncertainties.

		EXPANDED UNCERTAINTY [°C]			
Type standard uncertainty	*Calculation*	*TEST CHAMBER NO CASING*	*TEST CHAMBER WITH CASING*	*OIL BATH DRY MODE*	*OIL BATH LIQUID MODE*
Measurement noise/stability of reference	$U = \frac{\overline{RMS}}{\sqrt{n_{ref}}}$		±1,27 * 10^{-3}	±1,32 * 10^{-3}	±3,12 * 10^{-3}
Measurement noise/stability of thermocouples	$U = \frac{\overline{RMS}}{\sqrt{n_{tc}}}$	±3,18 * 10^{-3}	±8,49 * 10^{-4}	±4,31 * 10^{-4}	±2,81 *10^{-3}
Check standard statistic	$U = \overline{RMS}$	±0,1003	±0,027	±0,014	±0,045
Reference junction accuracy		±0,05	±0,05	±0,050	±0,050
Readout accuracy for reference			±0,012	±0,012	±0,012
Readout accuracy for thermocouples	$U = \frac{1}{2}(0.02\% * \bar{V} + 5{,}5\mu V) * \bar{m}$	±0,072	±0,071	±0,70	±0,069
Reference probe calibration uncertainty			±0,025	±0,025	±0,025
Test chamber T deviation in time		±0,3			
Test chamber calibration uncertainty		±0.175			
Axial uniformity				±0,04	±0,011
Radial uniformity		±0,63	±0,356	±0,008	±0,009
Total expanded uncertainty (k=2)	$U = \sum correlated\ uncertainty + \sqrt{\sum (indipendent\ uncertainty)^2}$	0,84	±0,41	±0,12	±0,150

Table: 3.7: Summary scheme of the terms considered in the uncertainty budget

3.2 Thin film casing insert calibration

3.2.1 Annealing

From the voltage traces, the original thin-film resistance values can be converted into temperature signal trough the calibration law.

Before the calibration, the annealing of the thin films is performed in order to assess any possible drift in thin films resistances. The annealing procedure consists in bringing the sensors to its maximum operating temperature monitoring the thin films resistances for several hours. Once the probe is cooled down, the value of resistance at ambient temperature is checked again to verify any presence of thermal hysteresis in the material. Thin films resistance values are acquired with the Fluke multimeter in Ω mode.

A total of nine annealing procedures are performed for the thin films casing insert. The first one with no current passing through the sensors, while the other ones with thin films turned on with the maximum feeding current of 20 mA to consider Joule effect. For the first one, performed at 65°C for 6 hours, the experimental setup is composed as shown in Figure 3.29.

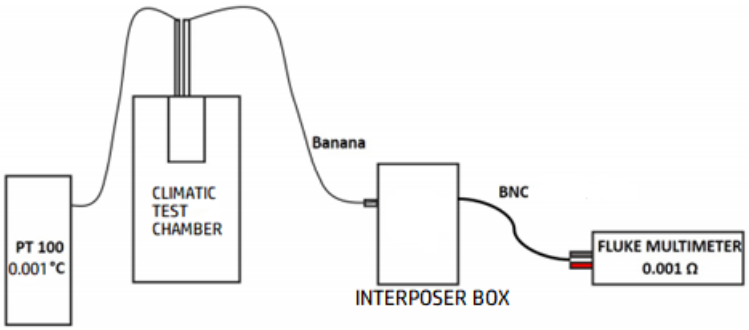

Figure 3.29: Setup for the annealing procedure

All the acquired data, which refer to the characteristic points of the insert (shown in Figure 3.30), are reported in Figure 3.31 and 3.32 that represent the T and R trend during the annealing while Figures 3.33 and 3.34 highlight the changing in the resistance values before and after the first annealing procedure.

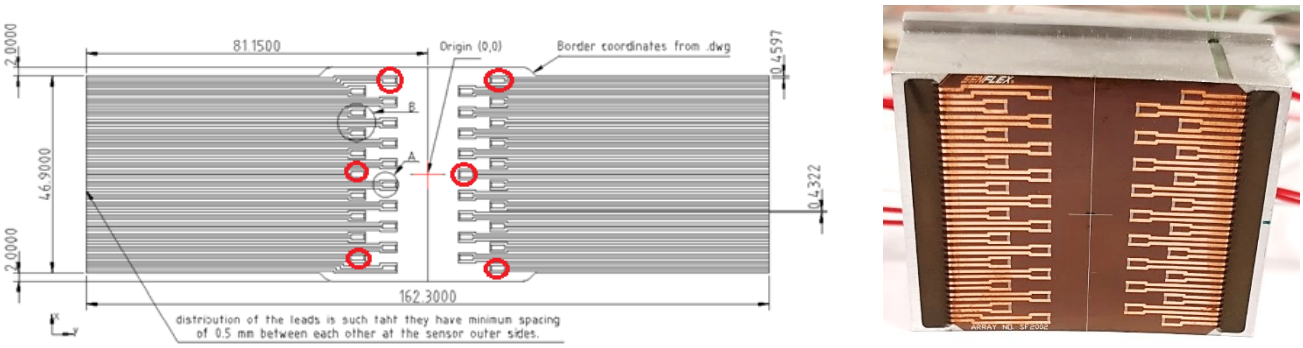

Figure 3.30: Drawing of thin film circuit

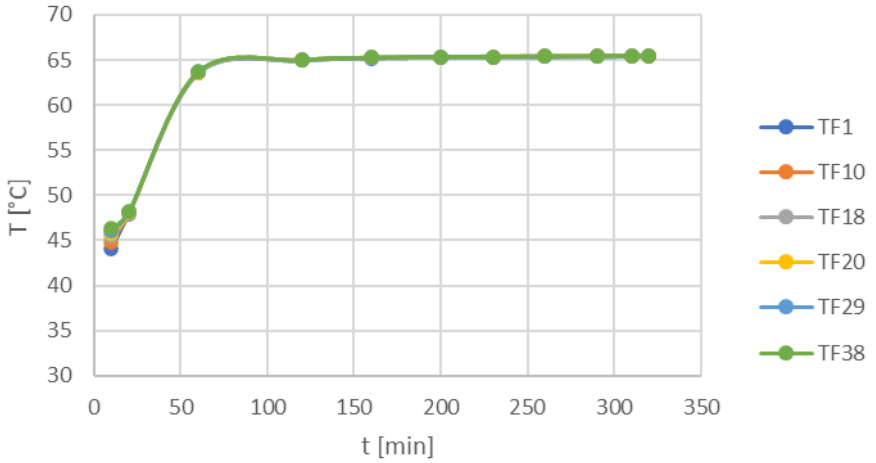

Figure 3.31: Temperature trend over time relative to the thin films taken as reference

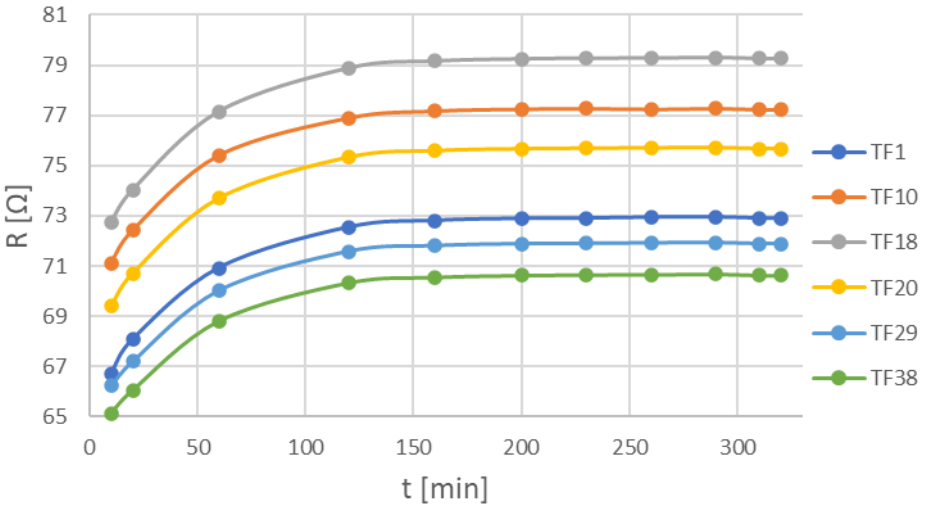

Figure 3.32: Resistance trend over time relative to the thin films taken as reference

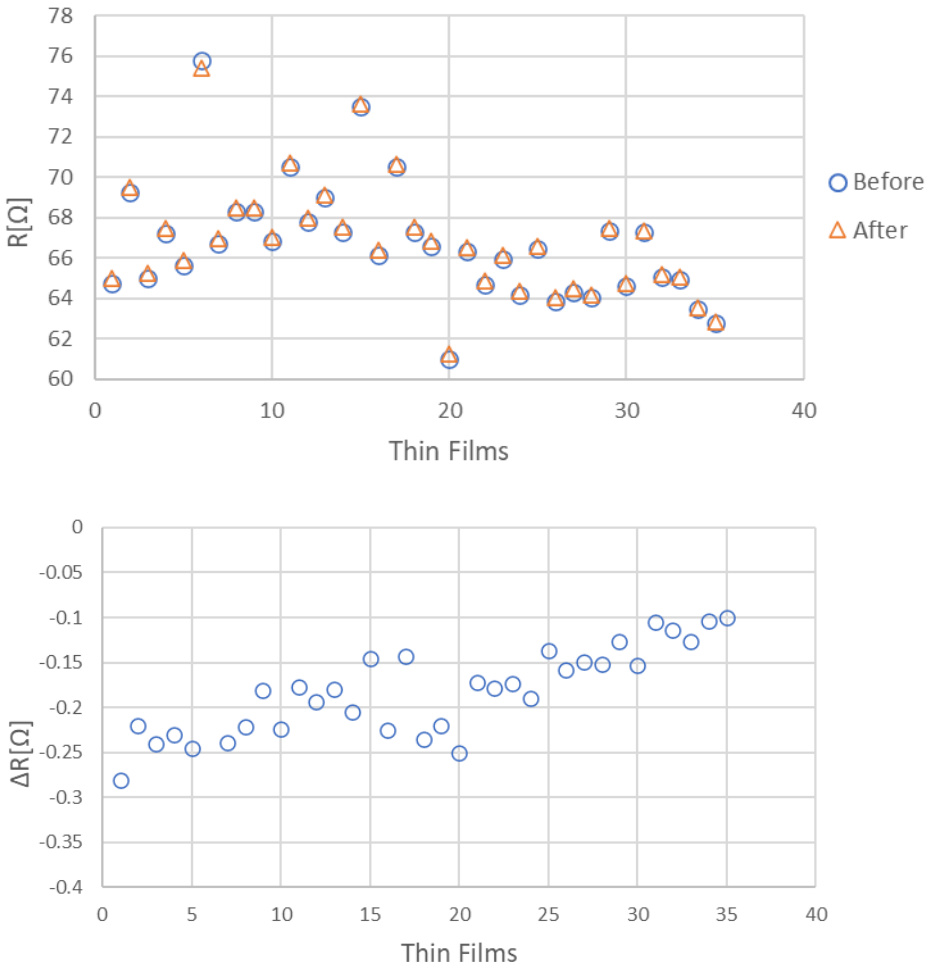

Figure 3.33: Resistance comparison before and after the annealing procedure

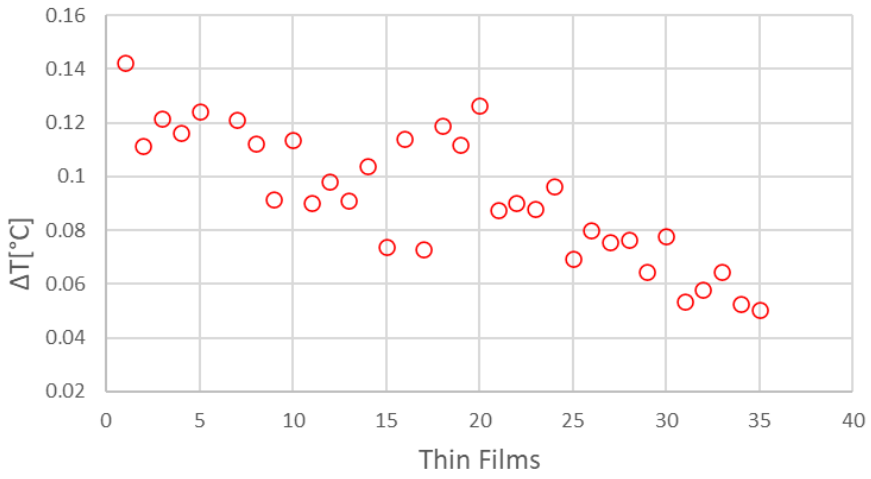

Figure 3.34: Comparison before and after the first annealing in terms of temperature

A schematic of the others anneals' setup is proposed in Figure 3.35. The latter is partially changed with respect to the previous cases in order to feed the thin films with the desired current. This need is satisfied including in the setup a control board, specifically designed for heat transfer measurements described in the following.

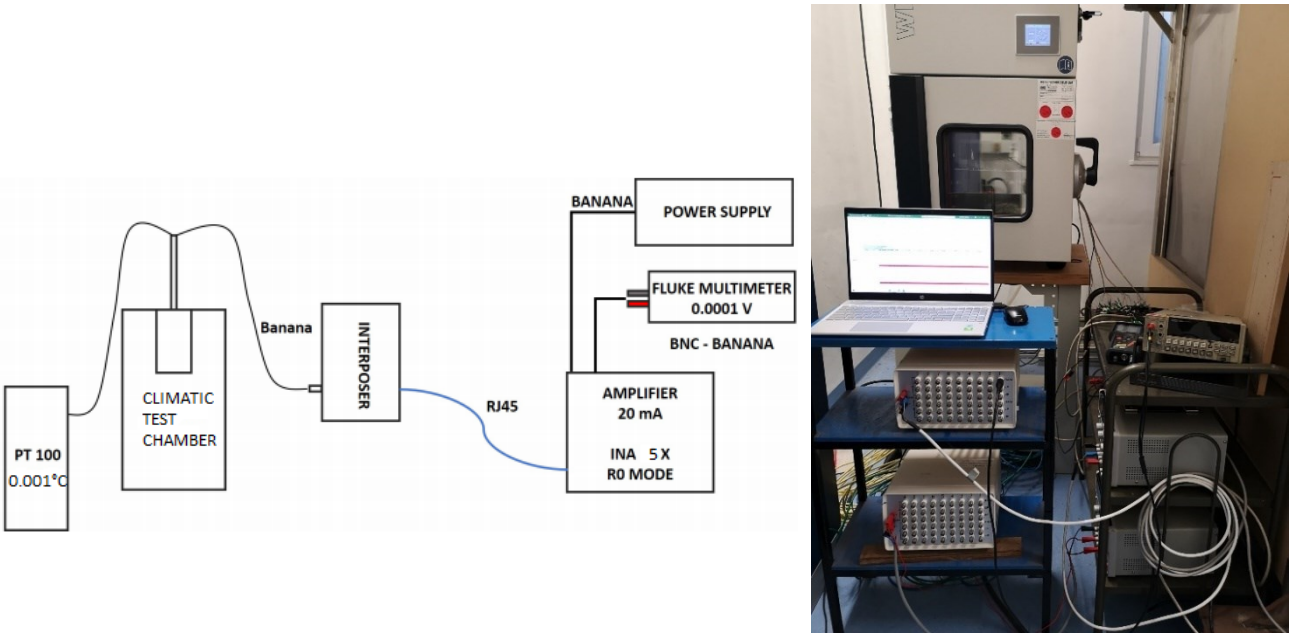

Figure 3.35: Setup scheme for the annealing procedure with thin films switched on

The control board is a signal conditioning unit composed by 9 boards with 2 channels per boards. It serves both as current supply for thin films as well as filter and amplifier. It accepts two different kinds of input: RJ45 connectors or BNC cables. When the resistance signal is given as input to the boards through the RJ45 connectors, it is converted into a voltage signal through an Anderson's Loop. This signal is then amplified with an Instrumentation Amplifier (INA) with a selectable gain that can be X1, X5 or X10. After that, an analogue switch controls whether the system is operated in R_0 mode or DR mode. When in R_0 mode, the voltage continues unaltered. When switching to the DR ('differential') mode, the circuit is balanced (set to 0 V) to record only the AC component of the signal that can be, depending on the switch 'EXT', amplified 10 times or not. Eventually, a shaped gain is applied. The latter is meant to counteract the diminishing amplitude of the temperature fluctuations resulting from heat flux variations at larger frequencies. The last part of the electronics is a filter stage, which can also be used separately through the BNC input.

Three outputs are generated: a RAW, unfiltered signal, a low-pass filtered signal at 500 Hz and a High-Pass filtered signal at 60Hz. To avoid aliasing, the latter includes a 180 kHz low pass filter as well. Three different current intensities can be selected, of 10, 15 or 20 mA. A schematic of the heat transfer amplifier functioning is reported in Figure 3.36, whereas a picture of the front and rear panel is reported in Figure 3.37. The settings adopted for this test are provided in Table 3.8.

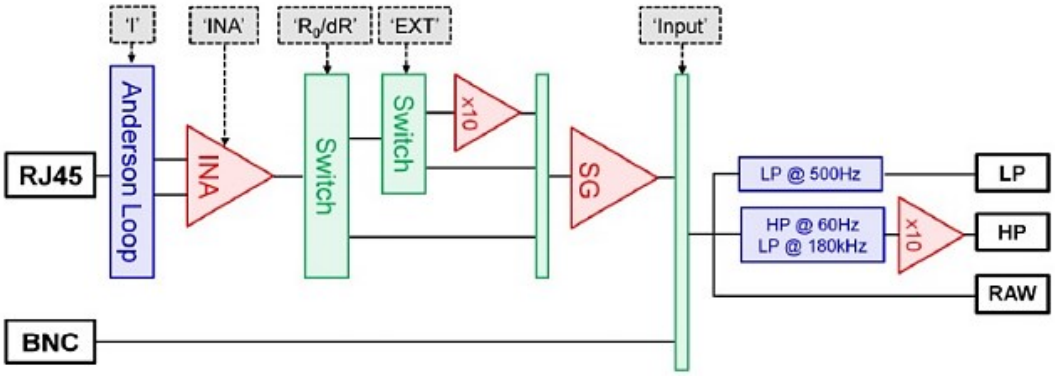

Figure 3.36: Simplified schematic of the electronics of the thin film conditioning unit

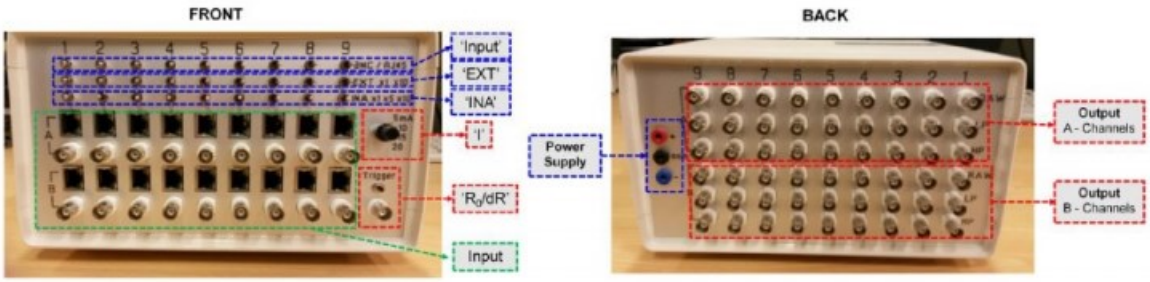

Figure 3.37: Picture of control unit's front and real panels

Current	20 mA
INA	X5
Output	RAW
Mode	R0
EXT	X1 (Off)

Table 3.8: Heat Transfer Control Board Settings

These types of annealing are performed at 70°C for an average time of 7 hours. The temperature inside the casing where the insert is located and the thin film voltages, are acquired every hour for the first 3 hours and every 30 minutes for the remaining time.

Every time, the first measurement is taken as reference at ambient temperature. After that, all measurements are taken with the oven turned on. The temperature and voltage trends during this procedure are shown in Figure 3.38 and Figure 3.39. After the ninth annealing and the complete cool down of the insert, the resistance at ambient temperature is checked again (Figures 3.36 and 3.37).

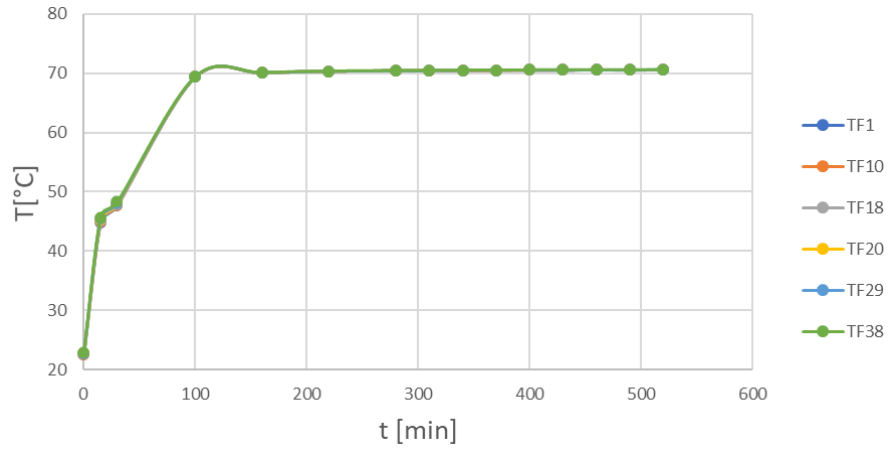

Figure 3.38: Temperature trend over time relative to the thin films taken as reference

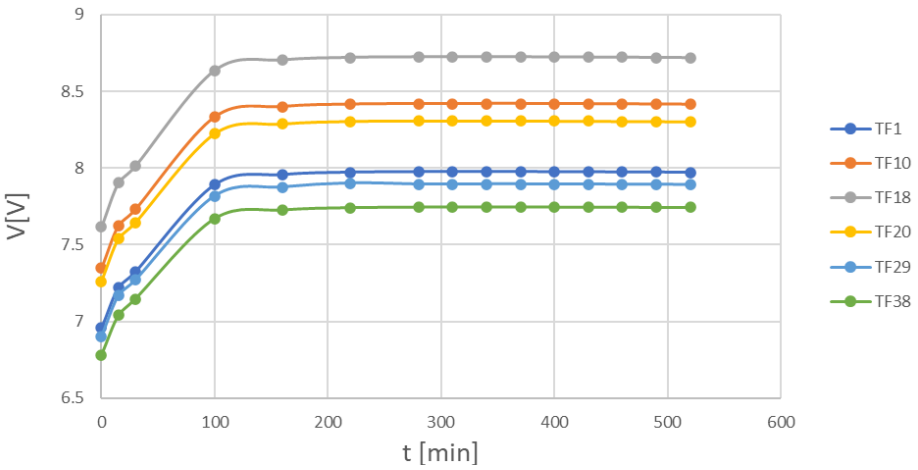

Figure 3.39: Voltage trend over time relative to the thin film taken as reference

Figures 3.40 shows the achievement of stability in terms of voltage. After 3 hours the difference between the voltage and the asymptotic value is 0,0062 V (0.08%) and this value tends asymptotically to zero over time. This is important to verify that the voltage does not increase with a constant temperature.

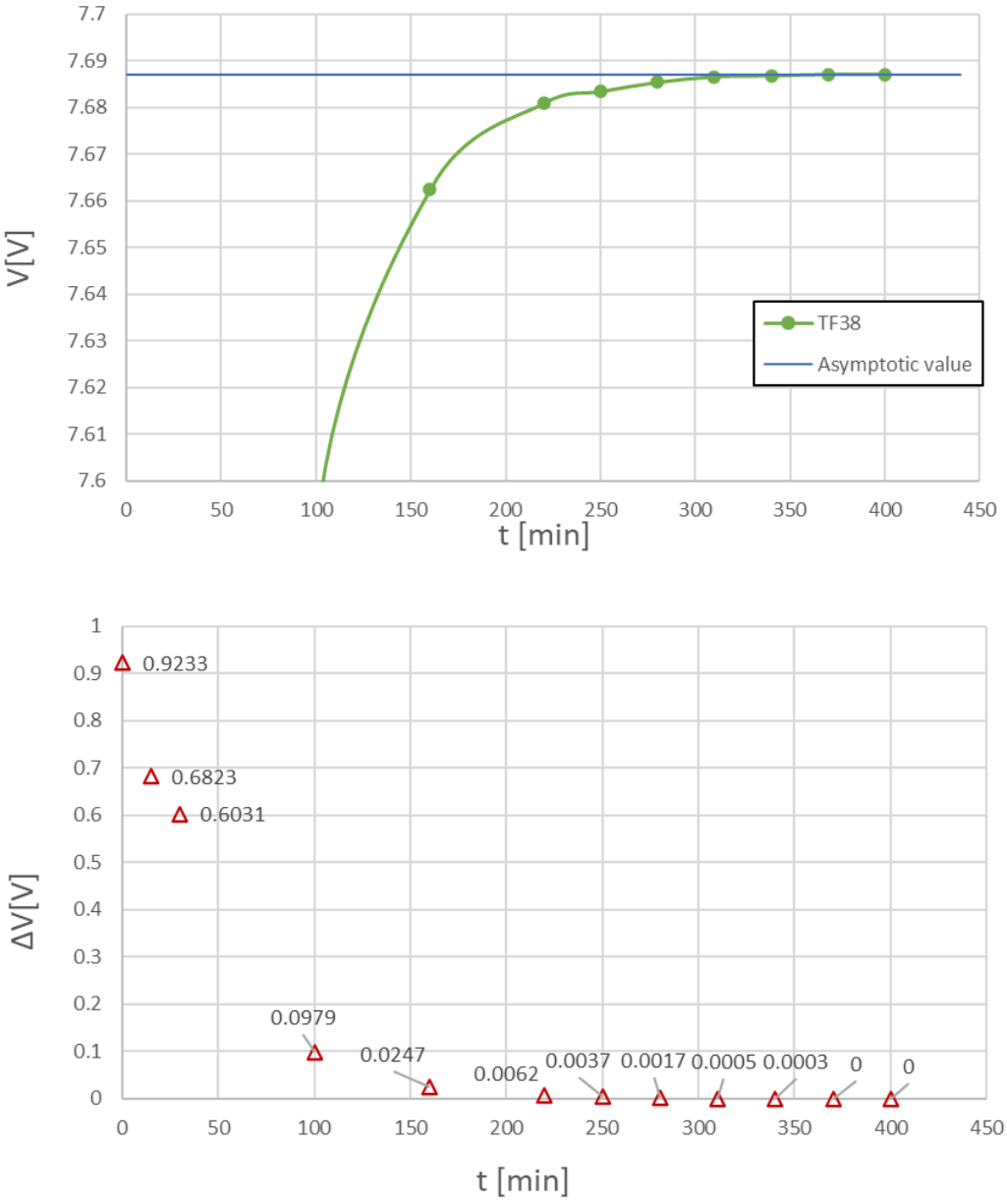

Figure 3.40: Voltage stability analysis over time

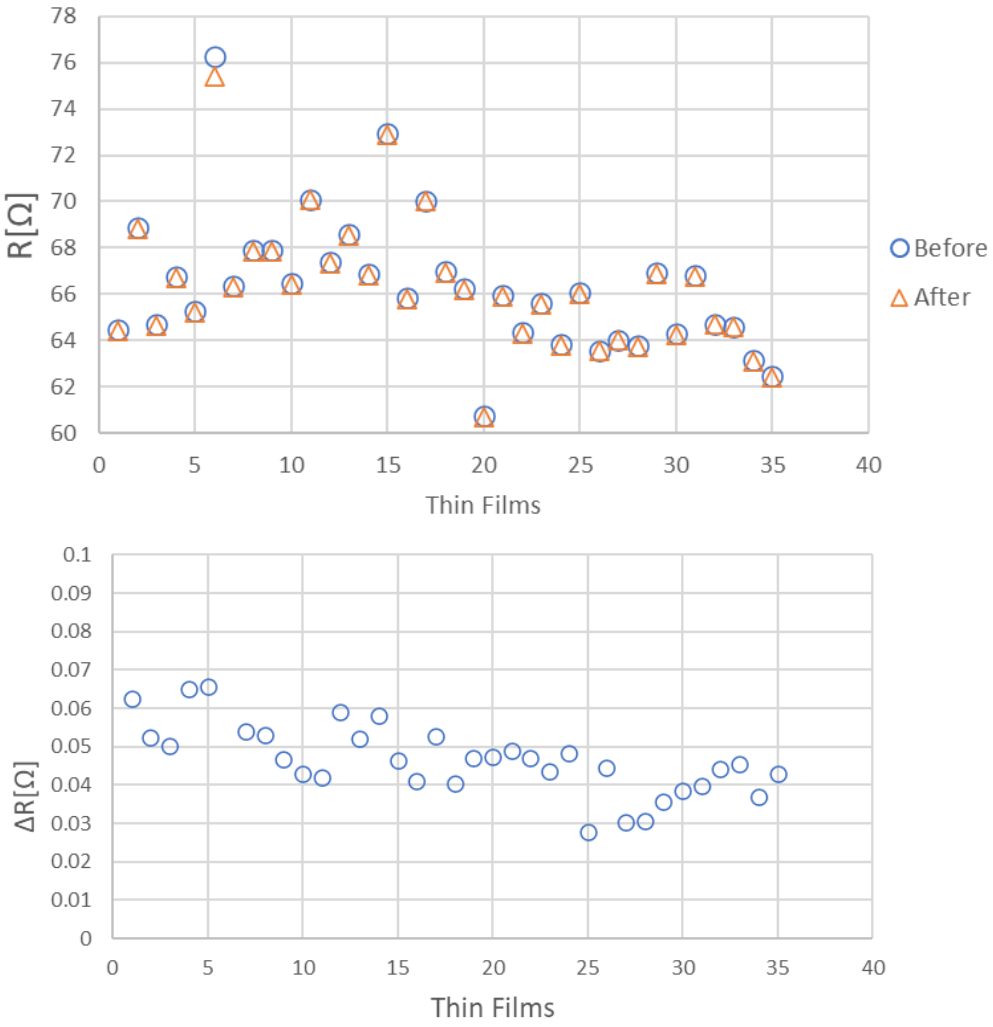

Figure 3.41: Resistance Comparison before and after the last annealing procedure

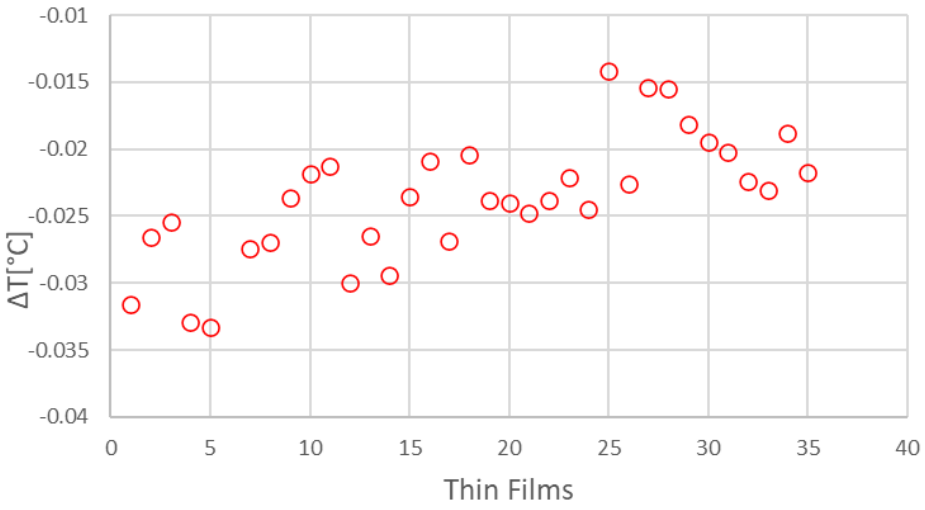

Figure 3.42: Comparison before and after the last annealing in terms of temperature

Figure 3.41a shows an anomaly in sensor 6 which has a resistance variation between before and after annealing greater than 0.8 Ohm. This variation could be explained by the presence of an air bubble between the metal surface and the sensor whose dimensions vary as the temperature to which the insert is subjected varies but this theory cannot be confirmed just through a visual inspection, so the results of this sensor were not taken into account.

It is important to note how to perform nine annealing, it allowed to pass from an average difference in resistance between before and after the procedure of 0.17 ohm (corresponding to 0.09 °C) to a difference of 0.04 ohm (corresponding to 0.02 °C).

Table 3.9 summarizes the operating conditions and the results obtained after each annealing, highlighting how it was necessary to repeat the procedure 9 times before ensuring that there are no substantial changes in terms of resistance between before and after heating the insert.

After all the annealing it was possible to calculate the sensitivity of each thin film as expressed in the following expression:

$$Sensitivity = \left(\frac{V_{75°C} - V_{25°C}}{T_{75°C} - T_{25°C}}\right)\frac{1}{0.02}\frac{1}{5}$$

Dividing the first factor by I=0.02 A and by INA=5 it was possible to convert the unit of measure from V/°C to Ω/°C. Sensitivity is a parameter that allows to transform the variation in perceived resistance into a ΔT, which must not exceed 0.3 ° C in order to state that temperature cycles do not involve variations in terms of resistance.

N annealing	***Operating conditions***	$\overline{\Delta R}$ ***[Ω]***	***Sensitivity [Ω/°C]***	$\overline{\Delta T}$ ***[°C]***
1) 18/11/2020	6h	-0.18	0.219	-0.82
2) 20/11/2020	20mA, 9h10’	0.11	0.219	0.50
3) 23/11/2020	20mA, 7h	0.16	0.227	0.71
4) 24/11/2020	20mA, 7h	0.06	0.218	0.28
5) 25/11/2020	20mA, 7h30’	0.082	0.213	0.39
6) 26/11/2020	20mA, 7h	0.046	0.208	0.22
7) 27/11/2020	20mA, 7h	-0.025	0.216	-0.12
8) 30/11/2020	20mA, 7h40’	0.104	0.215	0.48
9) 01/12/2020	20mA, 7h	0.047	0.208	0.22

Table: 3.9: summary table of the changes in resistance and temperature undergone by the sensors following the annealing procedure

The unexpected values detected in the eighth annealing are due to the incorrect positioning of the insert and the PT100 inside the test chamber. In fact, being in contact with the casing wall, the perceived temperature turns out to be much higher and continuously increasing compared to the actual temperature perceived by the insert.

Considering the achievement of voltage stability; obtaining the same sensitivity, resistance and therefore temperature values between before and after the sixth and ninth annealing process; and the absence of significant changes in resistance, the robustness of the electrical connections and in general the stability of the complete assembly is assessed.

3.2.2 Resistance - temperature calibration

The variation of thin film sensors electrical resistance with temperature is calibrated for each gauge using a temperature controlled industrial climatic chamber into which the instrumented block is placed. In particular, the insert has been positioned inside a metal box which prevents the flow of air generated by the oven fan impacts directly with the sensors and allows a higher stabilization and homogenization of the temperature as shown in Figure 3.43.

Figure3.43: Thin film insert positioning inside the test chamber.

The experimental setup, composed by a climatic test chamber SYSTEM WEISS TYPE WKL, a PT100, an interposer banana-BNC, a Fluke multimiter in mode Ω that allow to measure the resistance value of the thin film gauges is shown in Figure 3.44.

Figure 3.44: Setup for test chamber calibration

The calibration technique involves measuring gauge resistance as a function of temperature over a cycle of increasing temperatures. A PT100 thermometer is used as reference to monitor the temperature in proximity of the thin film casing insert. When several points at different temperature in a range between 25°C and 70°C have been taken, plotted, and appear consistent, the results are fit to the functional form of the sensor. Since the sensors are expected to be linear, a least squares linear fit is done on the actual temperature and the sensors output. The least squares fitting removes some of the random statistical error associated with a single calibration point and gives a smoothed, consistent summary of the calibration results. A linear regression between resistance and temperature is accomplished to obtain the calibration law shown in Figure 3.45 and Table 3.10.

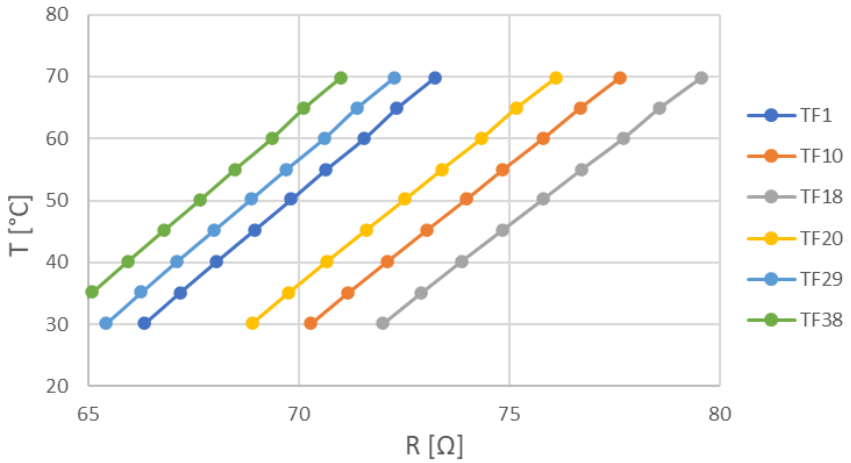

Figure 3.45: Calibration law

	$\overline{m}$ [°C/Ω]	$\overline{q}$ [°C]	$\overline{R^2}$
Calibration	5,545	-347,202	0,99992

Table 3.10: Linear regression coefficients

R^2 values above 0,9999 are acceptable, thus all the calibrations are satisfactory.

The residual plot (Figure 3.46), in which residuals are on the vertical axis and the independent variable is on the horizontal axis illustrate that the dots are randomly dispersed around the horizontal axis then a linear regression model is appropriate for the data.

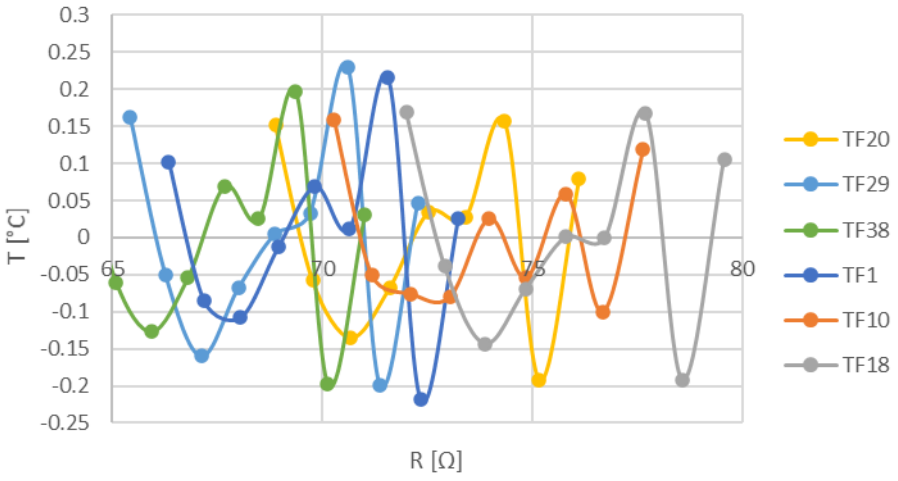

Figure 3.46: Residual plot for reference thin film

To further demonstrate the stability achieved by the sensors, the full calibration was performed twice. The results of the comparison of the calibration procedures are analysed and discussed in the following paragraphs.

To analyse the repeatability of the process and the stability reached by the gauges it is possible to compare the calibrations and evaluate if any shift in terms of slope and intercept are present.

Each calibration was performed in different days. Each time, the acquisition was made after reaching a stable temperature inside the casing and a stable resistance. After each acquisition day the insert was cooled down until reaching the ambient temperature, in this way complete thermal cycles were performed.

Figure 3.47 and Table 3.11 summarize the results achieved with the calibrations.

Calibration parameters	*1° Calibration*	*2° Calibration*	**Δ [%]**
$\bar{m}$ [°C/Ω]	5,55	5,47	-1,3
$\bar{q}$ [°C]	-347,20	-342,12	-1,5
$\overline{R^2}$	0,99992	0,99984	-0,008

Table 3.11: Average variation calibration parameters.

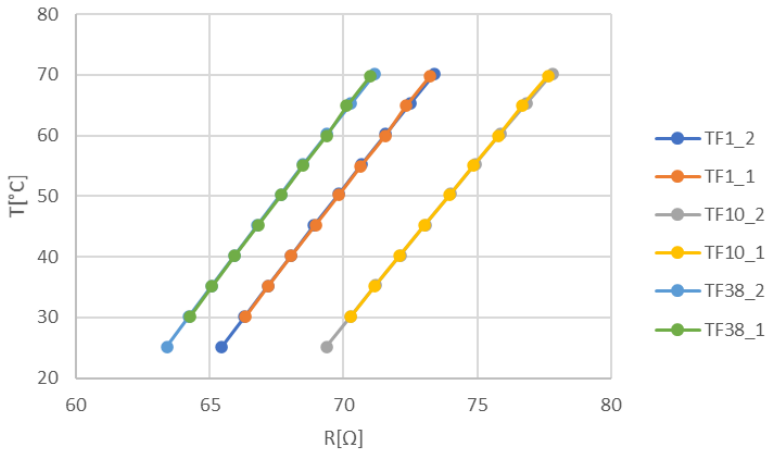

2Figure 3.47: Calibration law

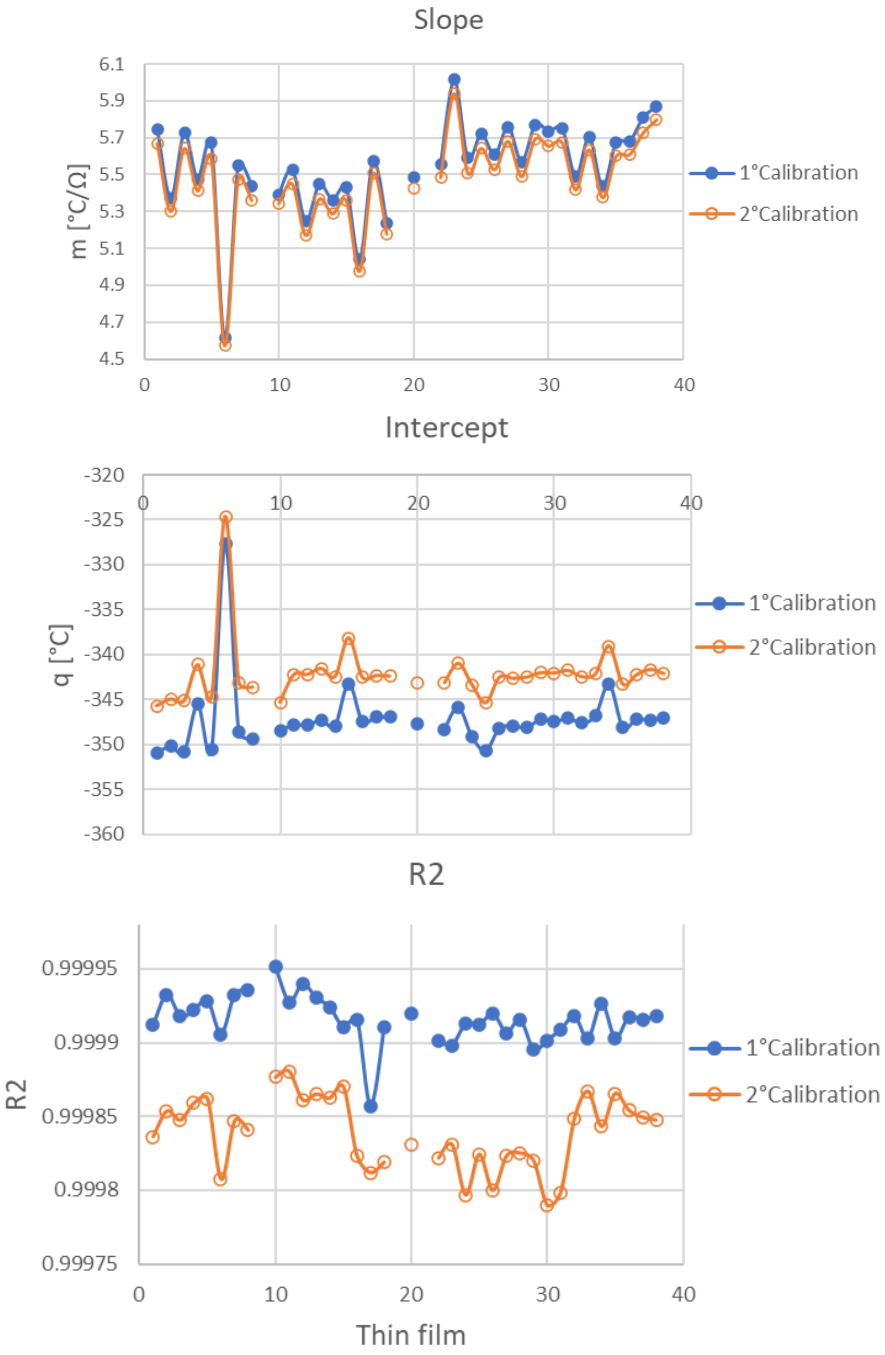

Figure 3.48: Comparison linear regression coefficients

By comparing the calibration parameters of Figure 3.48 it is possible to evaluate how the latter are subject to average variations summarized in Table 3.11. The differences between the calibration parameters, which can be identified by comparing the two calibration processes, are due to a misalignment between the first five points and the last five relating to the second calibration. In fact, by analysing the two sections of the latter (Figure 3.49) it is evident that while the variation in terms of slope is negligible, there is a displacement as regards the intercept which reduces the global value of R^2.

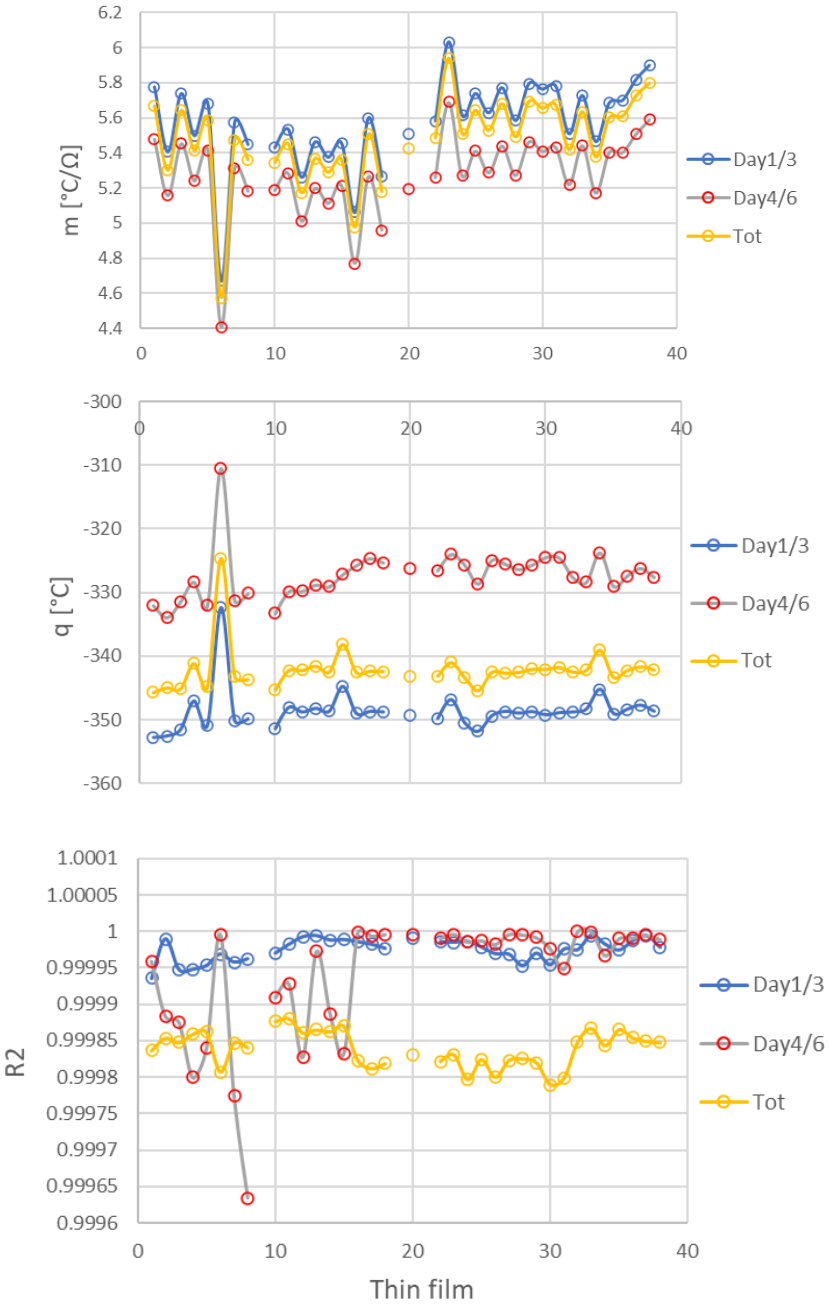

Figure 3.49: Comparison linear regression coefficients of the second calibration

Calibration parameters	*1° Calibration*	*2° Calibration First 5 points*	**Δ [%]**
$\overline{m}$ [°C/Ω]	5,545	5,567	0,39
$\overline{q}$ [°C]	-347,202	-348,613	-0,4
$\overline{R^2}$	0,99992	0,99998	0,006

Table 3.12: Average variation calibration parameters.

The confirmation of the above can be obtained from the comparison between the first calibration and the single sections relating to the second, which highlights how the variation of the parameters is negligible as shown in Table 3.12.

After each calibration, the resistance at ambient temperature was checked again obtaining the results shown in Figure 3.50 and summarized in Table 3.13.

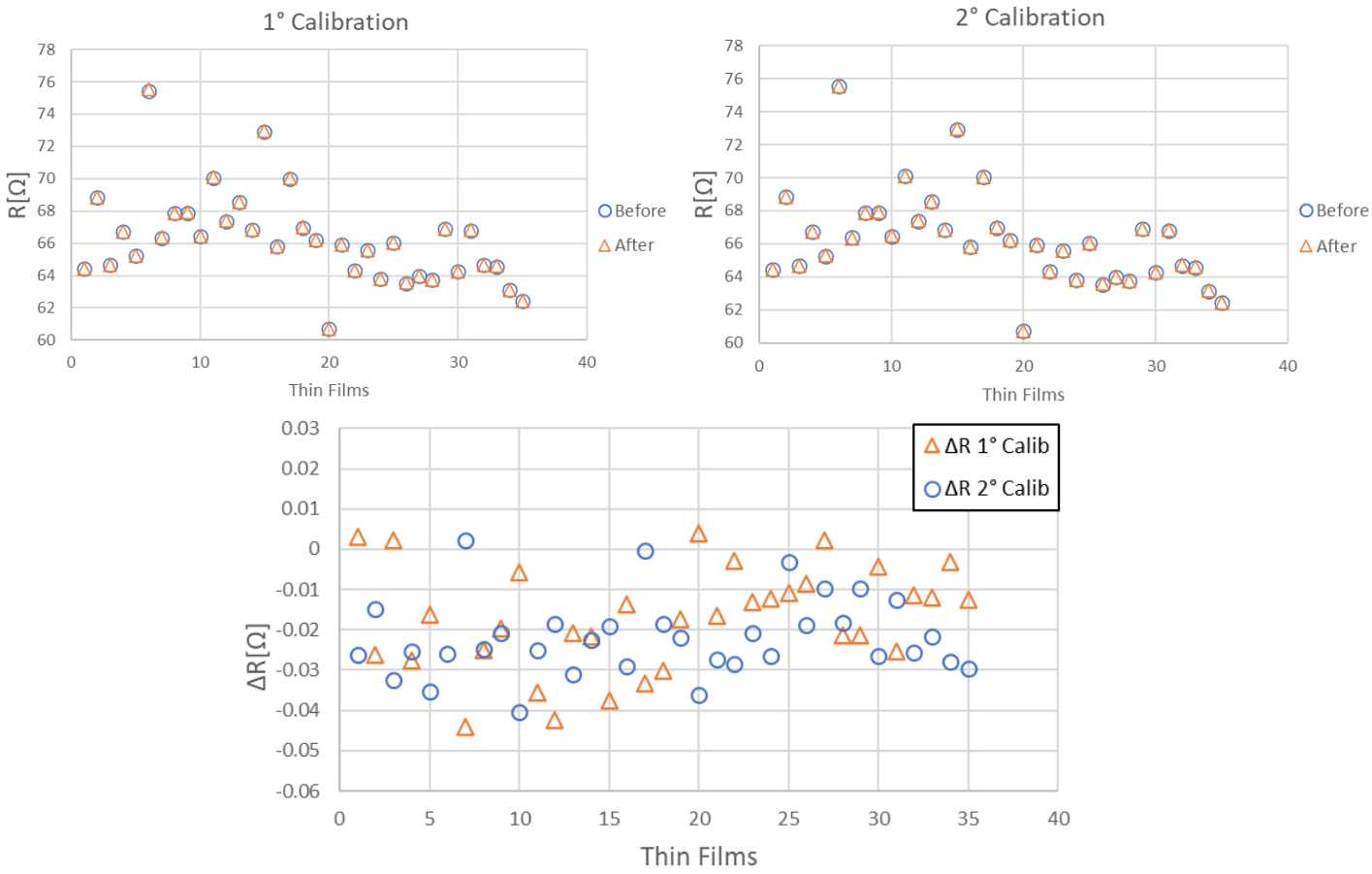

Figure 3.50: Comparison resistance before and after calibration process

Calibration	$\overline{\Delta R}$ *before VS after* $[\Omega]$	$\overline{\Delta T}$ *before VS after* $[°C]$
1	-0,017	-0,08
2	-0,022	-0,11

Table 3.13: Check possible drift in thin films resistances after each calibration.

Analysing the results shown above, no resistance shift was detected, and this leads to obtaining a temperature variation which falls within the uncertainty range of the instrument.

3.2.3 Uncertainty analysis thin films calibration

The uncertainty analysis is a fundamental tool to select the measurement chain and data processing tool. A complete uncertainty estimation is presented in this section. There are several calibration uncertainties to be evaluated in determining the total uncertainty of a thermocouple calibration system. As suggested by Favier [14], two macro uncertainty sources can be identified for experimental data: the measurement related uncertainty and the uncertainty associated with the statistical data reduction. The first item refers to all bias and random errors that result from the application of a particular instrument and measurement methodology (e.g., sensor, calibration, installation, flow conditions, data reduction, etc.). The second uncertainty contribution refers to the significance of the finite sample size when computing averaged quantities (i.e., the sampling duration). All the uncertainty sources that have been considered for the static calibration (detailed in 3.1.1) are summarized in table 3.14.

Type standard uncertainty	***CALCULATION***	***TEST CHAMBER WITH CASING***
Measurement noise/stability of reference	$U = \frac{\overline{RMS}}{\sqrt{n_{ref}}}$	±3,14 * 10^{-4}
Check standard statistic	$U = \overline{RMS}$	±0,011
Readout accuracy for reference	Isotech TTI-10 manual	±0,012
Reference probe calibration uncertainty	Isotech TTI-10 manual	±0,025
Test chamber T deviation in time	Climatic chamber datasheet	±0,3
Fluke multimiter accuracy	± 2*[0.013 % ($\overline{R_{70°C}}$ + 3)] * $\overline{m}$	±0,113
Total expanded uncertainty (k=2)	$\sqrt{\sum (indipendent\ uncertainty)^2}$	±0,32

Table 3.14: Summary scheme of the terms taken into account in the uncertainty analysis.

3.3 Thin film instrumented vane calibration

The R-T calibration of the thin films positioned on the vane was performed during a previous test campaign as the one described for the thin film casing insert, but just one annealing procedure was done for 8 hours reaching a temperature of 70,6°C to assess any possible drift in thin films resistances. The setup composed by the climatic chamber, the interposer, the Fluke multimeter, PT100 as reference resistance thermometer is shown in Figure 3.51. The calibration coefficients used for the processing data in this report are reported in Table A3 presents in Appendix A.

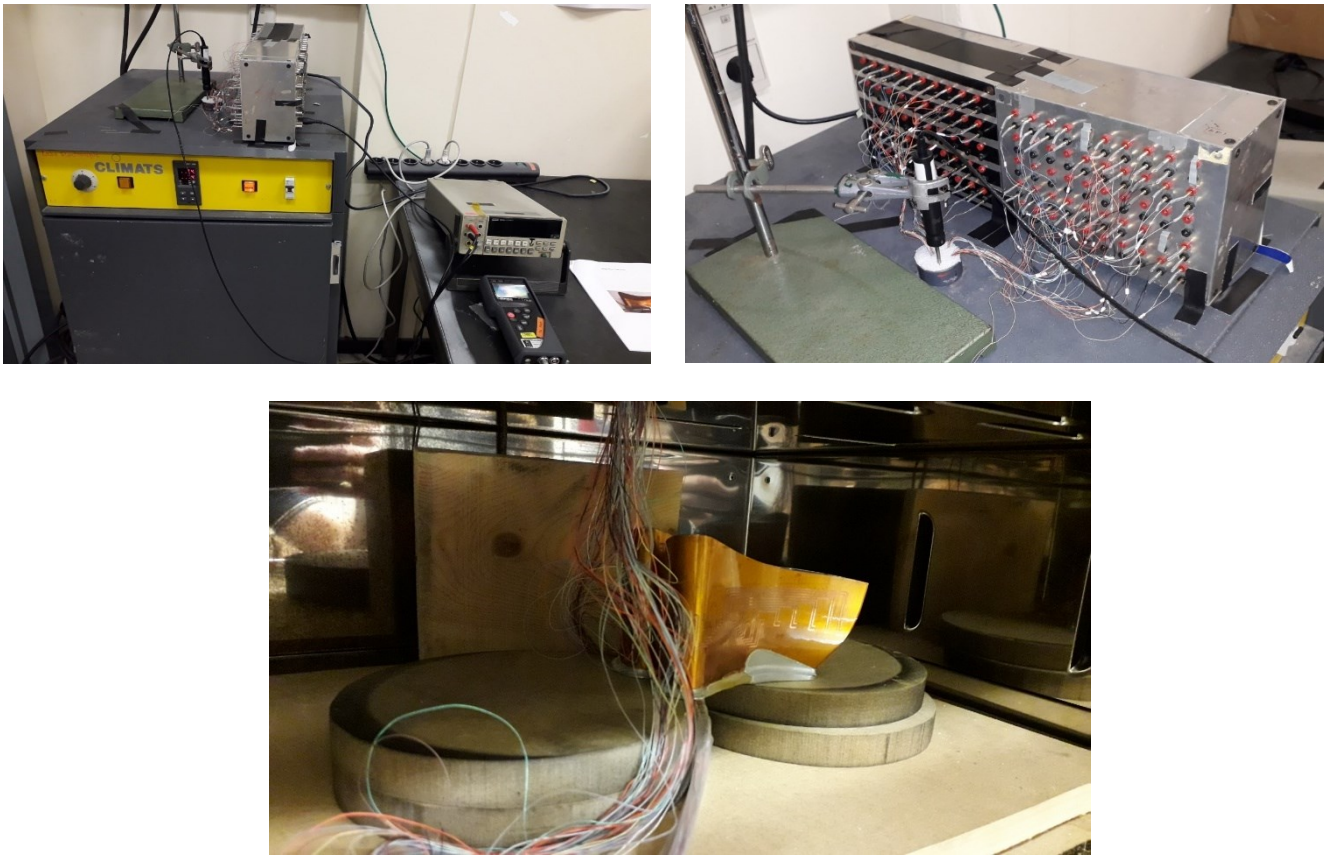

Figure 3.51: Calibration setup

Chapter 4

Experimental campaign

The goal of this experimental investigation is to analyse the steady and unsteady heat transfer and the aerodynamic conditions around the vane profile of a transonic turbine stage composed of 34 vanes and 48 rotor blades. The analysis of the convective heat exchange coefficient and the parameters obtained from the experimental campaign presented in the following allow to analyse the interaction between stator and rotor, if and where the flow transition appears along the vane, verify the efficiency of the cooling scheme, analyse the effects of the secondary flows and the losses, quantify the performance of innovative strategies and of the use of optimized blade tips geometries.

4.1 Instrumented stator vanes

Regarding the stator vane, this experimental investigation reports the heat transfer around the vane of a transonic turbine stage. Both time-resolved and time-averaged aspects are addressed. Unsteady heat transfer measurements allow to see the fluctuations generated by the rotor passing in front of the stator. The importance of conducting unsteady and therefore high-frequency heat flux measurements lies in the need to evaluate the interaction between stator and rotor. Therefore, these measurements, made both at the suction side and at the pressure side, allow for example to analyse the transition from laminar to turbulent flow, any presence of separations, etc.

The design of the thin films used for these measurements is more complex due to the high complexity in the air foil surfaces. The measurements are performed at 50% and 90% of the vane span. At each height, 26 thin film gages are distributed along the blade profile as can be seen in Figure B1 and Figure B2 while Tables B3 presents the summary of the tests carried out during the project and their conditions.

4.1.1 Heat transfer data conditioning

The thin films are controlled by newly custom-built amplifiers described in the previous paragraphs. The conditioning units can monitor the direct or the differential component of the gauge resistance and boost the sensor voltage by a DC gain variable between 1 and 75. This is a crucial aspect because in the frequency domain, thin-film gauge signals have a response T(ω)/q(ω) which decreases with rising frequency. Since the voltage change measured across the thin-film gauge at constant current is proportional to T, this signal is very small at high frequencies, and can be corrupted by electrical noise. This effect is qualitatively shown in Figure 4.52.

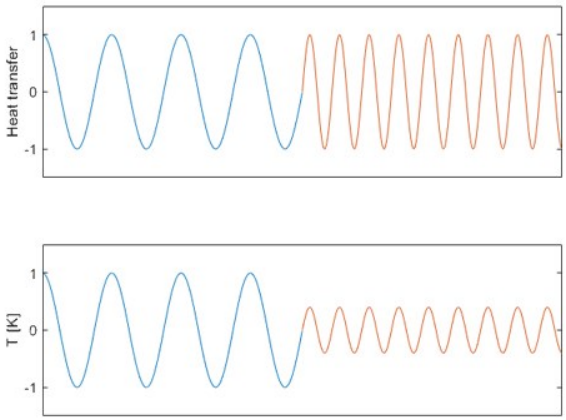

3Figure 4.52: Qualitative trend of the temperature amplitude decreasing with heat flux frequency.

As well as using low noise amplifiers and constant current supplies thin-film voltage signals are passed through an analog filter which pre-amplifies (otherwise known as “boosting” or “pre-emphasis”) the higher frequency signals to counter digitization errors in the smaller high-frequency signals and to reduce the effects of electrical noise after the initial amplifier.

The sensor signal is, hence, modulated by an analog filter stage with a gain profile increasing with frequency as shown in Figure 4.53. The frequency-dependent amplification varies from a factor of 2.3 at 100 Hz up to a peak gain of 75 at 150 kHz (about +12 dB/decade) after which the curve decays to avoid amplification of any noise.

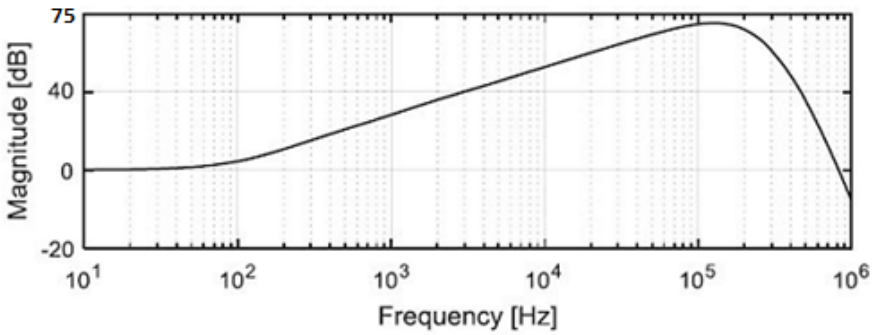

Figure 4.53: Shaped gain

During the blowdown, the signal from the gauges carries two types of information at different time scale:

- At the blowdown time scale, a large variation of temperature is recorded, similar to a step function with a total duration of about 0.2 seconds. This will be referred to as steady state component in the following.
- At the blade passing frequency, about 4700 Hz, very small fluctuations of temperature are measured corresponding to the stator-rotor interactions. This will be referred to as unsteady component.

Hence, the voltage being acquired with an acquisition system characterized by a high bandwidth, is filtered through an analog filter, before the digitization, in order to split it in two components as indicated in Figure 4.54. This is done, prior to sampling, to maximize the digital resolution of fluctuations at the blowdown duration time scale (0.2 s) and blade passing frequency (~ 2 μs). Indeed, dividing the original signal into the two high and low frequency components before the analog-to-digital conversion that allows to convert an analog signal with a continuous trend into a series of discrete values conversion, allows to divide the two different voltage ranges obtained into 65536 quantization levels, using 16-bit acquisition systems.

This guarantees the optimization of the resolution both for the trend of the filtered low-pass signal and for the fluctuations of the signal at high frequencies that otherwise would have different and not comparable range scales at the time of digitization.

To obtain LP components the time-average signal is low-pass filtered at 500 Hz and then sampled at 10 kHz for 10 seconds on a 16-bit resolution data acquisition system (National Instrument) while the high-bandwidth signal is conditioned through an analog band-pass filter allowing the information transfer in the range between 60 Hz and 250 kHz. The AC component is further amplified by a factor of 10 before being sampled on a 16-bit data acquisition system (Genesis) at 1 MHz as shown in Figure 4.54.

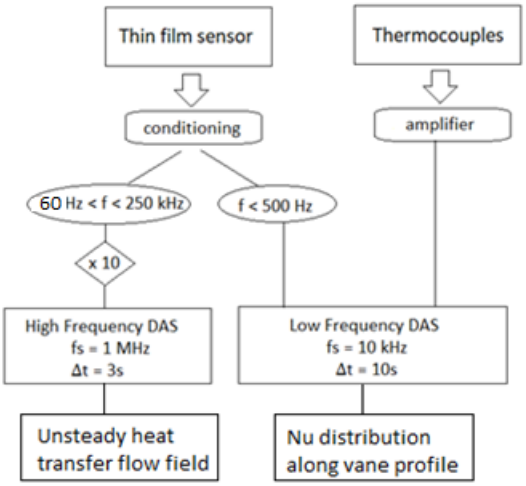

Figure 4.54: High- and low-frequency data conditioning and acquisition

4.1.2 Heat transfer data processing

Up to now, the shaped gain and two filtering stages have already been applied: analog (inside the amplifiers) and digital (inside the acquisition systems). Therefore, the output voltage signal is a signal that has undergone a modulation by means of these filters. The convolution of each transfer function used allows to obtain a global transfer function that groups them all. This transfer function varies according to the parameters set in the filters (amplification, type of filter, type of input cables, etc). Before applying the static calibration to retrieve from the voltage the temperature history, is necessary to correct this pre-emphasized or boosted signal and back to the thin-film voltage signal.

The MATLAB signal processing toolbox has been used to develop multiple IIR digital filters which have the inverse frequency response of the preamplifiers, and these filters can be used to recover the measured voltage from the recorded signals.

So, the TF^{-1} (demodulation transfer function) is applied to regain what was physically the true temperature variation and therefore the true voltage trend. In other words, before applying the static calibration as specified previously, through routine implemented on Matlab, it is possible to divide the signal obtained by the total transfer function, which is equivalent to applying it to minus 1, in order to find the initial signal only after having performed a correct digitization that allowed the filtering the signal in the desired bandwidth with a high resolution of temperature fluctuations even at high frequencies. The gauge voltage is, after the demodulation, converted into a resistance signal through an Anderson loop circuit that offers large-amplitude linear outputs for relatively low values of the excitation current. The latter is equal to 15 mA which represents a compromise between a higher current that would allow maximizing the ΔR at the output as the temperature variation, and so as the resistance variation, varies and a lower current that would allow minimizing the Joule effect that distorts the measurement. The calibration uses a slope and an intercept to convert the demodulated voltage into a resistance signal. These two coefficients are different for each amplifier. Due to the fact that the amplifier 1 calibration was not performed, it was necessary to evaluate the impact on the final value by applying an average of the calibration parameters rather than the exact values. By applying the maximum slope and then the minimum to the same signal, it is possible to evaluate the maximum percentage error that can be incurred by not calibrating the amplifier. Since the latter is a maximum of 0.165%, as shown in Figure 4.55, the calibration has not been performed.

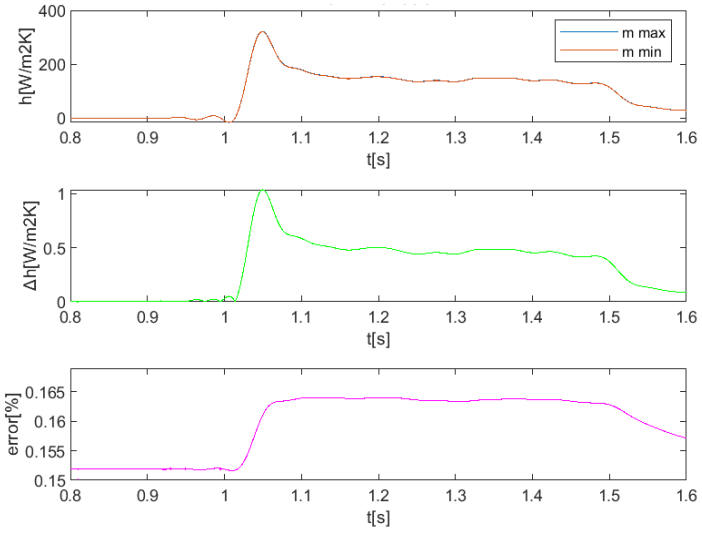

Figure 4.55: maximum h variation

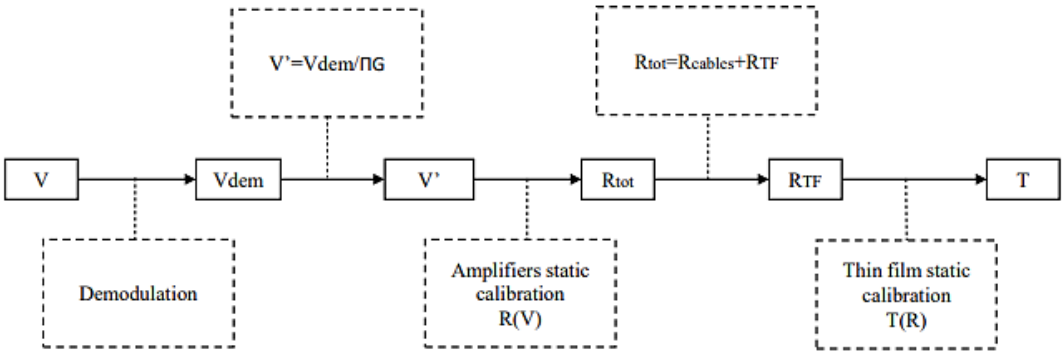

Figure 4.56: Voltage to temperature signal processing steps

With this data reduction technique, the entire frequency domain is covered in order to process both steady-state and fluctuating component.

At this point, while the heat flux at the casing is derived from the unsteady wall temperature measurements using a Crank-Nicholson scheme to solve the 1D unsteady heat conduction equation for a two-layer substrate with the assumption of a semi-infinite boundary condition at the back wall; for processing transient thin-film heat transfer gauge signals on the stator vanes it is necessary a new computationally efficient method developed by Oldfield [10].

The latter uses known pairs of exact solutions to derive an approximation of the impulse response of the gauge system. This impulse response is then used as a finite impulse response digital filter to process the sampled T signal to derive the required sampled $\dot{q}$ signal. This is computationally efficient because the impulse response need only be derived once for each gauge for a given sample rate, but can be reused repeatedly, using optimized MATLAB filter routines and is highly accurate.

4.1.3 Steady data processing

Once the signals are conditioned and acquired, several steps will lead us to the final Nusselt number, illustrated in figure 4.57.

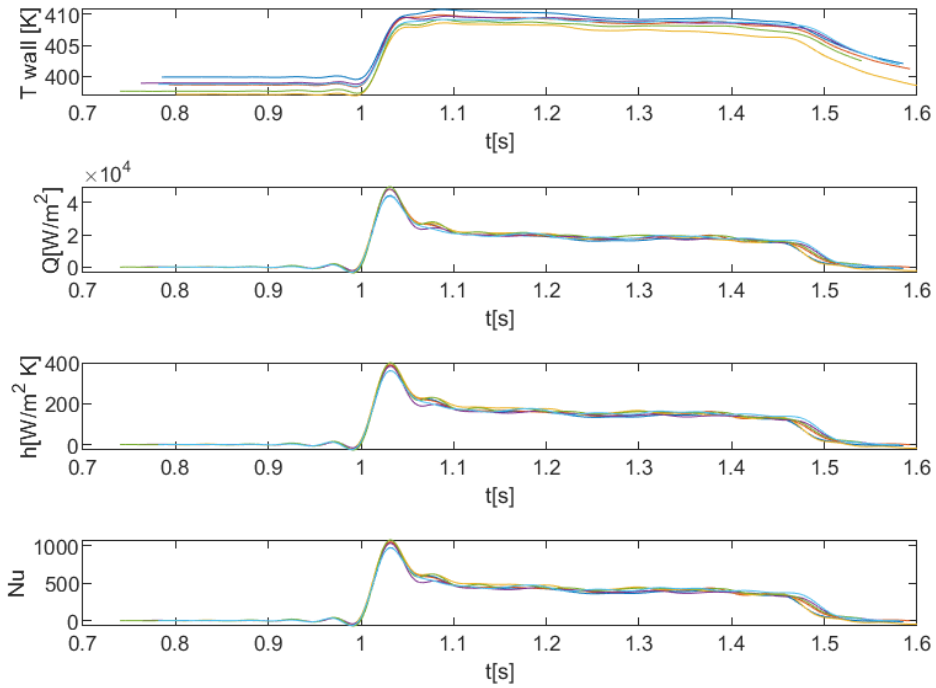

Figure 4.57: Processing steps

The first considerations can be made by analysing the trend of the raw voltage signal. In the figure 4.58 it is possible to highlight how the voltage increase depends on the position of the sensors along the pressure side and the suction side. The sensor positioned on the leading edge is the one that undergoes the most important increase consistently with the fact that it is the sensor hit almost perpendicularly by the flow. The other sensors, on the other hand, are characterized by a peak and a slope whose values tend to decrease as you move towards the trailing edge. Along the SS instead, the behaviour remains the same as just described, for the sensors adjacent to the LE, from a certain point onwards (both temporal and spatial) it is evident how instead the flow changes from laminar to turbulent. This causes the increase of the heat transfer evident from the sudden increase of the slope of the curve relative to the last sensor and to the reaching of the same of much higher peak values compared to the previous sensors, even higher than that recorded in the sensors adjacent to the LE.

In the highlighted area the hierarchy present at the PS is still in force therefore the curves are lower moving from the LE to the TE because the transition from laminar to turbulent requires both a certain time as well as unfavourable aerodynamic conditions that occur in the terminal part of the suction side.

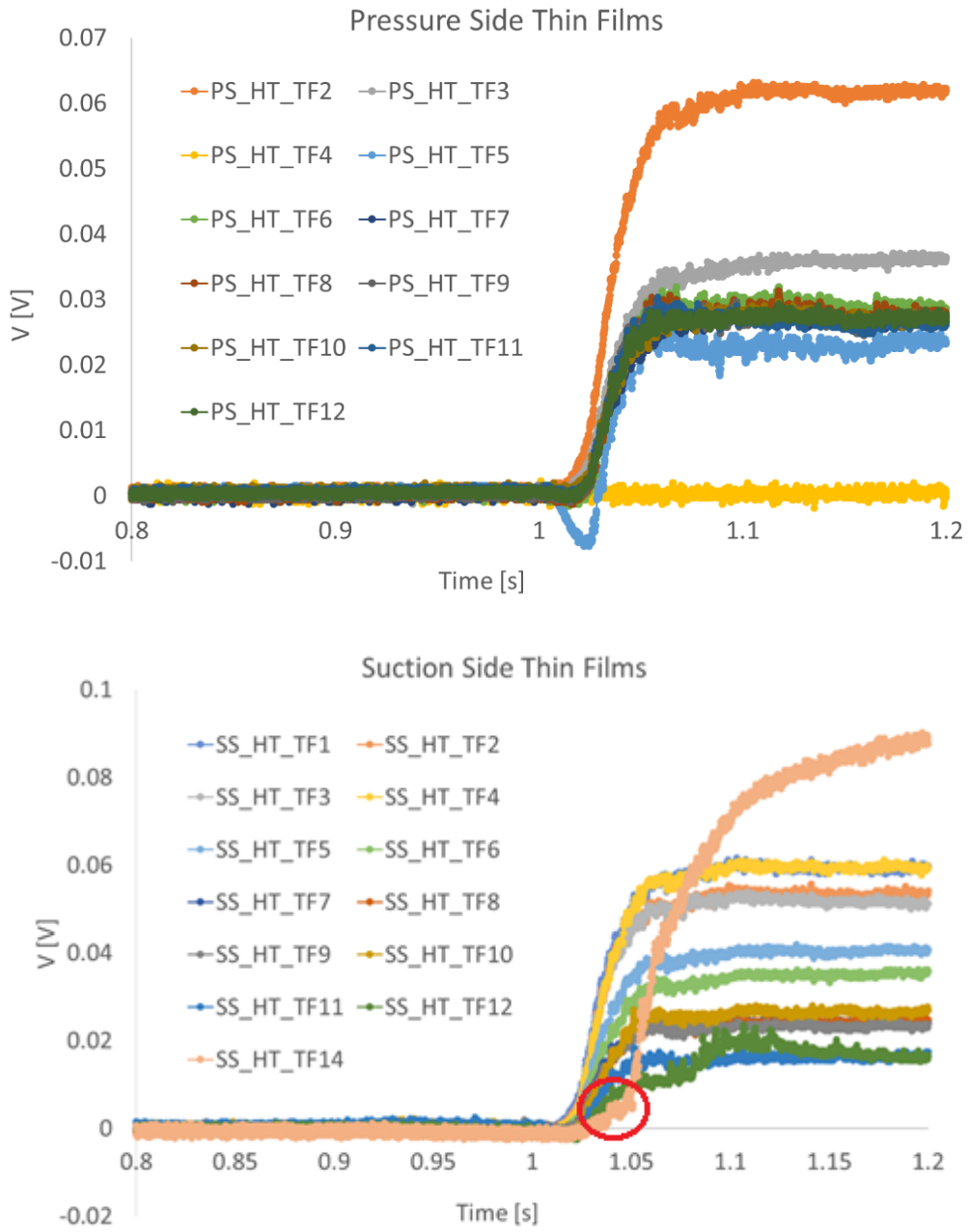

4Figure 4.58: Raw voltage trend over pressure side and suction side

The measurement technique consists first of all in recording the vane surface temperature increase during a blowdown test that produces a sudden gas temperature change. The gas temperature, shown in Figure 4.59 for all tests performed at 50% of the span, is monitored with a type K thermocouple.

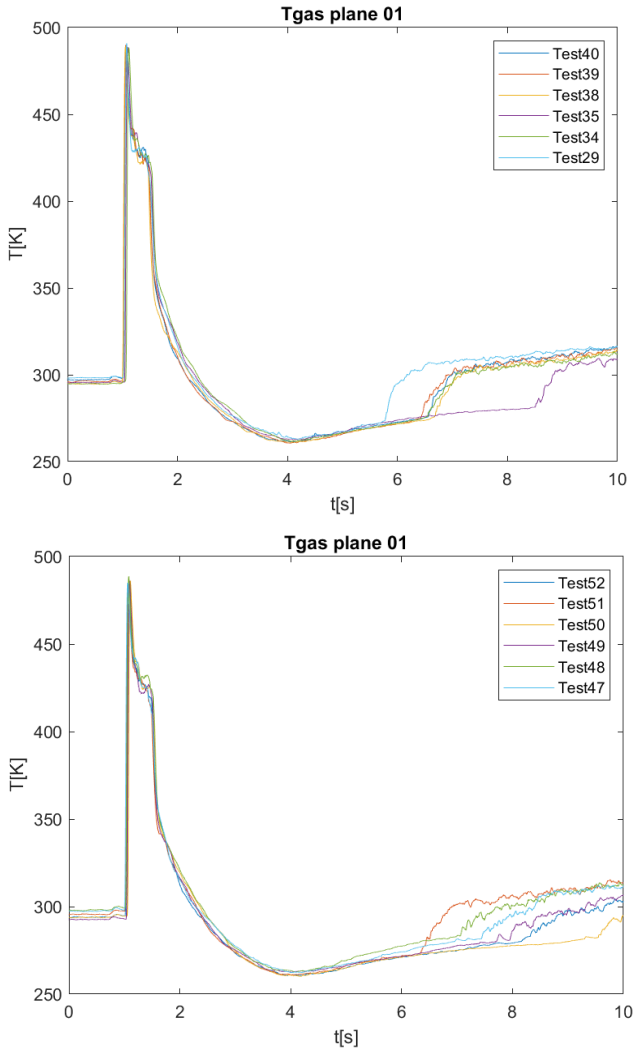

Figure 4.59: Gas temperature trend plane 01 for tests at 50% and 90% of the vane span

The testing time (~0.2 s) is so short that the inner extremity of the insert stays at ambient temperature during the blowdown. Typical evolutions of these temperatures during the blowdown are depicted in Figure 4.60, where the start instants of blowdown and purge injection are highlighted. The temperature of each sensor presents a different starting point (Figure 4.60a). To compute the heat transfer coefficient, the wall temperature was normalized with respect to the gas temperature relative to the considered test (Figure 4.60b).

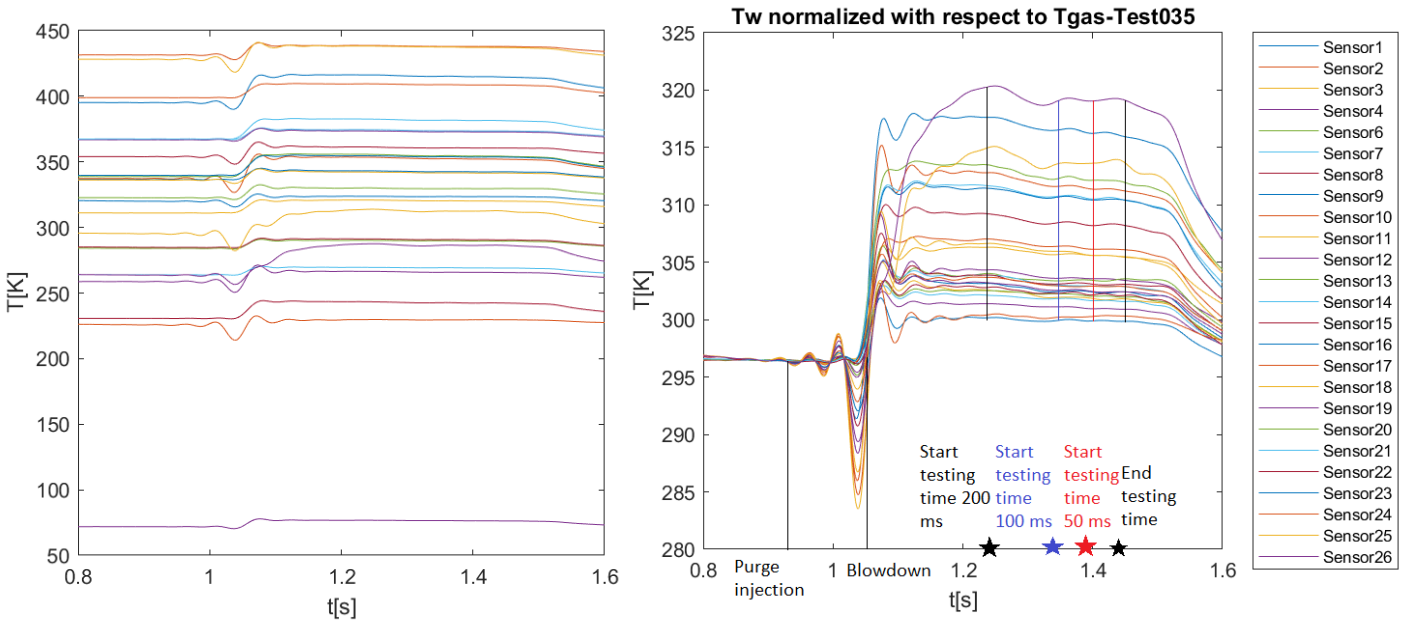

Figure 4.60: Typical wall temperature and gas temperature evolution

Comparing the normalization made for all the tests, acceptable discrepancies (± 1K) have been observed from test to test in the mean level of the wall temperature before the rising, so the drift of the Tw seems consistent and fixed, as reported in Figure 4.61.

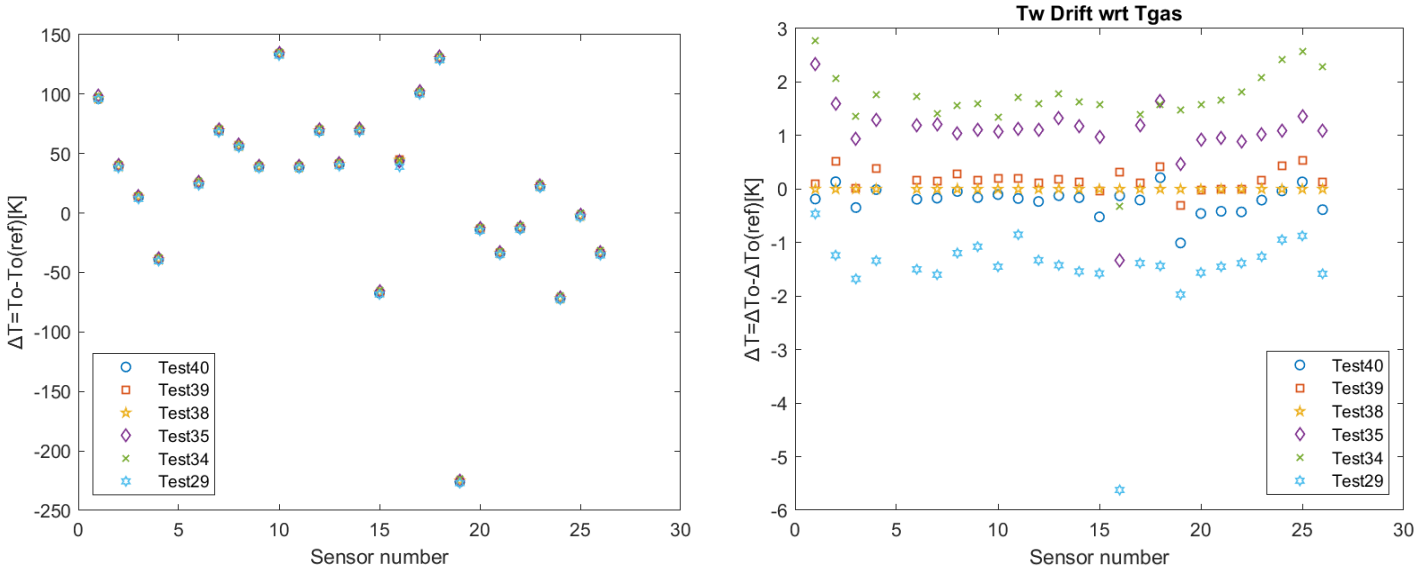

Figure 4.61: Test to test wall temperature drift with respect to the gas temperature

The heat transfer coefficient can then be derived from the wall temperature history, knowing the gas temperature and the convective heat flux, using the following equation:

$$h = \frac{\dot{q_{wall}}(t)}{(T_{gas} - T_{wall}(t))}$$

The gas temperature is measured with a thermocouple placed at the free stream. The surface temperature is given by the thin-film gauge, while the heat flux at the wall can be obtained using the method described in Chapter 2.3.2.2. The heat transfer around a vane is closely linked to the boundary layer state. For this reason, it is sensitive to the same parameters than the boundary layer such us: the Reynolds number whose increase can cause an overall increase of the heat transfer coefficient due to higher flow velocity or density and it tends to move upstream the transition onset; a high free stream turbulence level tends to enhance the overall heat transfer rate due to a higher mixing of the flow in the boundary layer; the curvature; the pressure gradient, the surface roughness, etc..

Heat transfer coefficient distributions along the vane at 50% and 90% of the vane span, obtained in the test campaign, are presented in Figures 4.62 and 4.63 where the HTC variability for different testing time windows and the repeatability of the experiment have been assessed. Each testing time window was obtained by imposing for each test the final time instant which corresponds to the time prior to the start of the pressure and temperature reduction; then establishing backwards three-time instants of the beginning of the testing time distanced from the final fixed point of 50 ms, 100 ms and 200 ms as shown in Figure 4.60b. As expected, the variability of the coefficient increases as the time interval considered increases, but the comparison of the average values shows that the variation, normalizing with respect to the value relating to the smallest time window, remains in any case less than 5%.

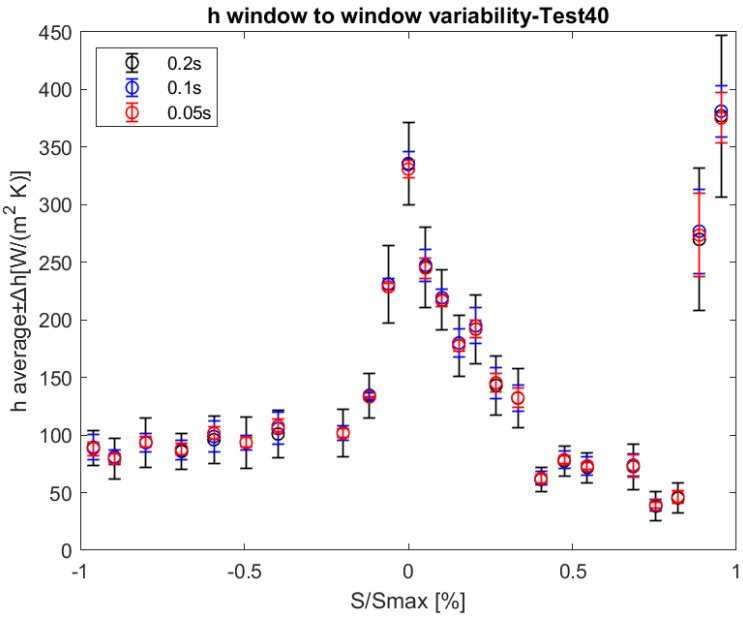

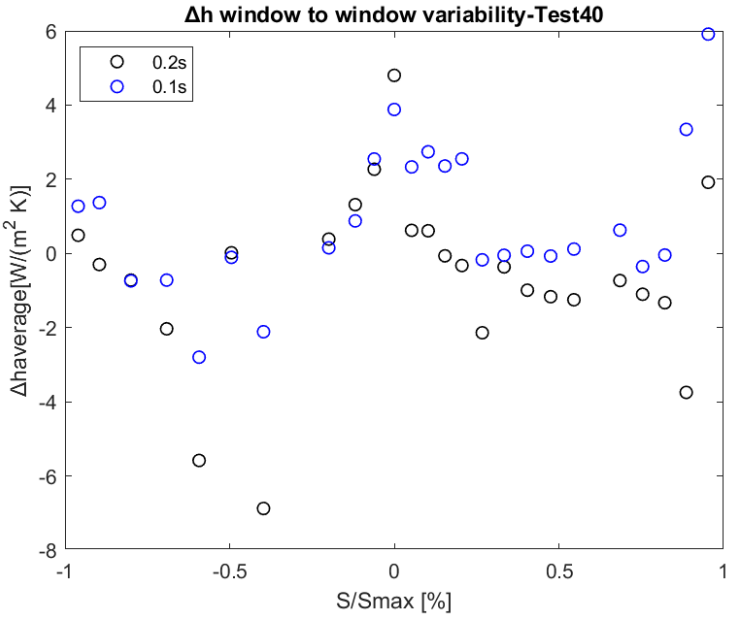

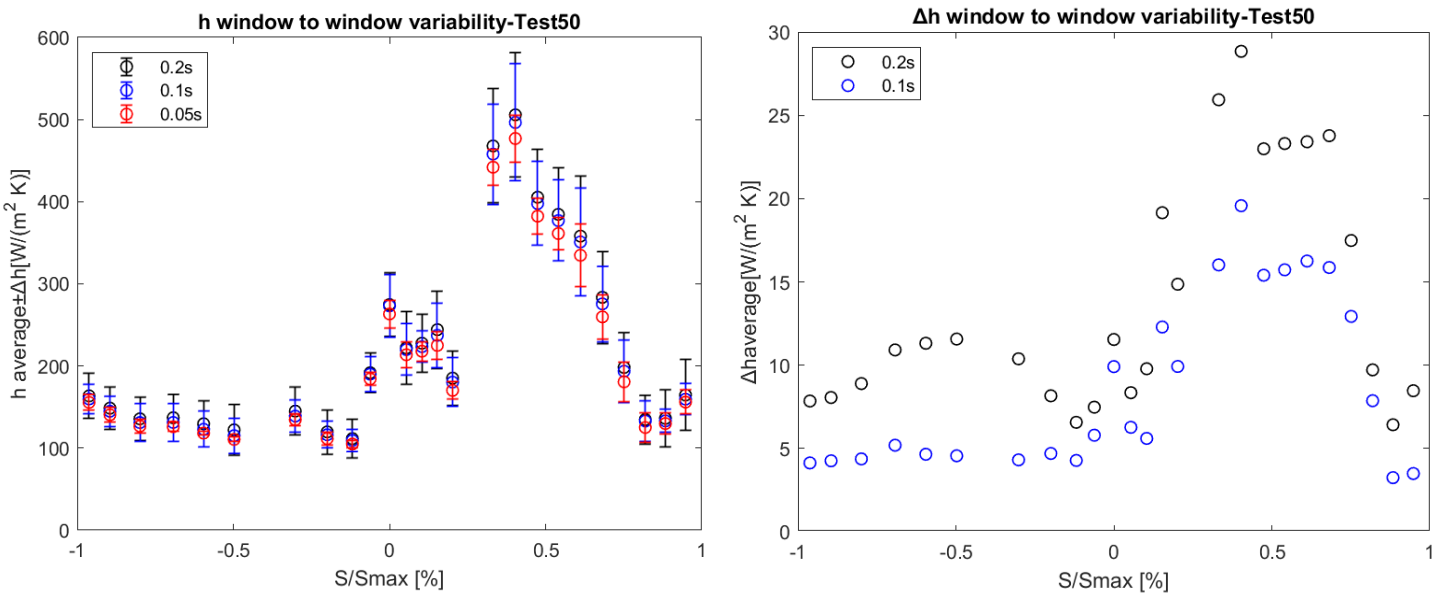

Figure 4.62: Heat transfer window to window variability respectively at 50% and 90% of the vane span

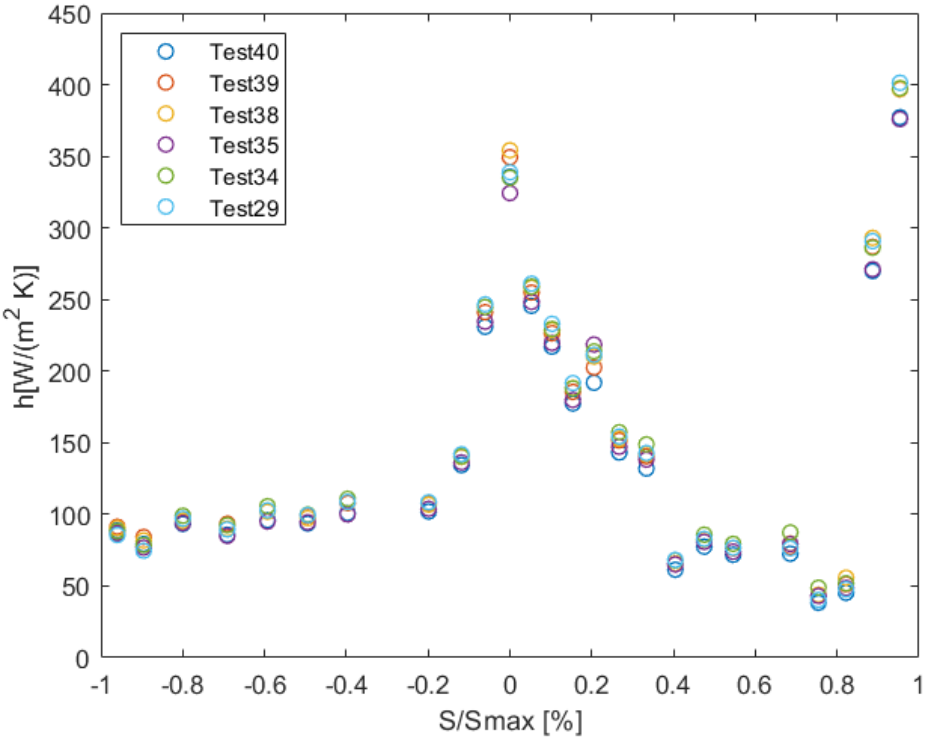

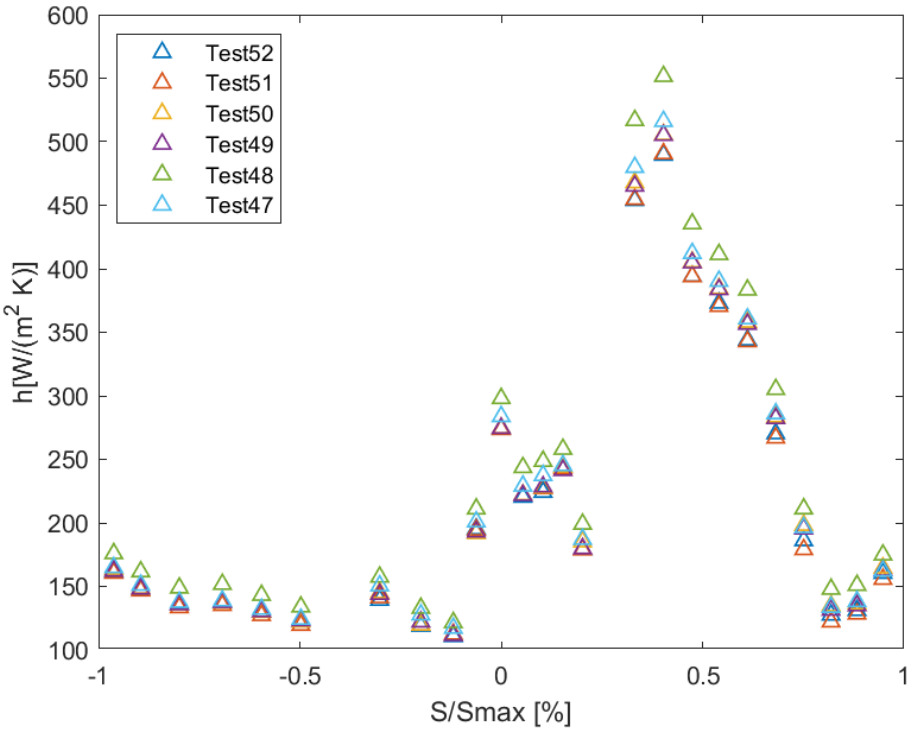

Figure 4.63: Heat transfer test to test repeatability respectively at 50% and 90% of the vane span

In the leading-edge area of Figure 4.63a, high heat transfer rates are observed with a maximum at the stagnation point. At this point, the velocity is zero and the boundary layer has not yet developed leading to very high heat transfer rates. Under the influence of both the large convex curvature and the favourable pressure gradient on the soon suction side and pressure side, a laminar boundary layer develops insulating the vane from the hot gas. Due to this, the heat transfer coefficient decreases very fast in these regions. Further on the pressure side, the curvature becomes concave. The boundary layer state depends then on the Reynolds number, the free stream turbulence level and on the importance of the destabilising effect of the concave curvature with respect to the stabilising effect of the favourable pressure gradient. However, the boundary layer remains in a laminar state. While on the pressure side the boundary layer remains laminar till the trailing edge, on suction side the flow becomes turbulent at about 88% of the curvilinear abscissa. In a turbulent boundary layer, high velocity fluctuations exist in all directions which cancel the previous insulating effect, so the heat transfer rates are even higher than at the leading edge. Figure 4.63b shows the HTC trend over the thin films positioned at the 90% of the vane span, where the highest value, unlike the previous case, is reached at 33% of the pressure side where the flow is turbulent.

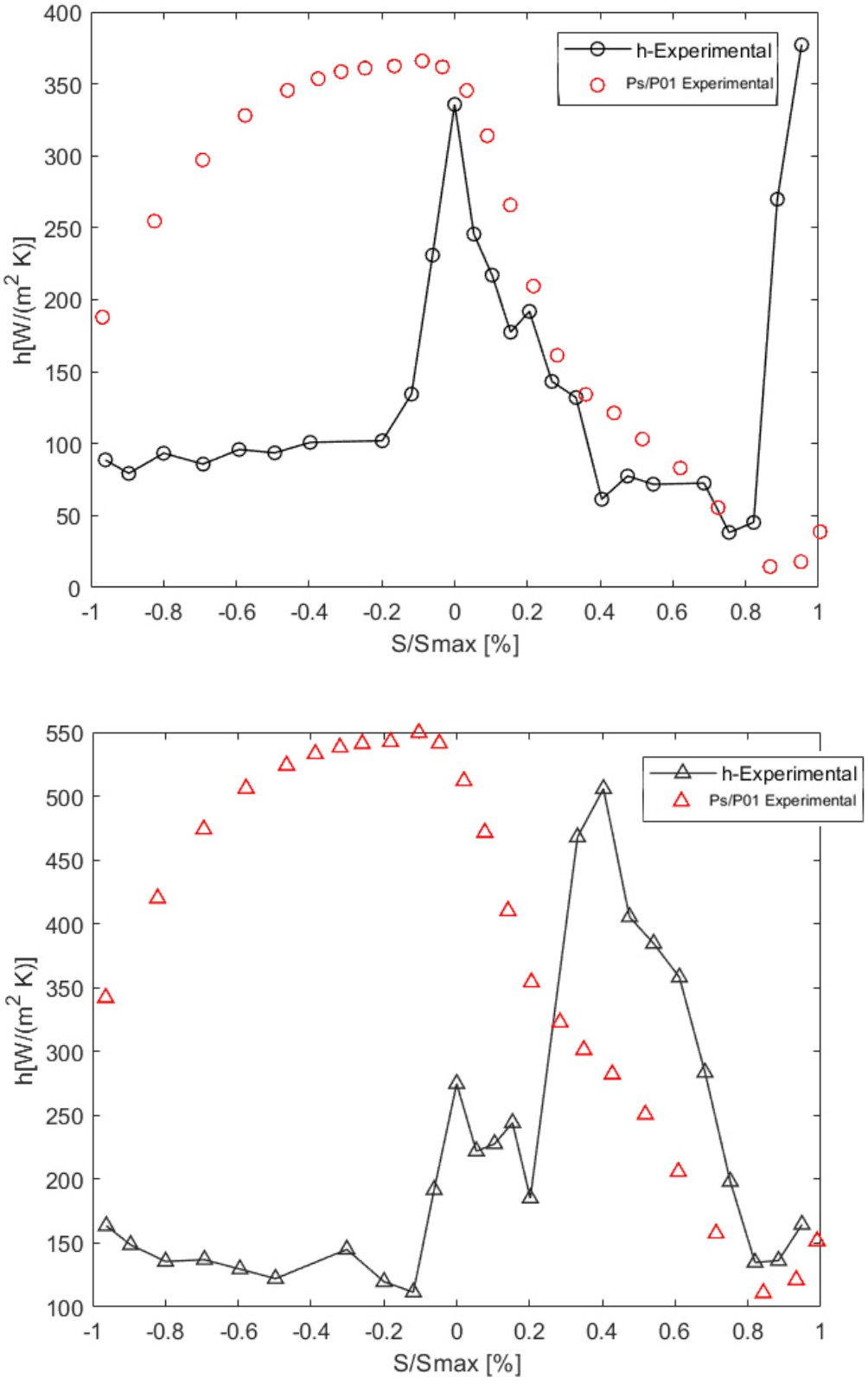

Figure 4.64: HTC trend and aerodynamic conditions comparison 50% and 90% of the vane span

In Figure 4.64, Ps/P01 along the vane, whose experimental trend is in agreement with the CFD numerical simulation, has been normalized to analyse the relationship between the heat transfer coefficient trend and the pressure ratio itself.

On the front part of the suction side (till 35%) the rapid decrease of the heat transfer coefficient corresponds to a strong acceleration of the flow. The latter tends to stabilize the boundary layer and maintains a slightly thickening protective layer between the hot gas and the vane while a decelerating flow would destabilize it and may promote transition and higher heat transfer. In this section the streamlines are well aligned between them. The point at 40% of the curvilinear abscissa characterized by a higher heat transfer coefficient value is an outlier that does not represent a real physical behaviour of the flow at that point. From 40% to 70% of the suction side a slight slope variation is detected in the Ps/P01 trend. This reduced acceleration involves the beginning of the transition from laminar to turbulent which is not yet complete, in fact, the heat transfer results in this stable zone, and it does not decrease as for the laminar boundary layer.

The point at 85% of the suction side is the point of maximum velocity. From here on, the flow decelerates; as a consequence, transition is dominant. On the rear part of the suction side the transition that has taken place and that is enhanced by the deceleration of the flow, is evident.

The last two points show the increase in heat transfer because of the increase of convection due to the presence of the turbulent boundary layer. Analysing Figure 4.65 in the following, the comparison between the heat transfer coefficient trend along the 90% and the 50% of the vane span is presented.

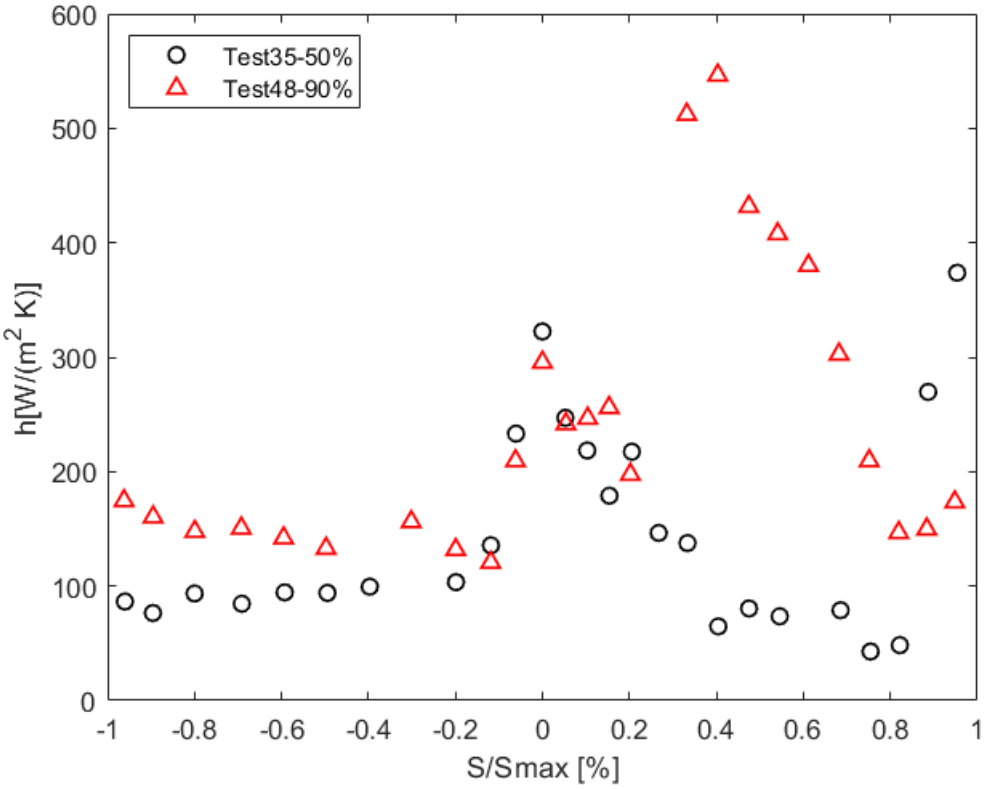

Figure 4.65: Comparison h trend at 50% and 90% of the vane span

On the first part of the suction side, at location 3-4 at 15%-20% of the curvilinear abscissa for 90% of the span, one observes a peak in the heat transfer coefficient. The same behaviour is seen at 50% span with a spatial delay but with less amplitude. A sign of earlier transition is noticed on the suction side, after location 5, where a steeply increase of the heat transfer coefficient at 90% on the span is present. On the front part of the pression side, the level of heat transfer is almost the same at 50% and 90% span with the same tendencies (deceleration between gages 1 and 4) while from 20% of the curvilinear abscissa the h coefficient is much lower on 50% of the span due probably to the lower rate of deceleration of the flow. The higher levels at 90% span were possibly attributed to the horseshoe vortex, which seems to have no influence at 50%. An increase in the turbulence level (from 9% at 50% to 18% at 90% of the span) enhances the overall heat transfer level mainly on the portions of the blade where the boundary layer is laminar (pressure side), as shown in Figure 4.65. The transition starts sooner for the highest turbulent rate. The transition on suction side with span=90% and Tu=18% is detected at s=30% compared with the transition at 50% of the span characterized with the 9% Tu detected at s=85%.

Once the heat transfer coefficient is computed, the Nusselt number is calculated using the stator chord and the air thermal conductivity.

$$Nu = \frac{h\, c_{vane}}{K}$$

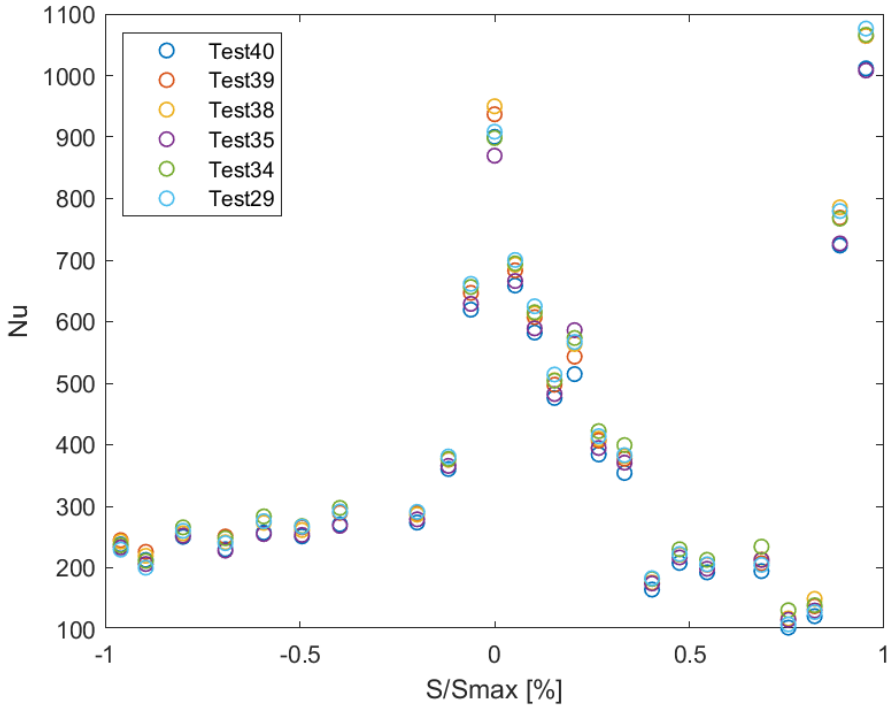

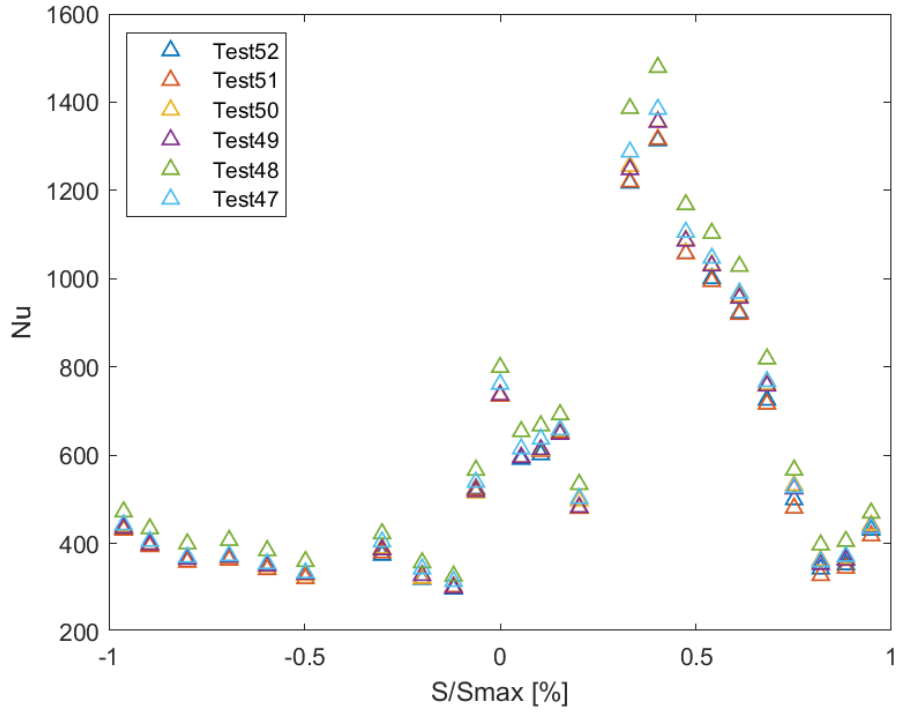

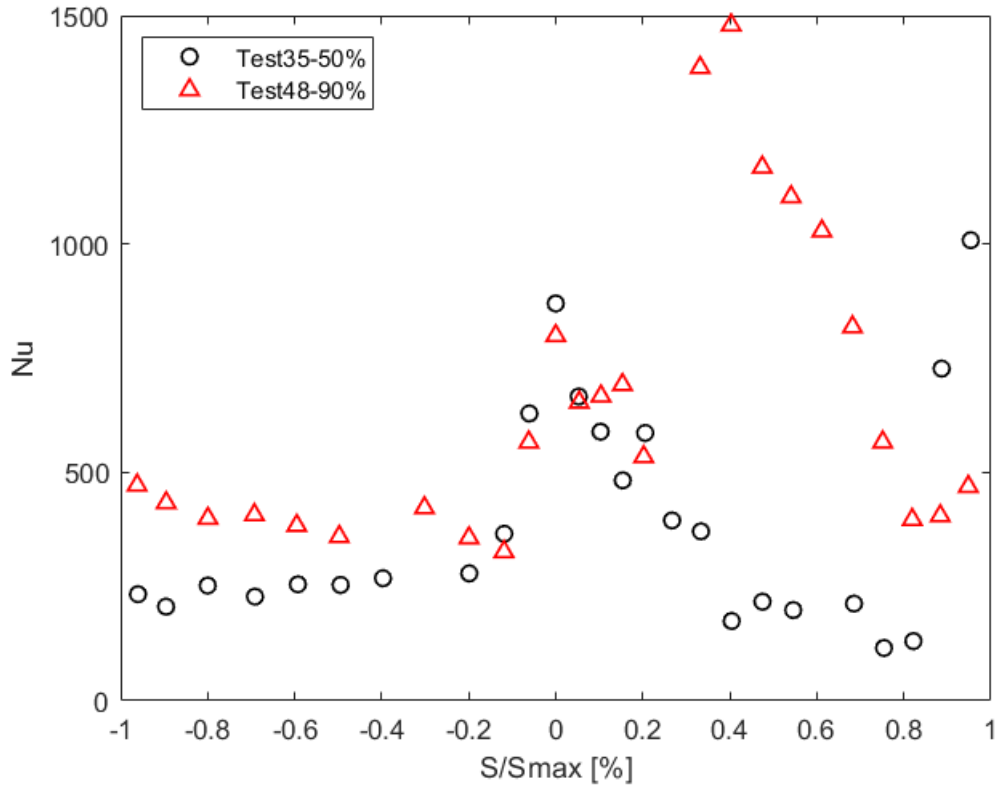

Figure 4.66: Time-average Nusselt number distribution: test to test repeatability at midspan and at 90%; b) comparison between the two investigated heights

As shown in Figure 4.66a, the highest flux level is measured in the stagnation region due to the lack of insulation from any boundary layer. It decreases rapidly as the boundary layer develops on both suction and pressure sides.

In the front region of the blade the boundary layer is very thin, and the heat transfer depends mainly on the Reynolds number and the free stream turbulence.

Due to the convex curvature and the favourable pressure gradient, the flow is continuously accelerated. This has a stabilizing effect on the boundary layer, which thickens progressively. As a result, the Nusselt number decreases. After a certain point the flow is decelerated, this may promote a transitional state and an increase of the heat transfer rate.

Around the blade leading edge, the boundary layer develops on a convex surface in a region of accelerating flow. In this region, it behaves like on the suction side, the Nusselt number decreases rapidly.

After the leading-edge region, the curvature changes from convex to concave. At this point, a separation bubble could appear but was not detected (one would see a plateau in the Mach number distribution and very low heat transfer rate).

The results confirm, as already described for the heat transfer coefficient, that at the midspan the transition to a turbulent boundary layer is induced on the late suction side whereas the boundary layer stays fully laminar on the pressure side. Being the rotor passage (see unsteady analysis) a large destabilizing factor, it seems that the boundary layer remains mainly laminar on the first part of the suction side and the pressure side, and transitional after. A fully turbulent boundary layer develops at the rear part of the suction side, part exposed to the passage of rotor blades, where the level of the Nusselt number namely ranging between 800 and 1100.

The Nusselt number distributions around the rotor blade at nominal conditions for the two investigated spans are compared in Figure 4.66. Relatively to the 50% of the vane span, level ranges between 800 and 870 are observed in the leading-edge region while the average level further downstream on the pressure and suction sides is of the order of 300. The highest values are observed at 90% and at 40% of the curvilinear abscissa respectively for the thin film placed at 50% and 90% of the vane span.

In cascade tests, the Nusselt number at the stagnation point of a blade can well be predicted using correlations by measurements around cylinders in cross flows. In literature does not exist theories able to estimate analytically the Nusselt number around a cylinder. The approach has to be empirical, experimental or numerical. Lowery and Vachon [17], proposed an empirical formula able to estimate the cylinder Nusselt number at the stagnation point. This formula has been used to predict the Nusselt number at the stagnation point at midspan for nominal conditions.

$$\frac{Nu}{\sqrt{Re}} = 1{,}01 + 2{,}624 * \left(\frac{Tu\sqrt{Re}}{100}\right) - 3{,}07 * \left(\frac{Tu\sqrt{Re}}{100}\right)^2$$

The correlation, that holds up a range between 0 and 64 of the parameter √ Re Tu), is a function of the Reynolds number and of the free stream turbulence intensity itself. Considering a turbulent intensity of Tu=9% and a Re=28000, the Nusselt number at the stagnation point is calculated and it is equal to 227.3 as shown in Figure 4.67 where an extrapolation of some experiments carried out by Schmidt et al. permitted to estimate the Nusselt number at our Reynolds. The estimated Nusselt number at the stagnation point is then plotted in Figure 4.68 as a function of Reynolds and the turbulence intensity. A turbulence intensity of 2.6% is needed in order to reach values of Nusselt number obtained with the data reduction analysis. This discrepancy can be due to the fact that in the present experiment, it is difficult to define turbulence intensity since the flow is submitted to periodic rotor passage at a rate of 4700 Hz, the correlation might be not accurate and the heat transfer, so the Nu number measured are affected by a large bias error.

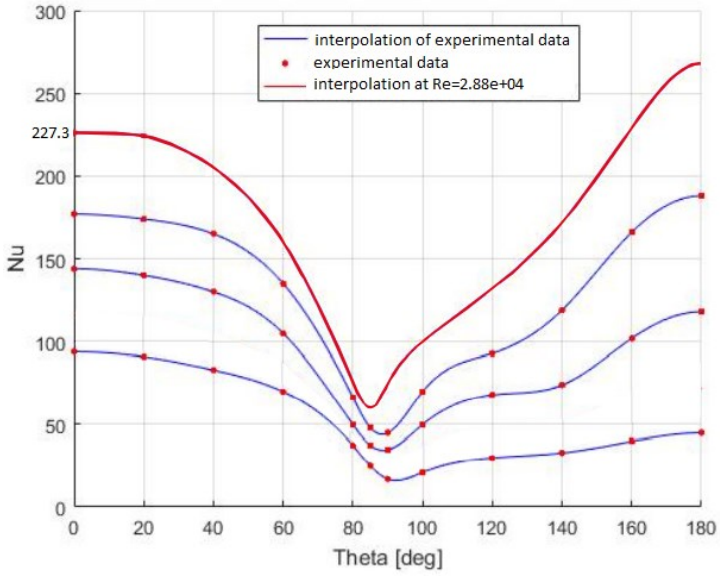

Figure 4.67: Nusselt number distribution around the cylinder

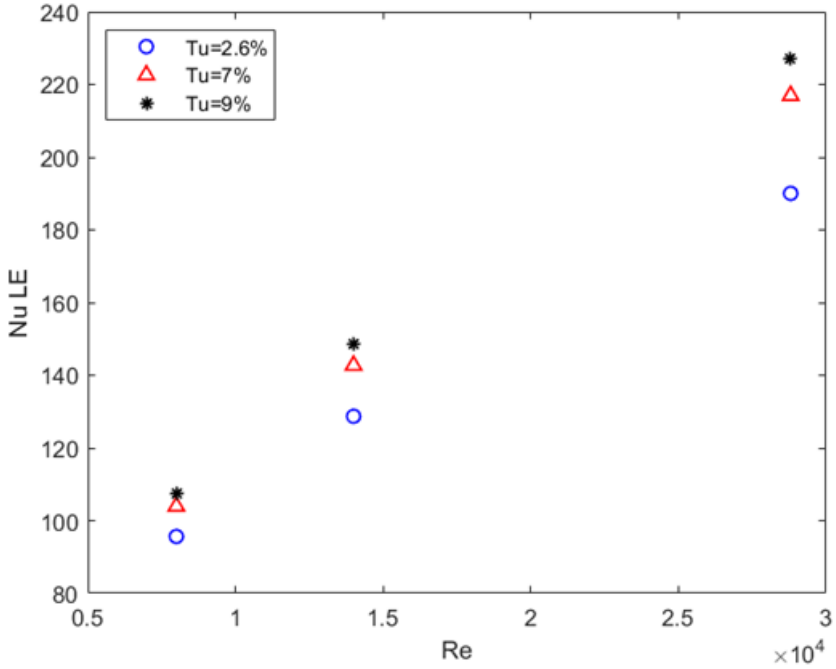

Figure 4.68: Nu number at the stagnation point as a function of Reynolds and the turbulence intensity

Many studies showed the strong link between heat transfer coefficient and Mach number distribution around the blade. The Mach number distribution around the profile is a key point to understand the aerodynamic parameter distribution along the vane. Experimentally, the isentropic Mach number distribution is derived from Equation 4.24 using wall static pressure taps measurements located along the vane profile and total pressure measurement performed with a pitot probe shown in Figure 4.69, where the isentropic Mach number distribution around the vane is plotted as well.

$$M_{isentropic} = \sqrt{((\left(\frac{p_0^{freestream}}{p}\right)^{\frac{\gamma-1}{\gamma}} - 1)\frac{2}{\gamma-1}} \tag{4.24}$$

The larger acceleration on the convex side causes a pressure which is lower than on the concave side. For this reason, the convex side is called suction side while the concave side is called pressure side. The statistical analysis of the heat transfer derived from heat transfer gauges allowed us to determine the boundary layer state.

In the laminar state, the flow is organized in successive layers sliding on top of each other without interaction between layers; the first layer is at null velocity (adherences to the wall) whereas the last is the velocity of the main flow; in this state, the boundary layer is usually thin and generates low losses; low-velocity fluctuations (see unsteady analysis) are observed as well as low heat transfer rates because the layer constitutes a thermal insulator. In the turbulent state, the flow is not well organized anymore but submitted to high-velocity fluctuations in all directions characterized by the turbulence level; the mixing of particles is very intense, the layer becomes thicker than the laminar one, high losses are generated, and high heat transfer rates are observed. The boundary layer thickens faster than in the laminar case. Steep velocity gradients are observed at the wall. A turbulent boundary layer generates high losses and high heat transfer rates which are both not desirable. The solution is to avoid the transition from a laminar state to a turbulent state. For this reason, many efforts were concentrated in understanding, modelling, and trying to predict transition.

In the transitional state, the boundary layer oscillates between a laminar and a turbulent state. This state is usually characterized by the intermittency factor (fully detailed later) which is, in a given point, the fraction of time during which the boundary layer is turbulent.

The existence and the location of transition depend on several parameters.

-A low Reynolds number tends to keep the boundary layer laminar; if the transition occurs, the low Reynolds number promotes the laminar separation without reattachment. A high Reynolds number promotes a turbulent reattachment with a recirculation bubble.

- A low turbulence level tends to keep the boundary layer laminar while a high free-stream turbulence level promotes by-pass transition.

-A negative pressure gradient tends to keep the boundary layer in a laminar state. On the pressure side, the pressure gradient remains negative all along the blade favouring a laminar on all the surfaces. On suction side, a large negative pressure gradient can often be maintained up to the throat region.

In the case of a subsonic flow, a deceleration follows promoting transition. In the case of transonic flow, the shock-boundary layer interaction will cause transition.

For these reasons, the suction side is responsible for a large part of the overall losses and is much more investigated than the pressure side.

- A convex surface tends to stabilise the boundary layer due to a curvature effect (the flow accelerates). In the nose region of the vane, the boundary layer stays laminar mainly due to the large convex curvature. A concave curvature has a destabilising effect which, on the pressure side, is in concurrence with the favourable pressure gradient.

- A high surface roughness promotes transition. For this reason, the vanes tested in a cascade have a very good surface finish in order to eliminate this effect.

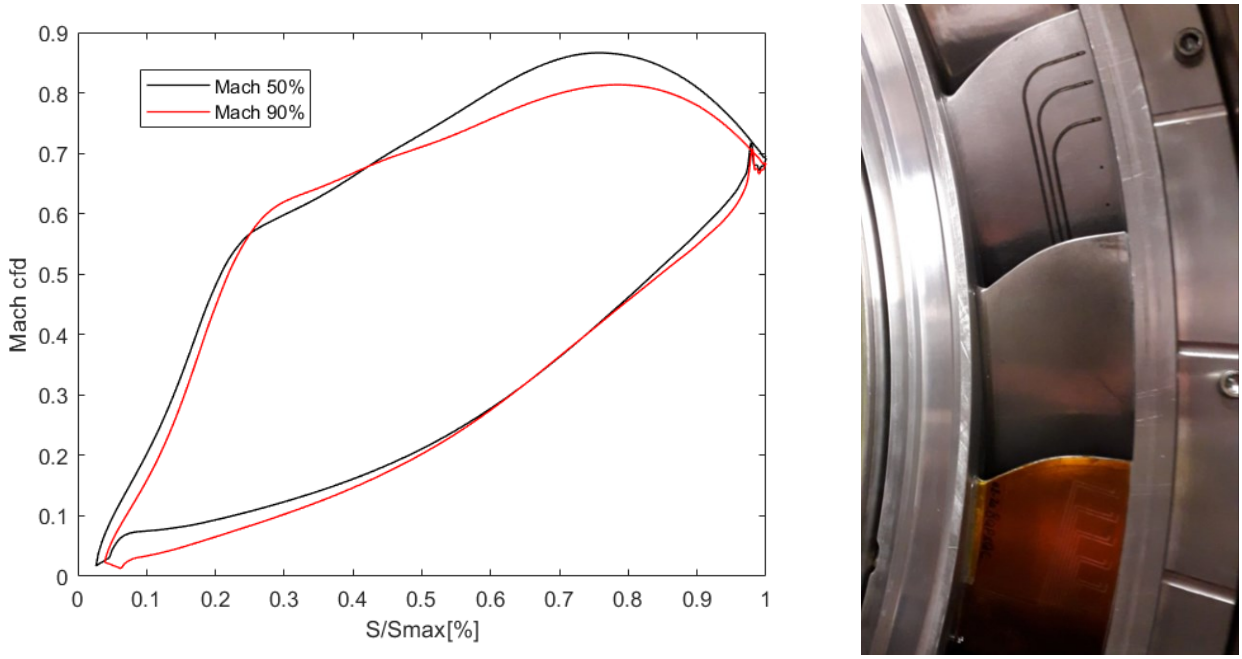

Figure 4.69: Mach distribution around the instrumented vane

4.1.4 Unsteady data processing

In this section, the variations of heat transfer on a stator blade due to the passage of the rotor are considered. The fluctuations felt by the vane occur at the rotor passing frequency:

$$f = \frac{RPM}{60} N_{blades}$$

With 48 rotor blades, a nominal speed of 5800 rpm, the blade passing frequency will be of 4.7 kHz.

The goal of the spectral analysis is to decompose the data into a sum of weighted sinusoids. This breakdown makes it possible to evaluate the frequency content of the phenomenon under examination. The phenomenon under consideration is not concentrated in a narrow frequency band but is distributed over a frequency range that reaches 500 kHz (see Figure D1). However, being the signal filtered at 50kHz, the unsteady analysis will focus on that frequency range. In the case in question the PSD is calculated due to the fact that the random effects could be able to obscure the underlying desired phenomenon. The quality of the signals acquired is, hence, investigated with the Welch's method through the MATLAB's pWelch function. Welch's method for estimating power spectra (also called the weighted overlapped segment averaging method and periodogram averaging method) is carried out by dividing the time signal into successive blocks, forming the periodogram for each block, and averaging. The latter permits to smooths out the random effects of noise. In other words, it is just an average of periodograms across time. The pWelch function allows to window the signal, takes the magnitude-squared of the DFT, computes the vector of frequencies and use DFT averaging to compute the so-called Welch power spectral density estimate. If we call M the length of each segment and S the number of points to shift between segments, the number of new points in each segment (the number of points in common to two adjacent segments) is M - S. Two adjacent segments are said to overlap by M - S points. When S ~ M, the segments do not overlap. When S = 0.5M, the segments contain 50% overlap. The M-point sequence w[m] is the window function. Some common windows are the rectangular, Harm, Hamming, Blackman, Blackman-Harris, and Kaiser-Bessel.

For this analysis, a hamming window that concentrates the signal in a narrower peak has been used and the signal was divided into 5 windows with a 90% of overlap. These parameters have been set in order to obtain a result as precise as possible without losing resolution.

The comparison between the Welch's method and the FFT is shown in Figure 4.70. The two curves overlap at high frequencies while the average made through the Welch method leads to low frequency differences.

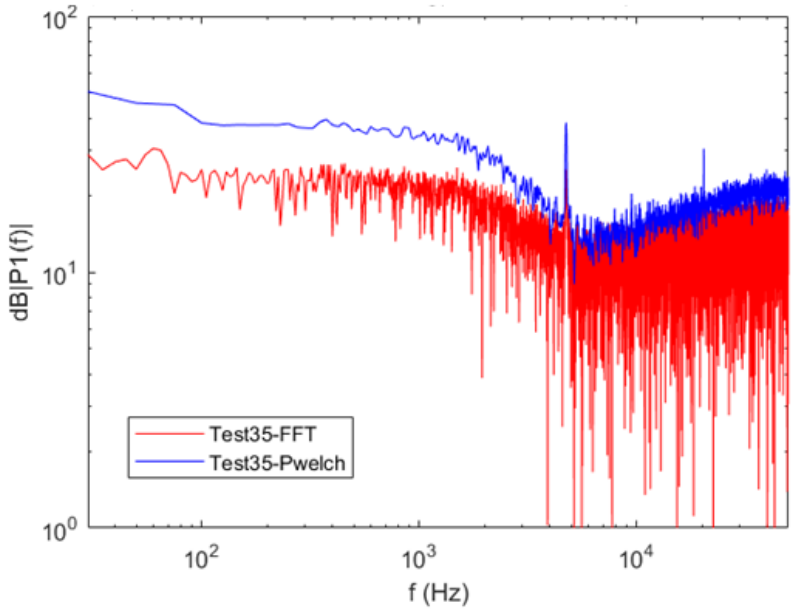

Figure 4.70: Comparison FFT and Welch's method

The PSD of two different signals is presented in the Figure 4.71 that corresponds to a gauge located in the middle of the pressure side. In this region, the unsteady interaction between the stator and rotor is not as strong as in the trailing edge region. The one from figure 4.72 corresponds to a gauge located in the rear part of the suction side, where the fluctuations in surface temperature (and therefore in Nusselt) are expected to be larger than anywhere else in the blade due to the strong interaction of the rotor blade passage. Thus, the vane passing frequency and its harmonics can be clearly identified in the spectrum, indicating one large fluctuation per period at the RPF. The number of visible harmonics depends on the location of the insert: at midspan their amplitude is higher as their energy content and the first harmonic is of the same order of magnitude as the dominant frequency as shown in Figure 4.73.

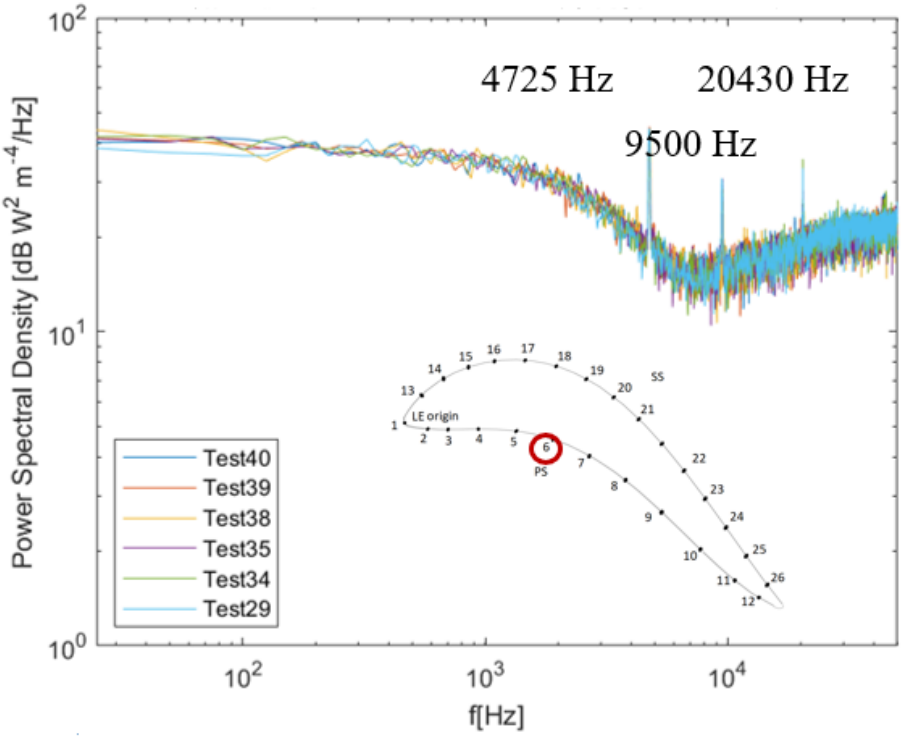

Figure 4.71: PSD sensor 6 on pressure side

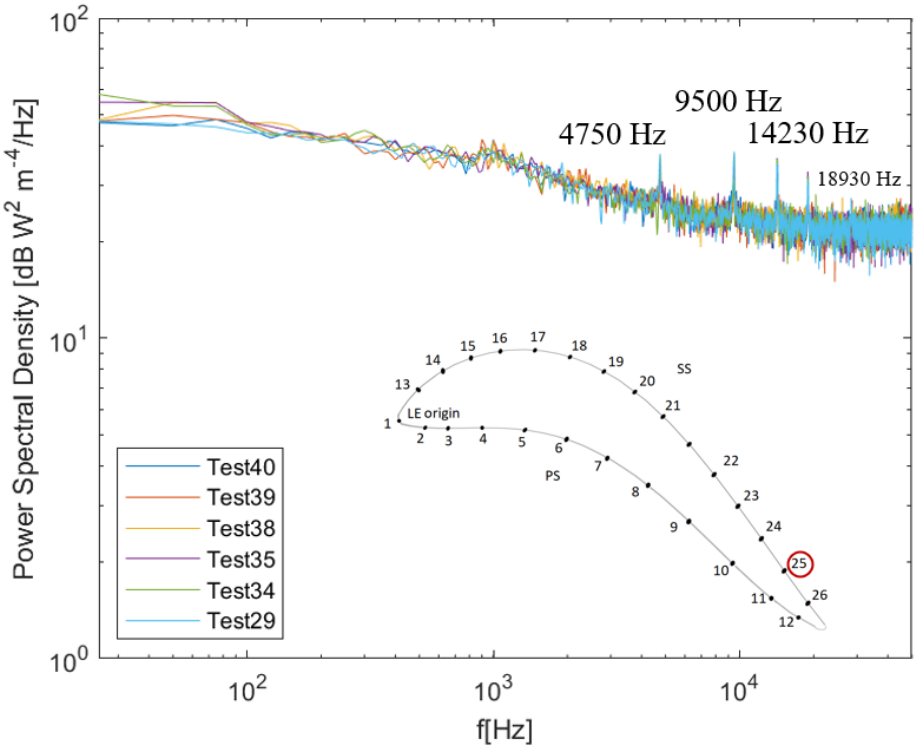

5Figure 4.72: PSD sensor 25 on suction side

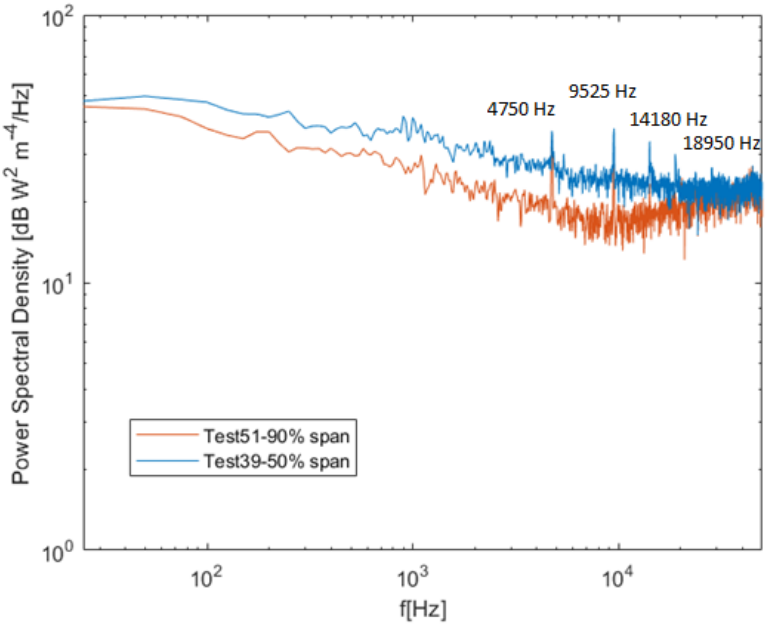

Figure 4.73: Comparison PSD sensor 25 at 50 and 90% of the vane span

To identify the frequencies that are not related to the physical phenomenon analysed, the frequency content in the time interval prior to the rising, therefore in the absence of flow, was analysed. Therefore, an initial segment of 0.1s before the beginning of each test was analysed in order to verify the consistency of the power peaks and their power spectral density. Figure 4.74 shows that one distinct peak can be observed at around 20kHz for all sensors along the vane. In this way, at these frequencies, the phenomenon appears not to be flow related but could have an electrical nature.

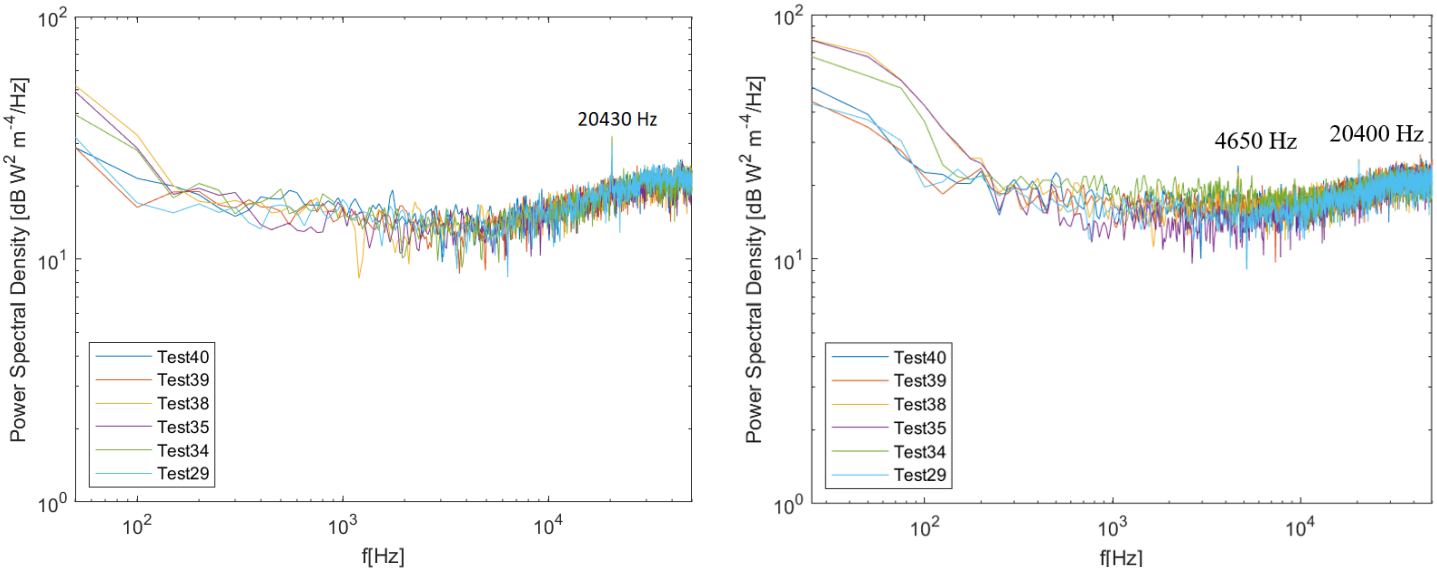

Figure 4.74: Power spectral density before the start of tests for sensor 6 (PS) and 26 (SS)

In Figure 4.74 relative to the last sensor of the suction side, despite being relative to an interval preceding the presence of the flow, it is possible to observe a peak at a frequency comparable to the rotation frequency of the rotor that has not yet reached the nominal condition.

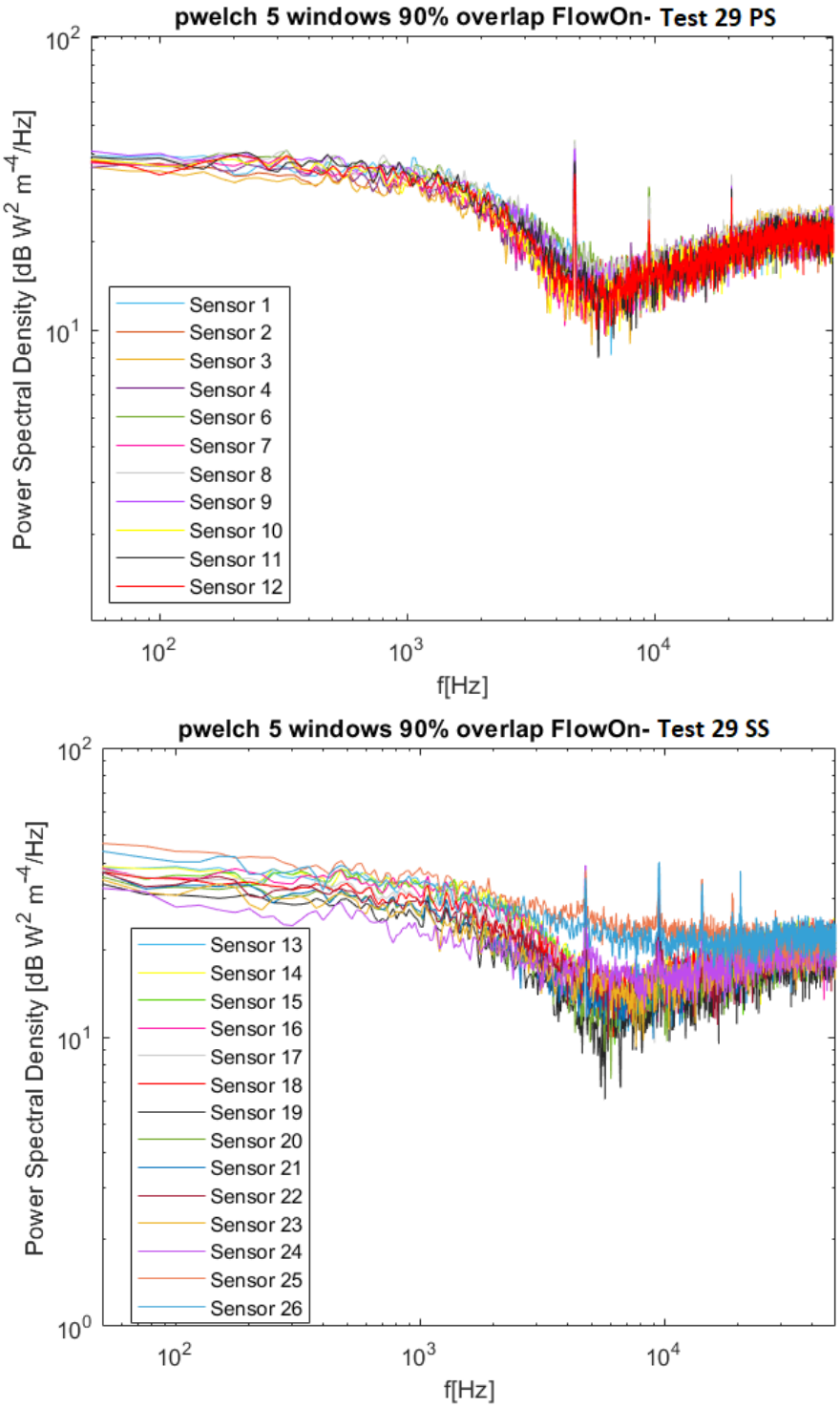

Figure 4.75: PSD for all the sensors at midspan

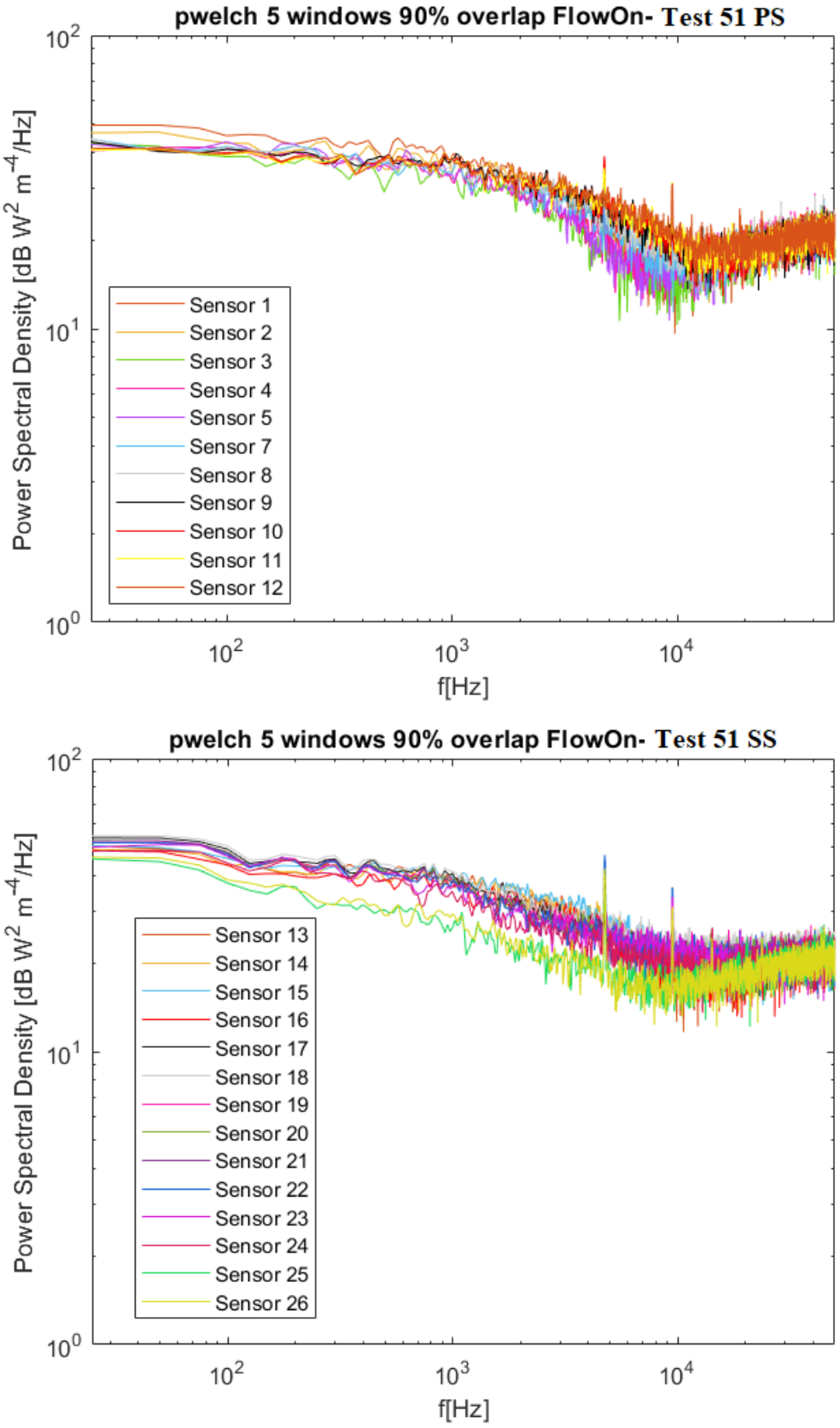

Figure 4.76: PSD for all the sensors at 90% of the vane span

Analysing the root mean square trend depicted in Figure 4.77 and 4.78 it can be highlighted that at nominal conditions, the amplitude of the fluctuations is much higher at the rear part of the suction side confirming the transition of the flow from laminar to turbulent and it decreases when going from the towards the leading edge.

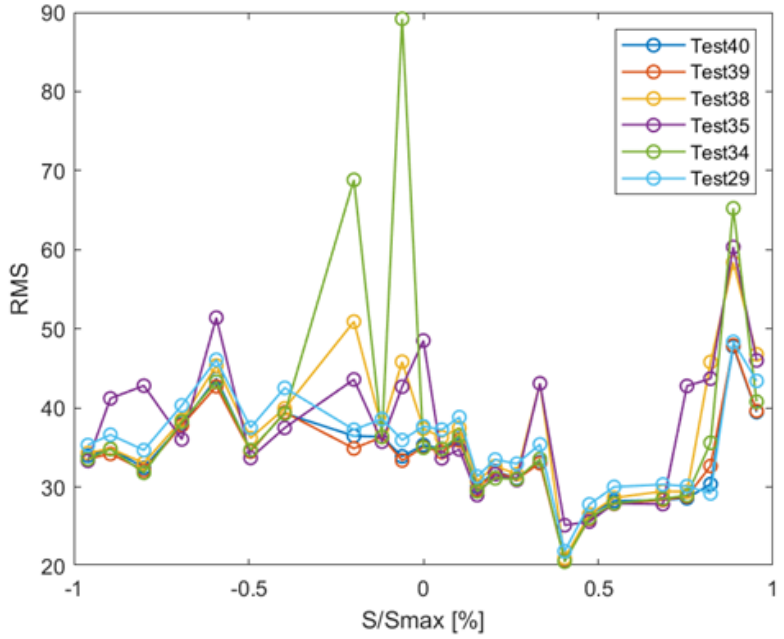

Figure 4.77: Root-mean-square's h over testing time at midspan

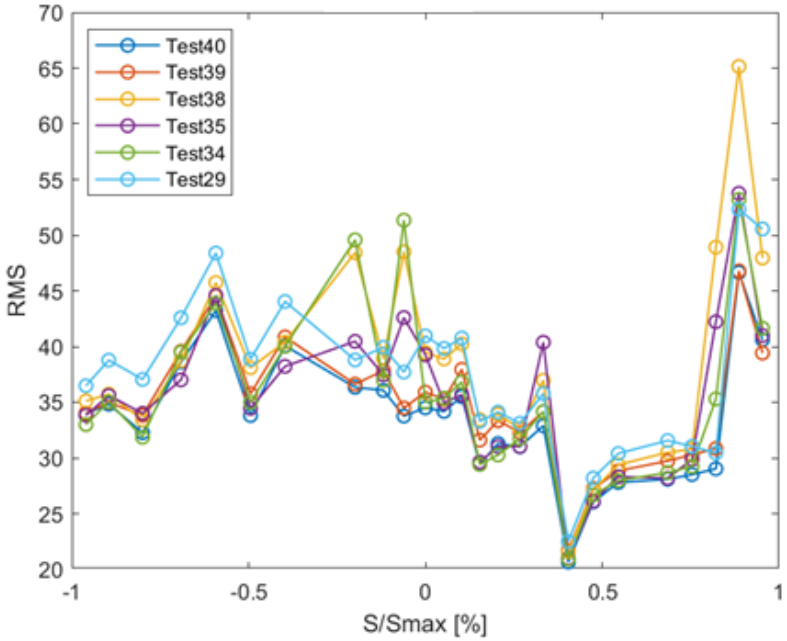

Figure 4.78: Root-mean-square's h over 50 ms at midspan

The increase of the fluctuations level can be observed from the vane position 23, reaching the peak on the sensor 25 and afterwards decaying to values higher than before the start of transition. The profile of the RMS indicates that no significant delay or hasten of transition is taking place during different tests. However, a test-to-test difference can be pointed out for sensors 2 and 4 of test 34 which present an increase in the fluctuations with respect to the others. This is due to a noise whose trend is also visible in the range of time prior to the start of the test itself and is therefore not attributable to the flow, as detailed in Figure 4.79. Indeed, as shown in these Figures, just considering a shorter time interval (50 ms VS 200 ms) the analysis is not corrupted by this noise and the Figure 4.79 illustrates the difference in terms of heat transfer coefficient trend between the sensors contaminated with the noise and the other ones.

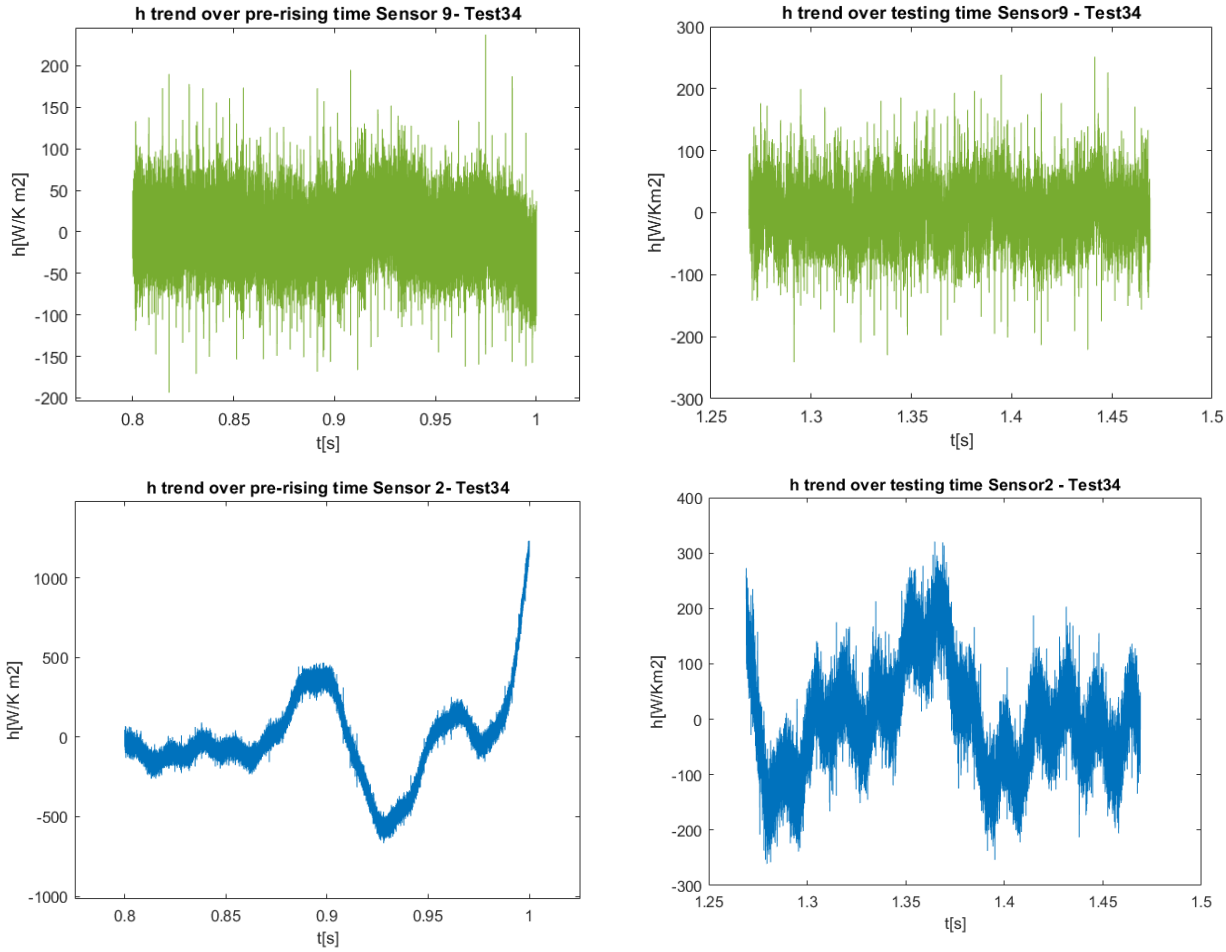

Figure 4.79: Comparison h trend over pre-rising period for sensors 2 and 9

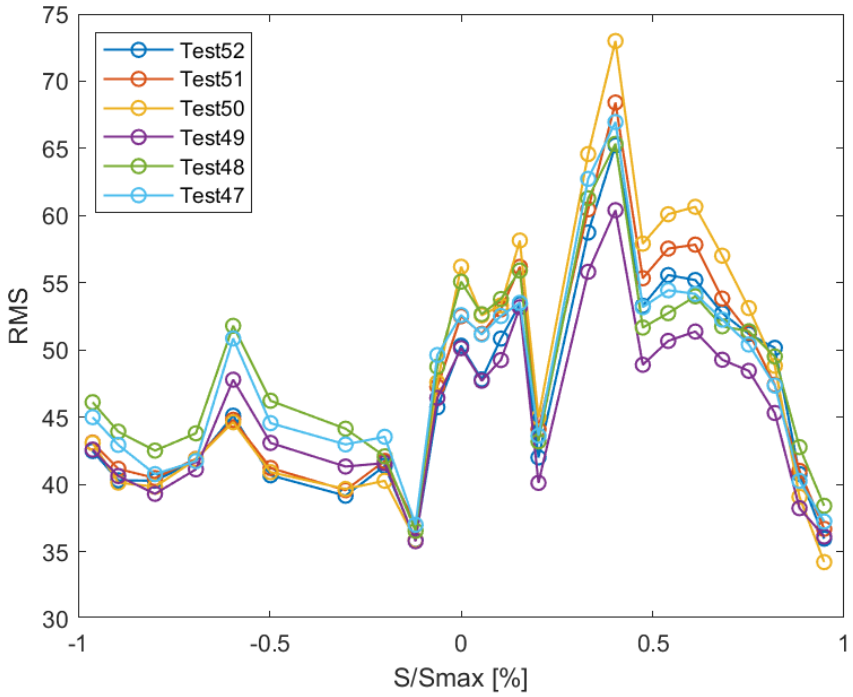

Figure 4.80: Root-mean-square trend at 90% of the vane span

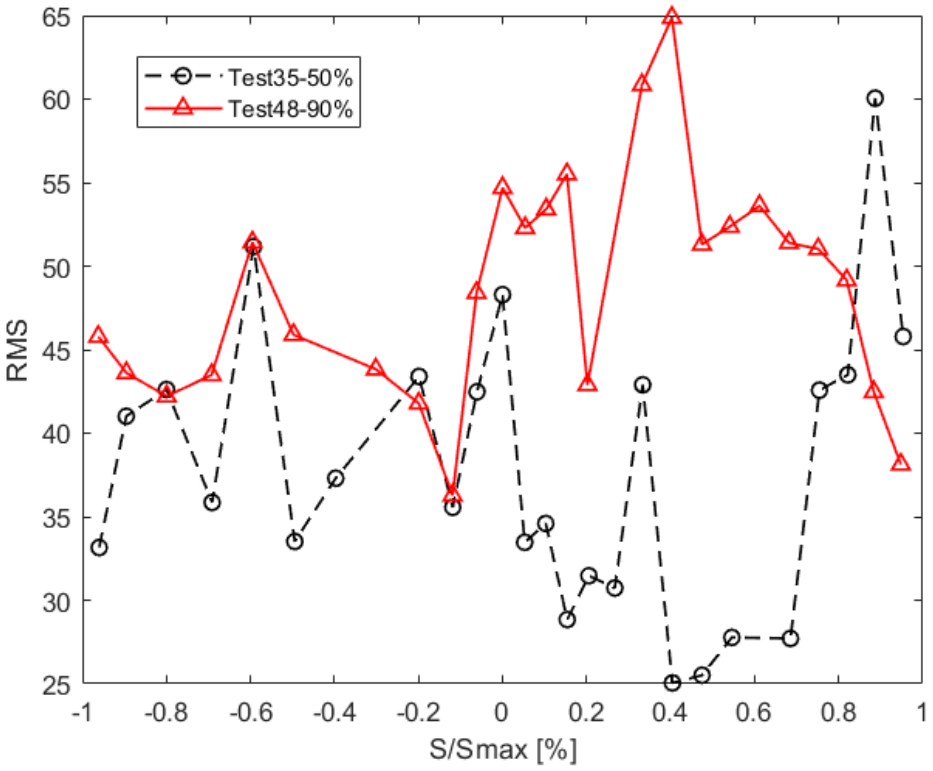

Figure 4.81: Root-mean-square comparison between the sensors at 50% and those at 90% of the vane span

4.1.4.1 Intermittency factor

Intermittency functions are regarded in literature as the favoured tool in predicting transition amongst the turbomachinery community for they can quantify the turbulence evolution within a laminar flow and result solely from experimental data. This parameter along with the skewness will be analysed in the last two paragraphs as described in [19]. The intermittency factor represents the fraction of time during which the flow over any point P on the surface is turbulent. Therefore, its value changes along the transition, passing from 0 in laminar flow to 1 in a fully developed turbulent boundary layer. Since the flow in the transition region is part of the time laminar and part of the time turbulent, Emmons presumed that the time-averaged flow quantity f at any streamwise position may be considered as a superposition of its laminar and turbulent values, respectively f_{lam} and f_{turb}, according to:

$$f = (1-\gamma)f_{lam} + \gamma f_{turb}$$

The intermittency factor (shown in Figure 4.84) has been computed using the power spectral density integral. Coton et al. [18] present a new method to compute the intermittency factor based on the power spectral density of the flow. In their experiments, the authors observe an increase of the high frequencies' energy content with the evolution of the transition process as shown in Figure 4.82 and thus define the intermittency factor in the following manner:

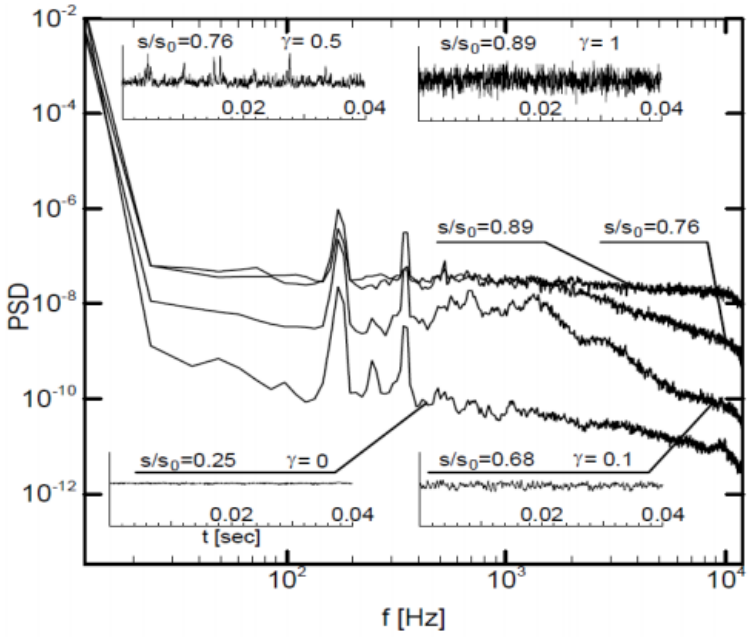

Figure 4.82: PSDI method

$$\gamma(x) = \frac{PSDO(x) - PSDI_{lam}}{PSDI_{turb} - PSDI_{lam}}$$

The PSDI correspondent to a laminar and the turbulent position is a choice of the user and, to have a maximum intermittency of one, the highest PSD integral have to be selected as the turbulent one.

Analysis of the frequency spectrum is performed using the MATLAB's function pWelch for different tests focusing on the region of transition. The evolution of the frequency content is showed on Figures 4.83 and 4.85 for different vane position along the suction side rear part and front part respectively.

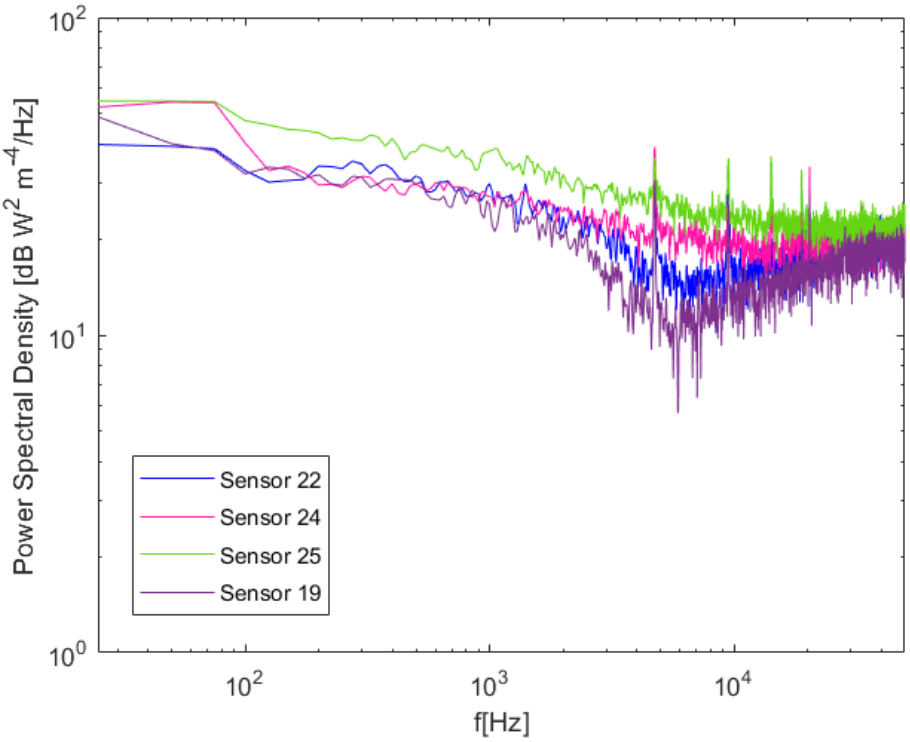

Figure 4.83: Power spectral density on suction side at midspan

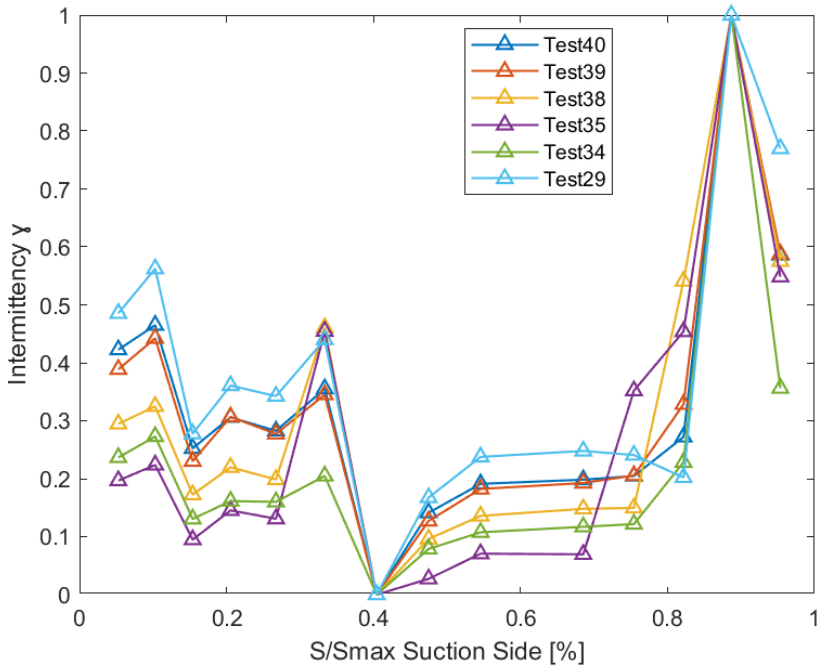

Figure 4.84: Intermittency factor through Power Spectral Density Integral at midspan

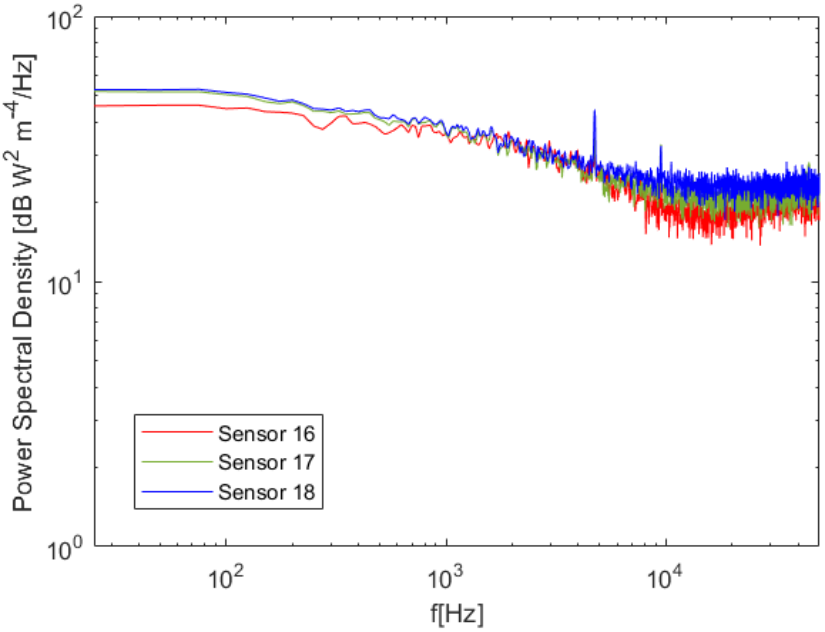

Figure 4.85: Power spectral density on suction side at 90% of the vane span

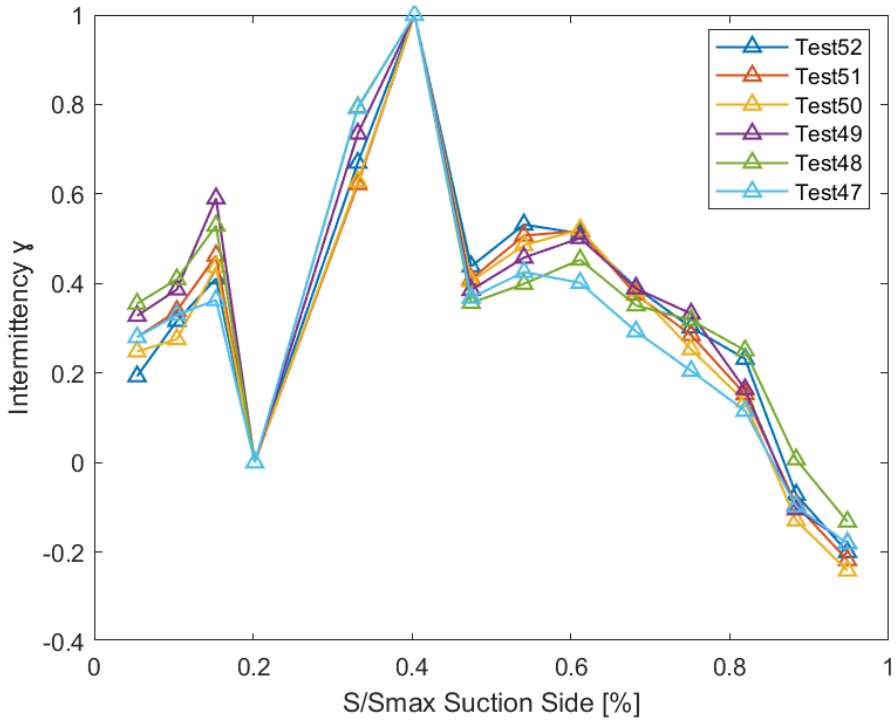

Figure 4.86: Intermittency factor through Power Spectral Density Integral at 90% of the vane span

4.1.4.2 Skewness

The skewness provides information on the degree of asymmetry of the fluctuations of a signal, and is computed as indicated in the following equation:

$$S_k = \frac{\frac{1}{N}\sum_{i=1}^{N}(h(t_i) - \bar{h})^3}{RMS^3}$$

The physical interpretation of this variable is the following. The RMS weights the level of the mean fluctuations, the skewness represents the degree of asymmetry of the statistical distribution around the mean value. For a fully laminar boundary layer (γ = 0), a given variable as h is evenly distributed and S_k=0. If the boundary layer experiences some turbulent portions, the skew becomes positive (with a maximum of S_k around γ = 0.25).

This is due to the fact that the heat 'transfer increases during the short duration appearance of turbulent spots within a predominantly laminar boundary layer. If equal laminar and turbulent portions exist (γ = 0. 5), h is evenly distributed and the skew zero again. As the transition process proceed, turbulent portions dominate and Sk becomes negative (with a minimum around γ = 0.75). At the completion the fully turbulent boundary layer (y = 1) presents again an even distribution and Sk=0

Hence, during transition from laminar to turbulent, a trend similar to the one present on Figure 4.87 is expected. Nevertheless, after reaching the positive peak, such behaviour cannot be completely observed as showed in Figures 4.88 and 4.89. This can be attributed to the lack of a sufficient number of sensors in the area of the vane where the transition is being analysed.

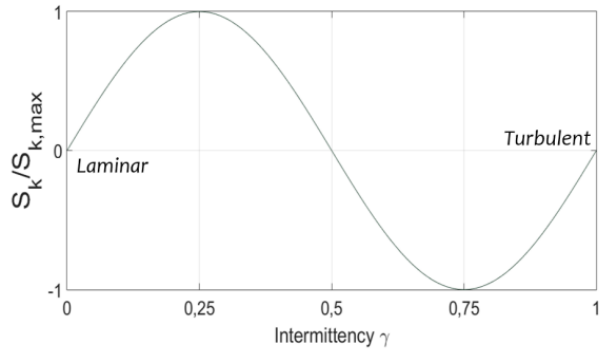

Figure 4.87: Theoretical skew distribution

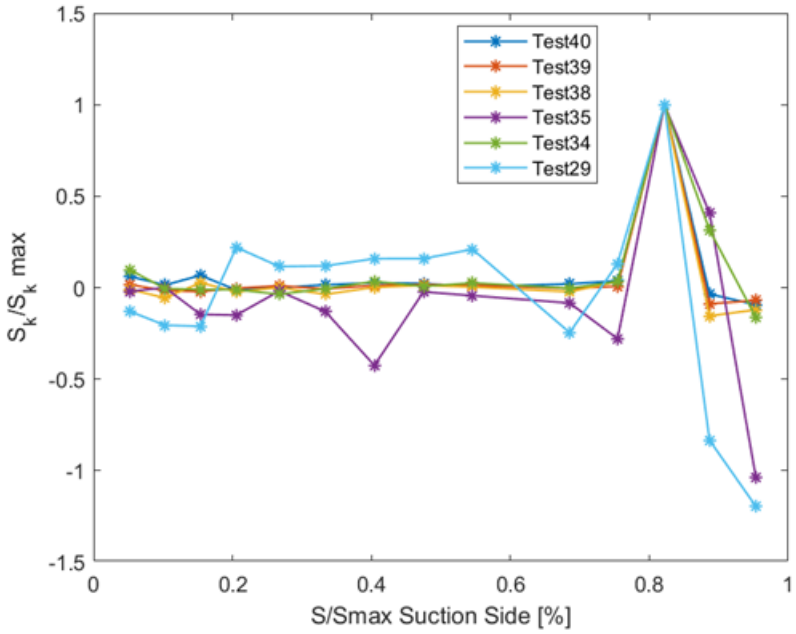

Figure 4.88: Skew trend over suction side at midspan

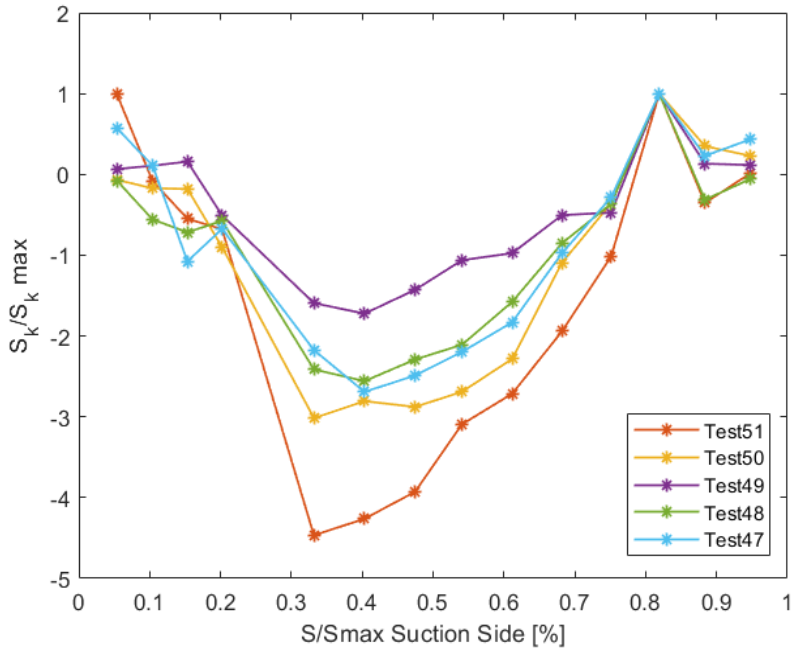

Figure 4.89: Skew trend over suction side at 90% of the vane span

Chapter 5

Conclusions

This thesis presented the investigation of the heat transfer along the vane of a high-pressure unshrouded turbine that took place through testing in a quasi-isentropic compression tube facility, at engine-representative conditions in the high-speed turbine facility of the von Karman Institute.

In the first part of the report the facility description and the delineation of the sensors used in the test campaign was provided. Measurements of high response thin films coupled with thermocouples provided the time-resolved and the time-average heat flux; pressure port transducers allowed the computation of the pressure distribution along suction and pressure side and thermocouples allowed the measurements of the inlet and outlet flow conditions.

This part was then followed by the section dedicated to the description of the calibration processes that made it possible to obtain the relations that bind the acquired signal to the temperature. The analysis sows that the calibration should be performed in an oil bath to obtain a 25 % better result. The digitizer's internal calibration leads to an uncertainty of ±0,2°C compared to the ±0.15°C obtained with the calibration in the oil bath.

Subsequently, the analysis of steady and unsteady heat transfer was carried out. The new computationally method developed by Oldfield allowed to obtain the heat flux starting from the trend of the voltage. The trend of the heat transfer coefficient obtained from the previous analysis at midspan, in line with the expected results, showed an increase not only in the LE but also in the rear part of the suction side (88% of the curvilinear abscissa) due to the destabilizing effect of the rotor and the flow deceleration which resulted in the transition of the flow from laminar to turbulent with an increase in heat transfer. The test-to-test repeatability was assessed.

Stator blades' pressure distribution was calculated and compared to CFD results showing a good agreement. The aerodynamic conditions study made it possible to interpret the heat transfer coefficient's trend verifying their influence of the latter.

The measurements carried out at 90% of the span instead showed a much more advanced peak towards the LE (35% of the curvilinear abscissa) probably due to the effect of the secondary flows near the casing that induced a premature transition.

The Nusselt number distribution, as a function of the Re number and turbulence was compared with the Lowery and Vachon's correlations used to predict the Nusselt number at the stagnation point showing a good agreement.

The unsteady analysis was carried out using the pWelch function in Matlab highlighting the influence of the rotor especially in the rear part of the suction side where the frequency content is higher and the blade passing frequency (4.7 kHz) and the associated harmonics are clearly distinguishable also before the start of the test.

In accordance with the unsteady analysis, the RMS trend also showed more pronounced fluctuations in the rear part of the suction side. The analysis of the period before the start of the test allowed to identify spurious frequency peaks not attributable to a real and physical behaviour of the fluid, also confirming that the test-to-test discrepancies in the RMS trend were due to the presence of noise.

The transition from laminar to turbulent was analysed through the intermittency factor and the skewness. Since the suction side is responsible for a large part of the overall losses, a greater number of sensors should be used in future investigations and experimental campaigns to be much more investigated in order to be able to appropriately know the trend of the intermittency factor and of the skewness that in the present evaluation, due to the lack of sufficient measurement points in the area of the discussion, did not provide results consistent with expectations.

Bibliography

[1] Sergio Lavagnoli. Turbine efficiency measurements at high pressure ratio. Project Report 2006-21, von Karman Institute for Fluid Dynamics, 2006.

[2] B. Cernat, M. Paty, C. De Maesschalck, S. Lavagnoli, Experimental and numerical investigation of optimized blade tip shapes - Part I: turbine rainbow rotor testing and cfd methods, in: ASME Turbo Expo 2018: Turbomachinery Technical Conference and Exposition, American Society of Mechanical Engineers, 2018, pp. V05BT13A012.

[3] V. Andreoli, S. Lavagnoli, G. Paniagua, V. F. Villace, Robust model of a transient wind tunnel for off-design aerothermal testing of turbomachinery. Measurement 82 (2016) 323-333. Doi : 10.1016/j.measurement.2015.12.032

[4] Claus H. Sieverding, Tony Arts, R. D´enos, and J.F. Brouckaert. Measurement techniques for unsteady flows in turbomachines. Experiments in Fluids, 28:285– 321, 2000.

[5] D.L. Schultz and T.V. Jones. Heat-Transfer Measurements in Short-Duration Hypersonic Facilities. University of Oxford, Gt.Britain: Department of Engineering Science, 1973.

[6] S.J. Thorpe and R.W. Ainsworth. The effects of blade passing on the heat transfer coefficient of the over-tip casing in transonic turbine stage. Journal of Turbomachinery, 130:041009, 2008.

[7] R. J. Moffat. “What’s New in Convective Heat Transfer?” In: International Journal of Heat and Fluid Flow (1998).

[8] Sergio Lavagnoli, Cis De Maesschalck, and Guillermo Paniagua. Uncertainty analysis of adiabatic wall temperature measurements in turbine experiments. Applied Thermal Engineering, 82:170–181, 03 2015.

[9] V. Pinilla, J.P. Solano, and G. Paniagua. Method and measurement of adiabatic wall temperature downstream of a high-pressure turbine using thin-film sensors. In ASME Turboexpo 2011, Vancouver, Canada, June 2011.

[10] M. L. G. Oldfield. Impulse Response Processing of Transient Heat Transfer Gauge Signals. Journal of Turbomachinery, APRIL 2008, Vol. 130 / 021023

[11] Ainsworth, R. W., Allen, J. L., Davies, M. R. D., Doorly, J. E., Forth, C. J. P., Hilditch, M. A., Oldfield, M. L. G., and Sheard, A. G., 1989, "Developments in Instrumentation and Processing for Transient Heat Transfer Measurements in a Full Stage Model Turbine," ASME J. Turbomach., 111, pp. 20–27.

[12] J. E. Doorly and M. Oldfield, "The theory of advanced multi-layer thin film heat transfer gauges," International Journal of Heat and Mass Transfer, vol. 30, no. 6, pp. 1159-1168, 1987.

[13] Denbigh, P., 1998, System Analysis and Signal Processing, Addison-Wesley, Reading, MA

[14] R. H. Dieck, Measurement uncertainties- methods and applications, ISA, 2007.

[15] Ronald Bunker. Axial turbine blade tips: Function, design, and durability. Journal of Propulsion and Power, 22:271–285, 03 2006.

[16] Ali A. Ameri. Heat transfer and flow on the blade tip of a gas turbine equipped with a mean-camberline strip. In ASME Turboexpo 2001, Louisiana, USA, June 2001.

[17] G. W. Lowery and R. I. Vachon, "The Effect of Turbulence on Heat Transfer from Heated Cylinders," International Journal of Heat and Mass Transfer, vol. 18, pp. 1229-1242, 1975.

[18] T. Coton, T. Arts, M. Lefebvre, and N. Liamis, "Unsteady and calming effects investigation on a very high-lift lp turbine blade–part i: Experimental analysis," Journal of Turbomachinery, vol. 125, no. 2, pp. 281–290, Apr. 2003.

[19] T. Ferreira "Influence of gas-to-wall temperature ratio on by-pass transition", 2016

[20] G. Luppino, "Design and Characterization of a Fast Response Temperature Probe for Gas Turbine Test Rigs"

[21] D. Favier, The role of wind tunnel experiments in cfd validation, Encyclopedia of Aerospace Engineering 1.

[22] J. Ustenko, “Direct and Inverse Heat Conduction Calculation applied to transient heat flux measurements,” VKI Project Report, 2011.

[23] BUTTSWORTH, D.R., JONES, T.V., A Fast-Response High Spatial Resolution Total Temperature Probe Using a Pulsed Heating Technique, Journal of Turbomachinery 120(3), 601-607 (7 pages), 1998

[24] Bogdan C. Cernat, Marek Paty, Cis De Maesschalcs, and Sergio Lavagnoli. Experimental and numerical investigation of optimized blade tip shapes — part i: Turbine rainbow rotor testing and numerical methods. Journal of Turbomachinery, 141:011006, 13 pages, 2019.

[25] Oldfield, M. L. G., Jones, T. V., and Schultz, D. L., 1978, “On-Line Computer for Transient Turbine Cascade Instrumentation,” IEEE Trans. Aerosp. Electron. Syst., 145——, pp. 738–749.

[26] P. M. Ligrani, C. Camci, and M. S. Grady. Thin Film Heat Transfer Gage Construction and Measurement Details. The Von Karman Institute for Fluid Dynamics, 1982.

[27] C. Sieverding, T. Arts, The vki compression tube annular cascade facility ct3, in:ASME 1992 International Gas Turbine and Aeroengine Confress and Exposition, American Society of Mechanical Engineers, 1992, pp. V005T16A001-V005T16A001.

Appendix A

Calibration coefficients

Acquisition	Name TC	Type TC	Amplifier	Channel	m ref [°C/V]	q ref [°C]	R^2 ref	mTC [°C/V]	qTC [°C]	R^2 TC
25/09 Test Chamber	HDCdown1	K	2	8	25184.78	20.97	0.99977	25079.45	21.17	0.99977
	HDCdown2	K	2	9	25103.50	21.30	0.99982	25002.99	21.78	0.99977
	HDCdown3	K	2	10	24595.89	23.61	0.99985	25022.43	21.77	0.99977
30/09 Test Chamber	HDC upstream 1	K	2	5	25356.63	23.89	0.99978	25326.63	23.28	0.99973
	HDC upstream 2	K	2	6	25417.23	23.22	0.99976	25344.70	23.16	0.99971
	HDC upstream 3	K	2	7	25470.38	22.75	0.99973	25337.27	22.99	0.99970
	EC-1	K	2	11	25519.55	22.72	0.99976	25337.40	23.27	0.99970
	EC-2	K	2	12	25651.43	22.18	0.99972	25351.76	23.30	0.99970
05/10 Oil Bath	Dao114A	K	2	1	24372.63	24.01	0.99992	24402.22	24.05	0.99989
	Dao114B	K	2	2	24310.63	24.29	0.99992	24380.68	24.32	0.99989
	Dao103A	K	2	3	24271.35	24.45	0.99993	24350.49	24.56	0.99989
	Dao103B	K	2	13	24516.96	24.41	0.99990	24404.51	24.48	0.99988
16/10 Oil Bath	Tat33-1	K	1	1	24331.56	25.33	0.99998	24367.83	25.39	0.99998
	Tat33-2	K	1	2	24272.14	25.58	0.99998	24346.69	25.57	0.99998
	Tat33-3	K	1	3	24213.63	25.69	0.99998	24319.75	25.78	0.99998
	Tat33-4	K	1	4	24259.49	25.93	0.99998	24271.59	25.90	0.99998
	Tat35-1	K	1	5	24265.84	25.83	0.99998	24285.19	25.88	0.99998
	Tat35-2	K	1	6	24168.13	25.68	0.99998	24266.55	25.75	0.99998
	Tat35-3	K	1	7	24137.22	25.53	0.99997	24244.05	25.59	0.99998
	Tat35-4	K	1	8	24290.21	25.31	0.99997	24233.58	25.35	0.99998
	Dao117-1	K	1	9	24109.07	25.24	1.00000	24347.95	25.33	0.99998
	Dao117-2	K	1	10	24075.52	25.33	0.99999	24334.87	25.49	0.99997
	Dao117-3	K	1	11	24057.19	25.53	0.99998	24334.08	25.52	0.99997
	Dao117-4	K	1	12	24277.19	25.75	0.99988	24198.16	25.68	0.99972
	Dao106-1	K	1	13	23970.01	25.53	0.99999	24278.16	25.72	0.99999
	Dao106-2	K	1	14	24448.90	25.36	0.99994	24211.96	25.65	0.99996
	Dao106-3	K	1	15	24261.25	25.22	0.99995	24261.78	25.47	0.99995
	Dao106-4	K	1	16	24651.92	25.01	0.99988	24199.73	25.26	0.99991
	Dao111A	K	2	4	24430.39	24.59	0.99994	24179.29	24.86	0.99966
	Next 668-1	K	2	14	23973.70	24.35	0.99997	24288.16	24.51	0.99998
	Next 668-2	K	2	15	24165.13	24.36	0.99998	24235.16	24.41	0.99997
	T tube	K	2	16	23985.44	24.15	0.99991	24137.62	24.12	0.99991

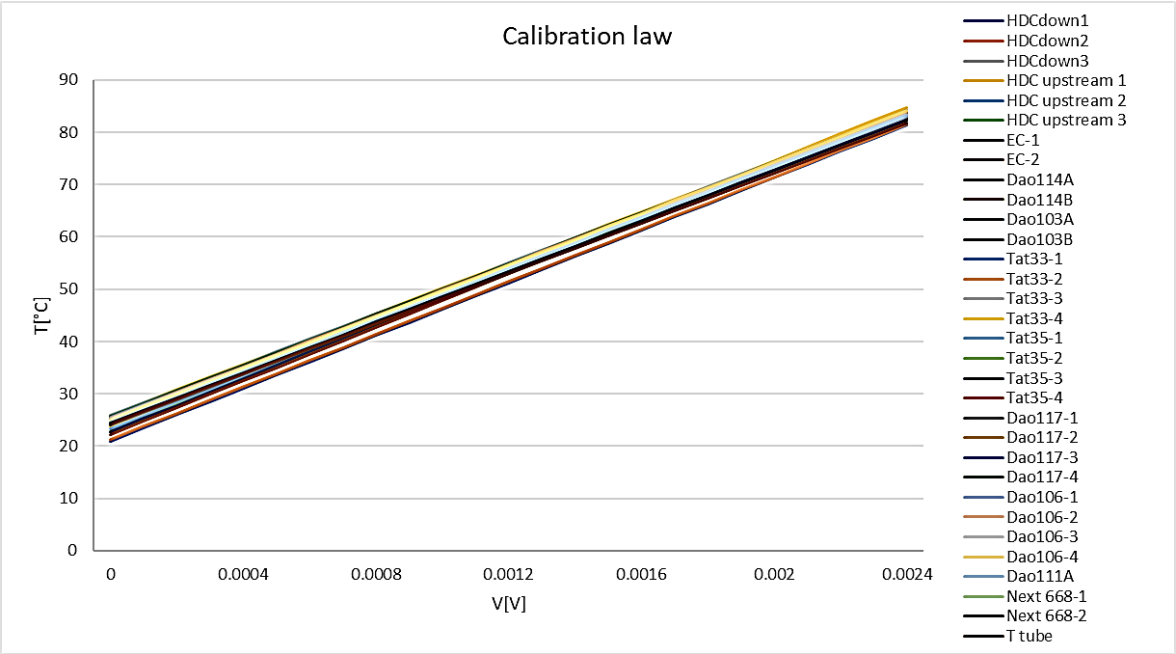

Table A1: Thermocouples' calibration set-up and coefficients

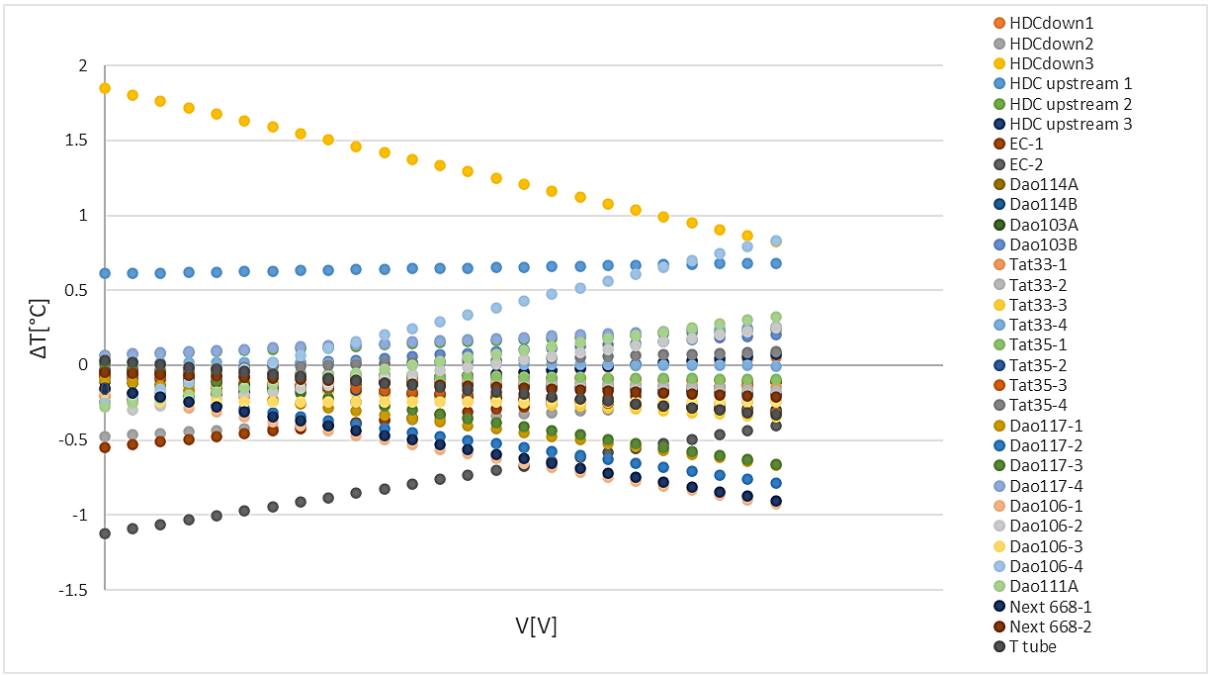

6Figure A1: Comparison in terms of temperature of the two calibrations, the reference one and the digitizer one

N	Slope [K/Ω]	Intercept [K]	R^2
1	5.746174	-350.976	0.999912
2	5.371812	-350.169	0.999932
3	5.724514	-350.856	0.999918
4	5.473625	-345.486	0.999922
5	5.671986	-350.582	0.999928
6	4.613125	-327.646	0.999906
7	5.551506	-348.628	0.999933
8	5.438908	-349.357	0.999935
10	5.389589	-348.482	0.999952
11	5.528571	-347.766	0.999928
12	5.246556	-347.856	0.99994
13	5.446508	-347.253	0.99993
14	5.363061	-347.9	0.999924
15	5.431068	-343.208	0.99991
16	5.038872	-347.385	0.999915
17	5.571978	-346.942	0.999857
18	5.239146	-346.913	0.999911
20	5.486796	-347.709	0.999919
22	5.558159	-348.275	0.999901
23	6.01422	-345.813	0.999898
24	5.592523	-349.112	0.999913
25	5.719914	-350.677	0.999912
26	5.60858	-348.151	0.99992
27	5.75871	-347.99	0.999907
28	5.569897	-348.072	0.999916
29	5.77039	-347.218	0.999895
30	5.735104	-347.472	0.999902
31	5.75127	-347.043	0.999909
32	5.490141	-347.596	0.999918
33	5.701544	-346.778	0.999903
34	5.435333	-343.269	0.999927
35	5.674302	-348.042	0.999903
36	5.680206	-347.175	0.999917
37	5.808859	-347.249	0.999915
38	5.870832	-347.022	0.999918

Table A2: Calibration coefficients thin film casing insert

TF 50%	Slope [K/Ω]	Intercept [K]	TF 90%	Slope [K/Ω]	Intercept [K]
1	21.79847	-919.881	1	21.66694	-935.287
2	21.88867	-920.855	2	22.52433	-923.557
3	22.02226	-916.418	3	18.41251	-941.465
4	23.8235	-994.938	4	24.28183	-1015.63
5	21.00225	-931.326	5	23.25526	-942.57
6	21.61801	-916.819	6	22.45029	-949.415
7	22.66857	-932.658	7	22.3275	-941.302
8	22.31833	-917.278	8	21.93798	-933.17
9	22.11829	-898.694	9	22.35182	-941.058
10	22.22186	-905.743	10	22.48181	-938.077
11	21.69469	-897.099	11	22.10854	-925.671
12	21.81973	-896.901	12	22.27373	-923.134
13	23.49867	-994.496	13	22.41782	-920.501
14	23.59279	-965.7	14	25.00261	-991.492
15	20.59154	-922.301	15	22.48678	-926.713
16	21.46655	-913.807	16	22.01993	-927.032
17	22.09874	-914.287	17	22.13852	-932.701
18	24.86069	-992.339	18	25.7544	-1019.35
19	17.14561	-873.99	19	21.80258	-930.472
20	21.25786	-892.35	20	22.04532	-915.734
21	21.50831	-916.483	21	22.52812	-921.003
22	21.1379	-880.433	22	22.29469	-912.961
23	21.67608	-894.804	23	22.60016	-921.084
24	20.69761	-927.401	24	22.56285	-909.623
25	21.42432	-899.619	25	22.41295	-905.315
26	21.28483	-914.03	26	21.59831	-906.73

Table A3: Calibration coefficients thin film on instrumented vane

Appendix B

Thin films position and experimental campaign flow conditions

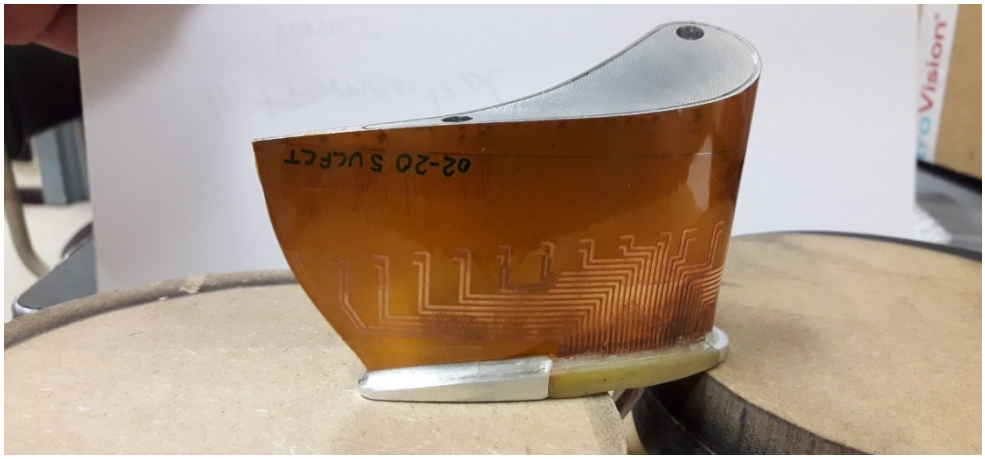

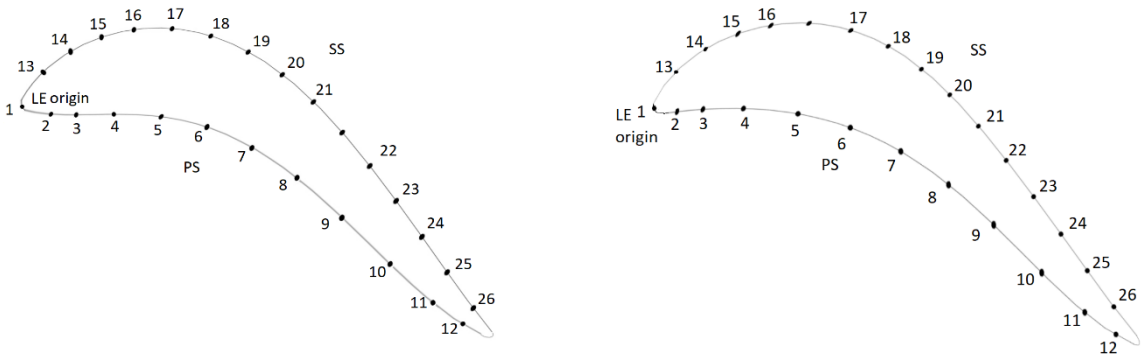

Figure B1: Geometry of the tested profile and thin film location at midspan (on the left) and at 90% of the vane span (on the right)

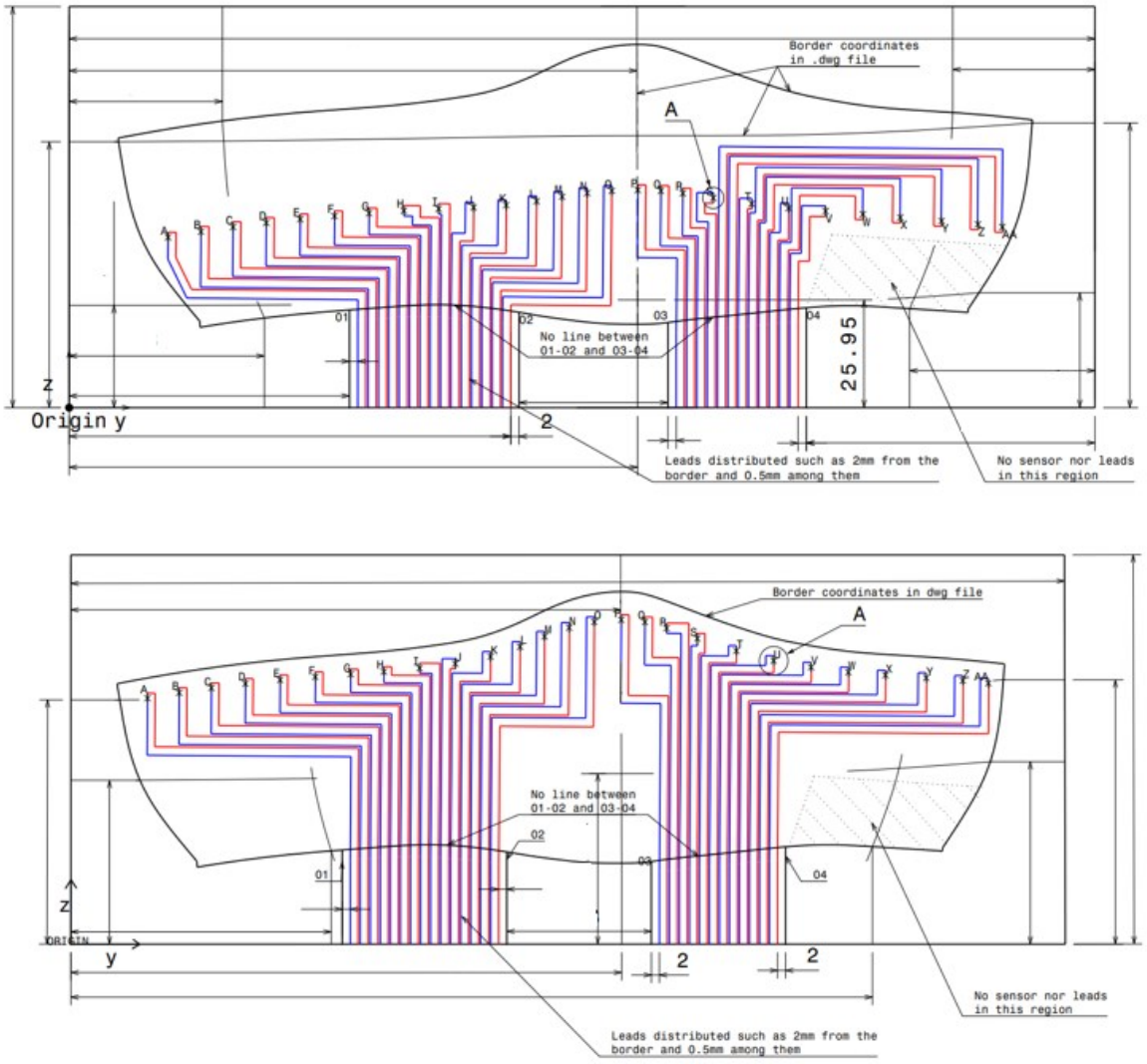

Figure B2: Stator blade thin film: 50% and 90%

50%		90%	
Y [%]	S/Smax [%]	Y [%]	S/Smax [%]
-96.00%	-94.51%	-96.21%	93.49%
-89.56%	-88.18%	-89.52%	87.08%
-79.98%	-78.75%	-79.93%	77.92%
-69.12%	-68.09%	-69.25%	67.71%
-59.26%	-58.40%	-59.52%	58.42%
-49.45%	-48.75%	-49.75%	49.02%
-39.70%	-39.18%	-30.17%	29.89%
-19.88%	-19.60%	-19.94%	19.67%
-11.85%	-11.64%	-11.89%	11.57%
-6.08%	-5.96%	-6.19%	5.93%
0.00%	0.00%	0.00%	0.00%
5.28%	5.17%	5.39%	5.22%
10.29%	10.10%	10.40%	10.19%
15.39%	15.14%	15.33%	15.25%
20.55%	20.28%	20.21%	20.37%
26.73%	26.37%	33.18%	33.35%
33.36%	32.88%	40.31%	40.29%
40.43%	39.82%	47.45%	47.22%
47.50%	46.75%	54.08%	53.66%
54.57%	53.69%	61.16%	60.51%
68.54%	67.42%	68.19%	67.33%
75.43%	74.20%	75.13%	74.07%
82.18%	80.86%	81.92%	80.69%
88.68%	87.30%	88.36%	86.98%
95.36%	93.95%	94.81%	93.20%

Figure B3: thin film positions along the chord and along the curvilinear abscissa: 50% and 90%

	TEST29	*TEST34*	*TEST35*	*TEST38*	*TEST39*	*TEST40*
Test Type	Blowdown	Blowdown	Blowdown	Blowdown	Blowdown	Blowdown
DATE	20/01/2021	22/01/2021	22/01/2021	25/01/2021	25/01/2021	25/01/2021
P01 target	1.040	1.040	1.040	1.040	1.040	1.040
T01 target	440	440	440	440	440	440
Prat	1.105	1.105	1.105	1.105	1.105	1.105
Trat	1.1	1.1	1.1	1.1	1.1	1.1
Pi - tube	-607.7	-602.4	-603.5	-615	-615.9	-616.6
Pf - tube	0.1747	0.1817	0.1803	0.1692	0.1658	0.1646
Ttube - fin						
Pres300	165	160	156	172	170	169
Tres	283	283	283	283	283	283
Margherite	-800	-800	-800	-800	-799	-799
Carrote-Encoder	480	602	663	359	418	418
Carrote-33 open	1	1	1	1	1	1
Tamb	16.2	17	17	16	16	15.8
Patm mmHg	739.230	733.970	735.040	744.927	744.927	746.550
Patm mbar	985.600	978.545	979.970	993.170	993.170	995.310
Pvac						
RPM - pretest	5800	5800	5800	5820	5820	5820
P01 stability trend	OK	Falling	Falling	-	-	OK
P01 stability DP	1.2	9.0	2.5	-	-	1.8
Pratio HUB	2.191	2.19	2.167	-	-	2.195
Pratio TIP	2.205	2.207	2.186	-	-	2.215
Orifice	13.50	13.50	13.50	12.33	12.33	12.33
Ptank	5.50	5.45	5.50	5.00	5.00	5.00
mpurge	37.5%	31.8%	38.4%	Nominal	Nominal	Nominal
mpurge stability	11%	12%	9%	-	-	11%
Comments	Mpurge high	Delayed injection ~50ms, HT 50% good for extra purge	Injection ~150ms, HT 50% good for extra purge	No SCANIVALVE, COND. AS 40 --> HT GOOD 1/7	No SCANIVALVE, COND. AS 40 --> HT GOOD 2/7	CONDITIONS RETRIEVED, HT GOOD 3/7
Scanivalve	Phase 2	Phase 2	Phase 2	Phase 2	Phase 2	Phase 2

	TEST47	*TEST48*	*TEST49*	*TEST50*	*TEST51*	*TEST52*
Test Type	Blowdown	Blowdown	Blowdown	Blowdown	Blowdown	Blowdown
DATE	29/01/2021	29/01/2021	02/01/2021	02/01/2021	02/01/2021	02/02/2021
P01 target	1.040	1.040	1.040	1.040	1.040	1.040
T01 target	440	440	440	440	440	440
Prat	1.105	1.105	1.105	1.105	1.105	1.105
Trat	1.1	1.1	1.1	1.1	1.1	1.1
Pi - tube	-603.9	-605	-602.8	-604.3	-605.6	-607.8
Pf - tube	0.1771	0.1758	0.1833	0.1813	0.1775	0.1767
Ttube - fin						
Pres300	165	162	155	159	169	165
Tres	283	283	283	283	283	283
Margherite	-799	-799	-799	-799	-799	-799
Carrote-Encoder	540	542	719	602	422	483
Carrote-33 open	1	1	1	1	1	1
Tamb	18.4	18	16	16	16	15.8
Patm mmHg	737.400	738.410	733.590	735.040	737.132	737.750
Patm mbar	983.118	984.470	978.040	979.970	982.760	983.590
Pvac mbar			47.0	48.4		
RPM - pretest	5820	5820	5820	5820	5820	5820
P01 stability trend	OK	OK	OK	OK	OK	OK
P01 stability DP			2.4	4	1.5	1.5
Pratio HUB	2.183	2.193	2.194	2.195	2.19	2.193
Pratio TIP	2.203	2.213	2.213	2.216	2.211	2.213
Orifice	12.33	12.33	12.33	12.33	12.33	12.33
Ptank	5.01	5.01	5.03	5.02	5.00	5.00
mpurge	1.57%	1.07%	2.40%	1.19%	-0.13%	0.47%
mpurge stability	11.60%	13%	14%	11%	12%	14%
Comments	HT 90% mounted 1, GTP heater ok	HT 90% mounted 2, GTP heater ok	HT 90% mounted 3	HT 90% mounted 4	HT 90% mounted 5	HT 90% mounted 6
Scanivalve	Phase 1	Phase 1	Phase 1	Phase 1	Phase 1	Phase 1

Table B3: Summary of the test conditions at 50% and 90% of the vane span

Appendix C

Thin films setup and connections

% Name	TFname	FiltN	FiltCh	I cur [mA]	INA	EXT	Mode	FiltType	
LP_HT1_50_01	1	2	B1	15	5	1	R0	LP	dir
LP_HT1_50_02	2	2	B2	15	5	1	R0	LP	dir
LP_HT1_50_03	3	2	B3	15	5	1	R0	LP	dir
LP_HT1_50_04	4	2	B5	15	5	1	R0	LP	dir
LP_HT1_50_06	6	2	B6	15	5	1	R0	LP	dir
LP_HT1_50_07	7	2	B7	15	5	1	R0	LP	dir
LP_HT1_50_08	8	2	B8	15	5	1	R0	LP	dir
LP_HT1_50_09	9	2	B9	15	5	1	R0	LP	dir
LP_HT1_50_10	10	4	A1	15	5	1	R0	LP	dir
LP_HT1_50_11	11	4	A2	15	5	1	R0	LP	dir
LP_HT1_50_12	12	4	A3	15	5	1	R0	LP	dir
LP_HT1_50_13	13	4	A4	15	5	1	R0	LP	dir
LP_HT1_50_14	14	4	A5	15	5	1	R0	LP	dir
LP_HT1_50_15	15	4	A6	15	5	1	R0	LP	dir
LP_HT1_50_16	16	4	A7	15	5	1	R0	LP	dir
LP_HT1_50_17	17	4	A8	15	5	1	R0	LP	dir
LP_HT1_50_18	18	4	A9	15	5	1	R0	LP	dir
LP_HT1_50_19	19	4	B1	15	5	1	R0	LP	dir
LP_HT1_50_20	20	4	B2	15	5	1	R0	LP	dir
LP_HT1_50_21	21	4	B3	15	5	1	R0	LP	dir
LP_HT1_50_22	22	4	B4	15	5	1	R0	LP	dir
LP_HT1_50_23	23	4	B5	15	5	1	R0	LP	dir
LP_HT1_50_24	24	4	B6	15	5	1	R0	LP	dir
LP_HT1_50_25	25	4	B7	15	5	1	R0	LP	dir
LP_HT1_50_26	26	4	B8	15	5	1	R0	LP	dir
HP_HT1_50_01	1	2	B1	15	5	1	R0	HP	F50k
HP_HT1_50_02	2	2	B2	15	5	1	R0	HP	F50k
HP_HT1_50_03	3	2	B3	15	5	1	R0	HP	F50k
HP_HT1_50_04	4	2	B5	15	5	1	R0	HP	F50k
HP_HT1_50_06	6	2	B6	15	5	1	R0	HP	F50k
HP_HT1_50_07	7	2	B7	15	5	1	R0	HP	F50k
HP_HT1_50_08	8	2	B8	15	5	1	R0	HP	F50k
HP_HT1_50_09	9	2	B9	15	5	1	R0	HP	F50k
HP_HT1_50_10	10	4	A1	15	5	1	R0	HP	F50k
HP_HT1_50_11	11	4	A2	15	5	1	R0	HP	F50k
HP_HT1_50_12	12	4	A3	15	5	1	R0	HP	F50k

HP_HT1_50_13	13	4	A4	15	5	1	R0	HP	F50k
HP_HT1_50_14	14	4	A5	15	5	1	R0	HP	F50k
HP_HT1_50_15	15	4	A6	15	5	1	R0	HP	F50k
HP_HT1_50_16	16	4	A7	15	5	1	R0	HP	F50k
HP_HT1_50_17	17	4	A8	15	5	1	R0	HP	F50k
HP_HT1_50_18	18	4	A9	15	5	1	R0	HP	F50k
HP_HT1_50_19	19	4	B1	15	5	1	R0	HP	F50k
HP_HT1_50_20	20	4	B2	15	5	1	R0	HP	F50k
HP_HT1_50_21	21	4	B3	15	5	1	R0	HP	F50k
HP_HT1_50_22	22	4	B4	15	5	1	R0	HP	F50k
HP_HT1_50_23	23	4	B5	15	5	1	R0	HP	F50k
HP_HT1_50_24	24	4	B6	15	5	1	R0	HP	F50k
HP_HT1_50_25	25	4	B7	15	5	1	R0	HP	F50k
HP_HT1_50_26	26	4	B8	15	5	1	R0	HP	F50k

% Name	*TFname*	*FiltN*	*FiltCh*	*I cur [mA]*	*INA*	*EXT*	*Mode*	*FiltType*	
LP_HT1_90_01	1	2	B1	15	5	1	R0	LP	dir
LP_HT1_90_02	2	2	B2	15	5	1	R0	LP	dir
LP_HT1_90_03	3	2	B3	15	5	1	R0	LP	dir
LP_HT1_90_04	4	2	B5	15	5	1	R0	LP	dir
LP_HT1_90_05	5	4	B9	15	5	1	R0	LP	dir
LP_HT1_90_06	6	2	B6	15	5	1	R0	LP	dir
LP_HT1_90_07	7	2	B7	15	5	1	R0	LP	dir
LP_HT1_90_08	8	2	B8	15	5	1	R0	LP	dir
LP_HT1_90_09	9	2	B9	15	5	1	R0	LP	dir
LP_HT1_90_10	10	4	A1	15	5	1	R0	LP	dir
LP_HT1_90_11	11	4	A2	15	5	1	R0	LP	dir
LP_HT1_90_12	12	4	A3	15	5	1	R0	LP	dir
LP_HT1_90_13	13	4	A4	15	5	1	R0	LP	dir
LP_HT1_90_14	14	4	A5	15	5	1	R0	LP	dir
LP_HT1_90_15	15	4	A6	15	5	1	R0	LP	dir
LP_HT1_90_16	16	4	A7	15	5	1	R0	LP	dir
LP_HT1_90_17	17	4	A8	15	5	1	R0	LP	dir
LP_HT1_90_18	18	4	A9	15	5	1	R0	LP	dir
LP_HT1_90_19	19	4	B1	15	5	1	R0	LP	dir
LP_HT1_90_20	20	4	B2	15	5	1	R0	LP	dir
LP_HT1_90_21	21	4	B3	15	5	1	R0	LP	dir
LP_HT1_90_22	22	4	B4	15	5	1	R0	LP	dir
LP_HT1_90_23	23	4	B5	15	5	1	R0	LP	dir
LP_HT1_90_24	24	4	B6	15	5	1	R0	LP	dir

LP_HT1_90_25	25	4	B7	15	5	1	R0	LP	dir
LP_HT1_90_26	26	4	B8	15	5	1	R0	LP	dir
HP_HT1_90_01	1	2	B1	15	5	1	R0	HP	F50k
HP_HT1_90_02	2	2	B2	15	5	1	R0	HP	F50k
HP_HT1_90_03	3	2	B3	15	5	1	R0	HP	F50k
HP_HT1_90_04	4	2	B5	15	5	1	R0	HP	F50k
HP_HT1_90_05	5	4	B9	15	5	1	R0	HP	F50k
HP_HT1_90_06	6	2	B6	15	5	1	R0	HP	F50k
HP_HT1_90_07	7	2	B7	15	5	1	R0	HP	F50k
HP_HT1_90_08	8	2	B8	15	5	1	R0	HP	F50k
HP_HT1_90_09	9	2	B9	15	5	1	R0	HP	F50k
HP_HT1_90_10	10	4	A1	15	5	1	R0	HP	F50k
HP_HT1_90_11	11	4	A2	15	5	1	R0	HP	F50k
HP_HT1_90_12	12	4	A3	15	5	1	R0	HP	F50k
HP_HT1_90_13	13	4	A4	15	5	1	R0	HP	F50k
HP_HT1_90_14	14	4	A5	15	5	1	R0	HP	F50k
HP_HT1_90_15	15	4	A6	15	5	1	R0	HP	F50k
HP_HT1_90_16	16	4	A7	15	5	1	R0	HP	F50k
HP_HT1_90_17	17	4	A8	15	5	1	R0	HP	F50k
HP_HT1_90_18	18	4	A9	15	5	1	R0	HP	F50k
HP_HT1_90_19	19	4	B1	15	5	1	R0	HP	F50k
HP_HT1_90_20	20	4	B2	15	5	1	R0	HP	F50k
HP_HT1_90_21	21	4	B3	15	5	1	R0	HP	F50k
HP_HT1_90_22	22	4	B4	15	5	1	R0	HP	F50k
HP_HT1_90_23	23	4	B5	15	5	1	R0	HP	F50k
HP_HT1_90_24	24	4	B6	15	5	1	R0	HP	F50k
HP_HT1_90_25	25	4	B7	15	5	1	R0	HP	F50k
HP_HT1_90_26	26	4	B8	15	5	1	R0	HP	F50k

Table C1: thin-film setup and connections at 50% and 90% of the vane's span

Appendix D

Total power spectral density of the signal acquired.

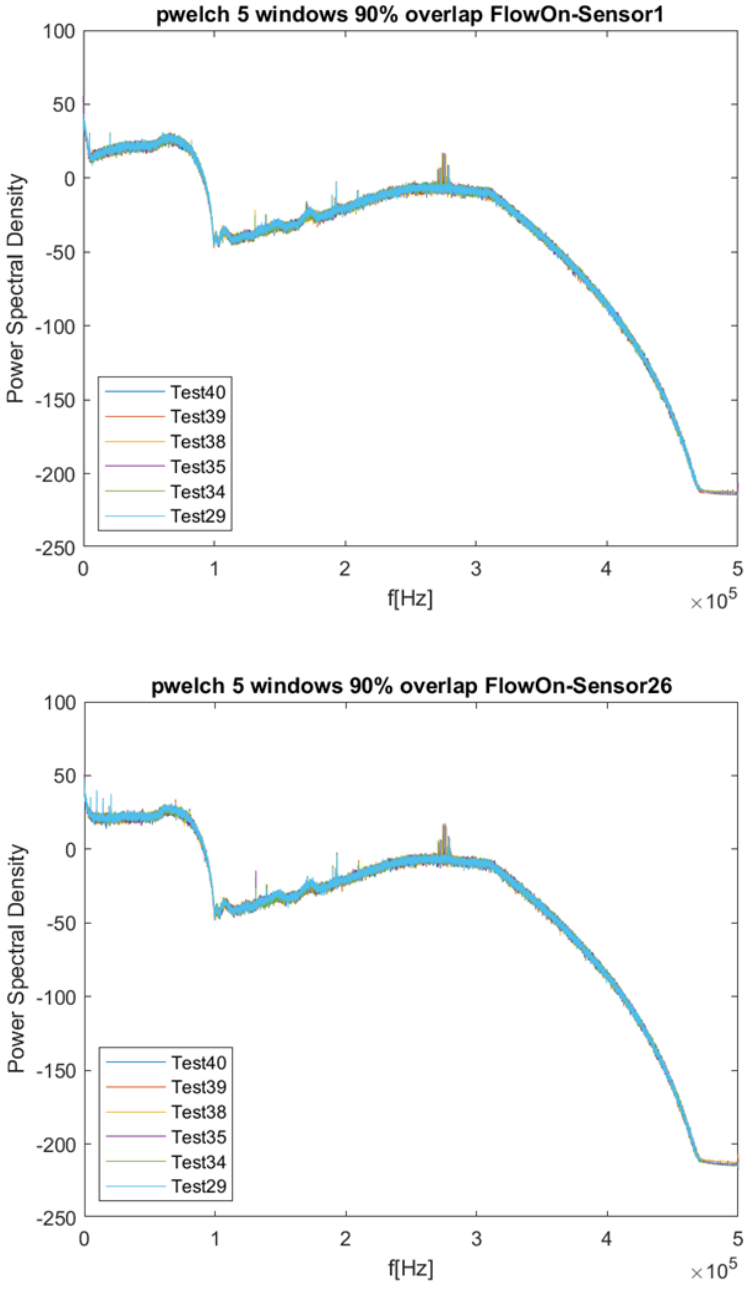

Figure D1: Power spectral density